

EXPERIMENTAL QUIET ENGINE PROGRAM AERODYNAMIC PERFORMANCE OF FAN B

by

R.G. Giffin
D.E. Parker
L.W. Dunbar

GENERAL ELECTRIC COMPANY

prepared for

NATIONAL AERONAUTICS AND SPACE ADMINISTRATION

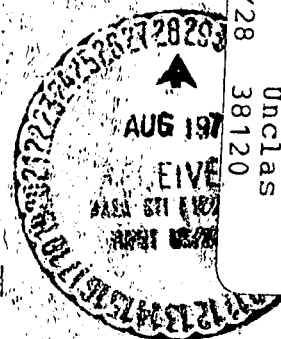
NASA-Lewis Research Center
Contract NAS3-12430
E.W. Conrad, Project Manager

Reproduced by
NATIONAL TECHNICAL
INFORMATION SERVICE
U S Department of Commerce
Springfield VA 22151

(NASA-CR-72993) EXPERIMENTAL QUIET ENGINE
PROGRAM AERODYNAMIC PERFORMANCE OF FAN B
R.G. Giffin, et al (General Electric Co.)
Aug. 1972 117 p
CSSL 21E

G3/28 38120
Unclas

N72-29808



12380
1271

1. Report No. NASA CR-72993		2. Government Accession No.		3. Recipient's Catalog No.	
4. Title and Subtitle EXPERIMENTAL QUIET ENGINE PROGRAM AERODYNAMIC PERFORMANCE OF FAN B				5. Report Date August 1972	
				6. Performing Organization Code	
7. Author(s) Giffin, R.G., Parker, D.E., and Dunbar, L.W.				8. Performing Organization Report No.	
9. Performing Organization Name and Address General Electric Company Aircraft Gas Turbine Division Cincinnati, Ohio 45215				10. Work Unit No.	
				11. Contract or Grant No. NAS 3-12430	
12. Sponsoring Agency Name and Address National Aeronautics and Space Administration Washington, D.C. 20546				13. Type of Report and Period Covered Contractor Report	
				14. Sponsoring Agency Code	
15. Supplementary Notes Project Manager, E. W. Conrad, V/STOL & Noise Division NASA Lewis Research Center, Cleveland, Ohio					
16. Abstract This report presents the aerodynamic component test results of Fan B, one of two high-bypass-ratio, 1160 feet per second (353.6 m/sec) single-stage fans, which was designed and tested as part of the NASA Experimental Quiet Engine Program. The fan was designed to deliver a bypass pressure ratio of 1.50 with an adiabatic efficiency of 87.0% at a total fan flow of 950 lb/sec (430.9 kg/sec). It was tested with and without inlet distortion. A bypass total pressure ratio of 1.52 and an adiabatic efficiency of 86.9% at a total fan flow of 966 lb/sec (438.2 kg/sec) were actually achieved. An operating margin of 19.5% was demonstrated at design speed.					
17. Key Words (Suggested by Author(s)) Fan, Compressor, Inlet Flow Distortion, Aerodynamic Performance				18. Distribution Statement Unclassified - Unlimited	
19. Security Classif. (of this report) Unclassified		20. Security Classif. (of this page) Unclassified		21. No. of Pages 116	
				22. Price* \$9.00 \$8.00	

Details of illustrations in
this document may be better
studied on microfiche.

TABLE OF CONTENTS

	<u>Page</u>
1.0 SUMMARY	1
2.0 INTRODUCTION	3
3.0 DESCRIPTION OF TEST FAN	5
4.0 TEST SET-UP AND PROCEDURE	9
A. TEST FACILITY	9
B. OVERALL PERFORMANCE INSTRUMENTATION	9
C. BYPASS RATIO SCHEDULE	11
D. VEHICLE CONFIGURATION	11
5.0 RESULTS AND DISCUSSION	13
A. PRESENTATION OF OVERALL RESULTS	13
B. UNDISTORTED FLOW PERFORMANCE	13
1. Fan Bypass Region	13
2. Fan Core Performance	16
3. Bypass Ratio Excursion	23
4. Fan Bypass OGV Schedule	45
5. Fan Core OGV Schedule	45
6. Traverse Data	48
C. DISTORTED FLOW PERFORMANCE	48
6.0 SUMMARY OF RESULTS	65
7.0 REFERENCES	67
APPENDIX I INSTRUMENTATION	69
APPENDIX II COMPUTATION OF OVERALL FAN PERFORMANCE	73
APPENDIX III OVERALL PERFORMANCE DATA FOR BUILD 1	77
APPENDIX IV ROTOR TIP PRESSURE PATTERNS	87
APPENDIX V AEROMECHANICAL PERFORMANCE	101
LIST OF SYMBOLS	115

Preceding page blank

LIST OF ILLUSTRATIONS

<u>Figure</u>		<u>Page</u>
1	Fan B Component Test Vehicle Layout.	7
2	Full-Scale Compressor and Fan Test Facility.	10
3	Fan B Component Test, Bypass Ratio Schedule.	12
4	Fan B Performance Characteristics in the Bypass Region.	14
5	Fan B Performance Characteristics in the Core Region.	15
6	Radial Efficiency Profile at Discharge.	18
7	Radial Profiles.	19
8	Radial Profiles.	20
9	Radial Profiles.	21
10	Radial Profiles, Build 1.	22
11	Variation of Element Properties with Throttling, Design Stream Function = 0.06 (Bypass OD, Immersion 1).	24
12	Variation of Element Properties with Throttling, Design Stream Function = 0.302 (Bypass Immersion 3).	25
13	Variation of Element Properties with Throttling, Design Stream Function = 0.543 (Bypass Immersion 5).	26
14	Variation of Element Properties with Throttling Design Stream Function = 0.785 (Bypass ID, Immersion 7).	27
15	Variation of Element Properties with Throttling, Design Function = 0.861 (Core OD, Immersion 1).	28
16	Variation of Element Properties with Throttling, Design Stream Function = 0.892 (Core Immersion 2).	29
17	Variation of Element Properties with Throttling, Design Stream Function = 0.923 (Core Immersion 3).	30
18	Variation of Element Properties with Throttling, Design Stream Function = 0.954 (Core Immersion 4).	31
19	Variation of Element Properties with Throttling, Design Stream Function = 0.985 (Core ID, Immersion 5).	32
20	Bypass Ratio Excursion, Bypass Performance.	34
21	Bypass Ratio Excursion, Core Performance.	35
22	Variation of Element Properties with Bypass Ratio, Design Stream Function = 0.422.	36
23	Variation of Element Properties with Bypass Ratio, Design Stream Function = 0.543.	37

LIST OF ILLUSTRATIONS (Continued)

<u>Figure</u>		<u>Page</u>
24	Variation of Element Properties with Bypass Ratio, Design Stream Function = 0.664.	38
25	Variation of Element Properties with Bypass Ratio, Design Stream Function = 0.785.	39
26	Variation of Element Properties with Bypass Ratio, Design Stream Function = 0.861.	40
27	Variation of Element Properties with Bypass Ratio, Design Stream Function = 0.892.	41
28	Variation of Element Properties with Bypass Ratio, Design Stream Function = 0.923.	42
29	Variation of Element Properties with Bypass Ratio, Design Stream Function = 0.954.	43
30	Variation of Element Properties with Bypass Ratio, Design Stream Function = 0.985.	44
31	Effects of OGV Setting Angle on Bypass Performance.	46
32	Effect of OGV Closure on Fan Core Performance.	47
33	Traverse Radial Profiles, Radius Vs. Total Pressure Ratio (Bypass).	49
34	Traverse Radial Profiles, Radius Vs. Corrected Total Temperature Rise (Bypass).	50
35	Traverse Radial Profiles, Radius Vs. Adiabatic Efficiency (Bypass).	51
36	Traverse Radial Profiles, Radius Vs. Absolute Air Angle (Bypass).	52
37	Traverse Radial Profiles, Radius Vs. Relative Air Angle (Bypass).	53
38	Traverse Radial Profiles, Radius Vs. Total Pressure Ratio (Core).	54
39	Traverse Radial Profiles, Radius Vs. Corrected Total Temperature Rise (Core).	55
40	Traverse Radial Profiles, Radius Vs. Adiabatic Efficiency (Core).	56
41	Traverse Radial Profiles, Radius Vs. Absolute Air Angle (Core).	57
42	Inlet Flow Distortion Level.	58
43	Tip Radial Distortion Inlet Pressure Profile.	60
44	Hub Radial Distortion Inlet Pressure Profile.	61
45	One/Rev Distortion Pattern.	62

LIST OF ILLUSTRATIONS (Continued)

<u>Figure</u>		<u>Page</u>
46	Demonstrated Fan Performance Distortion Patterns in Inlet.	63
47	Demonstrated Core Portion Fan Performance Distortion Patterns in Inlet.	64
48	Fan B Test Vehicle Instrumentation Location.	71
49	Inlet Boundary Layer Description.	74
50	Typical Inlet Duct Pressure Profiles.	75
51	Fan B Performance Map, Fan Bypass Total Pressure Ratio Vs. Total Fan Flow.	78
52	Fan B Performance Map, Fan Core Total Pressure Ratio Vs. Core Fan Flow.	79
53	Tip Radial Distortion Inlet Pressure Profile.	80
54	Hub Radial Distortion Inlet Pressure Profile.	81
55	One/Rev Distortion Inlet Pressure Profile.	82
56	Fan B Performance Map, Tip Radial Distortion (Build 1).	83
57	Fan B Performance Map, Hub Radial Distortion (Build 1).	84
58	Fan B Performance Map, One/Rev Distortion (Build 1).	85
59	Typical Data Record of Kulite Trace.	89
60	Readings Taken for Rotor Tip Static Pressure Contours.	90
61	Rotor Static Pressure Distribution.	91
62	Rotor Static Pressure Distribution.	92
63	Rotor Static Pressure Distribution.	93
64	Rotor Static Pressure Distribution.	94
65	Rotor Static Pressure Distribution.	95
66	Rotor Static Pressure Distribution.	96
67	Rotor Static Pressure Distribution.	97
68	Rotor Static Pressure Distribution.	98
69	Rotor Static Pressure Distribution.	99
70	Titanium-Bladed Fan B Nominal Operating Line Vibrational Characteristic.	105
71	Titanium-Bladed Fan B Campbell Diagram.	106
72	Fan B Stator Vanes Nominal Operating Line Vibration Characteristic.	109

LIST OF ILLUSTRATIONS (Concluded).

<u>Figure</u>		<u>Page</u>
73	Fan B Bypass OGV, Campbell Diagram.	110
74	Fan B Aft Inner OGV, Campbell Diagram.	111
75	Fan B Forward Inner OGV, Campbell Diagram.	112

1.0 SUMMARY

This report presents the aerodynamic component test results of Fan B, one of two high-bypass-ratio, 1160 feet per second (353.6 m/sec) single-stage fans, which was designed and tested as part of the NASA Experimental Quiet Engine Program. The fan was tested with an undistorted inlet flow and with circumferential and radial distortions. The hub tip radius ratio was 0.465 at rotor inlet. A flow splitter, immediately downstream of the rotor, separates the fan bypass flow from the fan core flow. An axial distance equal to two rotor chords was employed between the rotor and bypass portion outlet guide vanes, (OGV). The vane-number-to-blade-number ratio was 2.3. No inlet guide vanes were employed.

The fan was designed to deliver a bypass total pressure ratio of 1.50 at a total fan flow of 950 lb/sec (430.9 kg/sec). The design bypass adiabatic efficiency was 87.0%. A bypass portion total pressure ratio of 1.52 and an adiabatic efficiency of 86.9% at a flow of 966 lb/sec (438.2 kg/sec) were actually achieved. The fan core region was designed to develop a total pressure ratio of 1.43 at a flow of 147.3 lb/sec (66.8 kg/sec). A fan core portion pressure ratio of 1.425 was actually achieved at its design flow. At this condition a fan core adiabatic efficiency of 77.0% was measured.

The operational limit line was determined up to 100% corrected speed. Rotating stall was the operational limit at all speeds except 85 and 90% where high rotor stress precluded further increases in back pressure. At 100% corrected speed, an operating margin of 19.5% was achieved relative to the design operating line at altitude-cruise conditions; at 90% corrected speed the operating margin was 10.9% relative to the design operating line at sea-level-static conditions.

The fan was tested with one-per-rev circumferential, tip radial, and hub radial distortion screens installed. At 90% corrected speed, the screens were found to produce approximately 15% distortion (maximum minus minimum pressure divided by maximum pressure). The fan demonstrated minimal operating margin loss to one-per-rev circumferential and hub radial distortions. The tip radial distortion resulted in a substantial operating margin degradation.

2.0 INTRODUCTION

In the last 20 years the rapid growth of the commercial aviation industry has demanded large increases in aircraft size and flight frequency. This, coupled with the increased public awareness of the noise pollution problem, has prompted the initiation of an Experimental Quiet Engine Program by the NASA-Lewis Research Center (Contract NAS3-12430). The major objectives of this program are: the demonstration of noise levels produced by turbofan engines which are designed for low noise output and confirmation that predicted noise reduction can be achieved; demonstration of the technology and design innovations which will reduce the production and radiation of noise in high-bypass turbofan engines; and acquisition of experimental acoustic and aerodynamic data for turbofan engines, which are designed for low noise output, to give a basis for correction of acoustic theory and experiment, and to give a better understanding of the noise production mechanisms in fans, compressors, turbines, and nozzles.

Observations of past trends indicate that as tip speed increases, at constant aerodynamic loading, fan broadband noise increases. Also, at constant tip speed, a reduction in aerodynamic loading is observed to decrease fan pure tone noise. Hence, for given mission requirements, the minimum fan noise configuration requires consideration of the weighted sum of the two types of noise. In order to confirm acoustic noise predictions and to acquire acoustic and aerodynamic data for typical high-bypass fans two low-speed fans, designated Fan A and Fan B, and one low-aerodynamic-loading fan, designated Fan C, were designed.

The aerodynamic performance of the three fans has been determined in the General Electric Large Fan Test Facility in Lynn, Massachusetts. Upon completion of the aerodynamic testing, each fan, in turn, is to be tested in the NASA-Lewis Acoustic Test Facility.

One of the low-speed fans, Fan A has been selected, and the low-aerodynamic-loading Fan C are to be mated with a TF39/CF6 engine core. The complete full-scale high-bypass fan engines will then be tested at the General Electric Remote Test Site at Peebles, Ohio, to determine their overall aeroacoustic performance as well as thrust and specific fuel consumption.

This report presents the aerodynamic component test results on Fan B with uniform inlet flow and with tip radial, hub radial, and circumferential distortion of the inlet flow. Details of the design of Fan B, and the other fans to be evaluated in this test series, are given in Reference 1.

Preceding page blank

3.0 DESCRIPTION OF TEST FAN

The aerodynamic design point for this low-speed fan was selected at the altitude cruise condition, a flight Mach number of 0.8 at an altitude of 36,000 feet (10.97 km). At this condition the corrected tip speed is 1160 ft/sec (353.6 m/sec) with an average fan bypass total pressure ratio of 1.50 and an average fan core total pressure ratio of 1.43. The design corrected fan flow of 950 lb/sec (430.9 kg/sec), with a hub tip radius ratio of 0.465 and a specific flow of 41.3 lb/sec/ft² (197.0 kg/sec/m²) of annulus area, results in a tip diameter of 73.354 inches (1.863 m). The design flow for the fan core, corrected to fan inlet, was 147.3 lb/sec (66.8 kg/sec) resulting in a bypass ratio of 5.45.

Figure 1 shows a meridional view of the Fan B component test vehicle. Immediately downstream of the rotor, a flow splitter is located which separates the fan bypass flow from the fan core flow. The axial distance between the rotor and bypass outlet guide vane (OGV), expressed in number of rotor chords, is a minimum of 2.0. The axial distance between the rotor and fan core OGV, expressed in number of rotor chords, is 1.25. No inlet guide vanes were incorporated in the configuration. The moderately low-aspect-ratio (1.71) unshrouded rotor contained 26 blades. The rotor tip and hub solidities were 1.30 and 2.16, respectively. Sixty vanes were incorporated for both the outer and inner OGV's for a vane-number-to-blade-number ratio of 2.3.

The design rotor tip relative Mach number is 1.20. The rotor blade employs a profile shape that is specifically tailored to prevent excessive shock losses on the suction surface and still be compatible from a throat area and energy addition standpoint. The blade meanline shape and point of maximum thickness vary radially. The blade is similar to a double circular arc profile in the hub region. Profile shapes at other radii are generally similar in appearance to the NASA multiple-circular arc profiles.

The profile shapes for the bypass OGV, which operates at moderate conditions of inlet Mach number and diffusion factor, were designed with a modified NASA 65 series thickness distribution on a circular arc meanline. The fan core OGV, which operates in a relatively high inlet Mach number environment when considering the turning requirement and diffusion factor level, was a tandem vane row wherein the profile shapes were specifically tailored to minimize suction surface Mach numbers and, therefore, prevent shock losses and minimize diffusion losses.

Tabulated below are some of the pertinent Mach numbers and diffusion factors for the rotors and OGV's:

Preceding page blank

			<u>Outlet Guide Vanes</u>	
	<u>Rotor</u>		<u>Bypass</u>	<u>Core</u>
Inlet Mach	OD	1.20	0.69	0.75
Number	ID	0.80	0.78	0.84
Diffusion	OD	0.376	0.425	0.474
Factor	ID	0.440	0.445	0.549

Complete design details are presented in Reference 1.

The average running rotor tip clearance at 100% speed was 0.036 inches (0.91 mm).

FOLDOUT FRAME

FOLDOUT FRAME

FOLDOUT FRAME

2

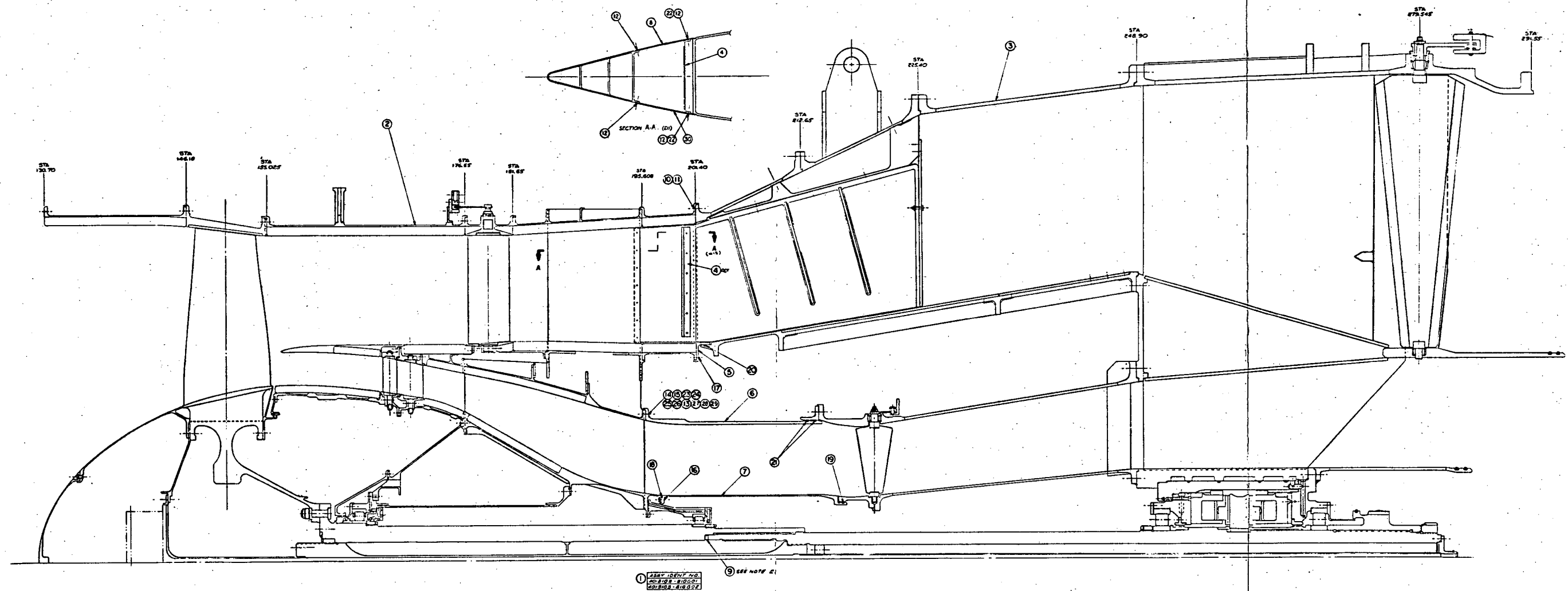


Figure 1. Fan B Component Test Vehicle Layout.

4.0 TEST SET-UP AND PROCEDURE

A. TEST FACILITY

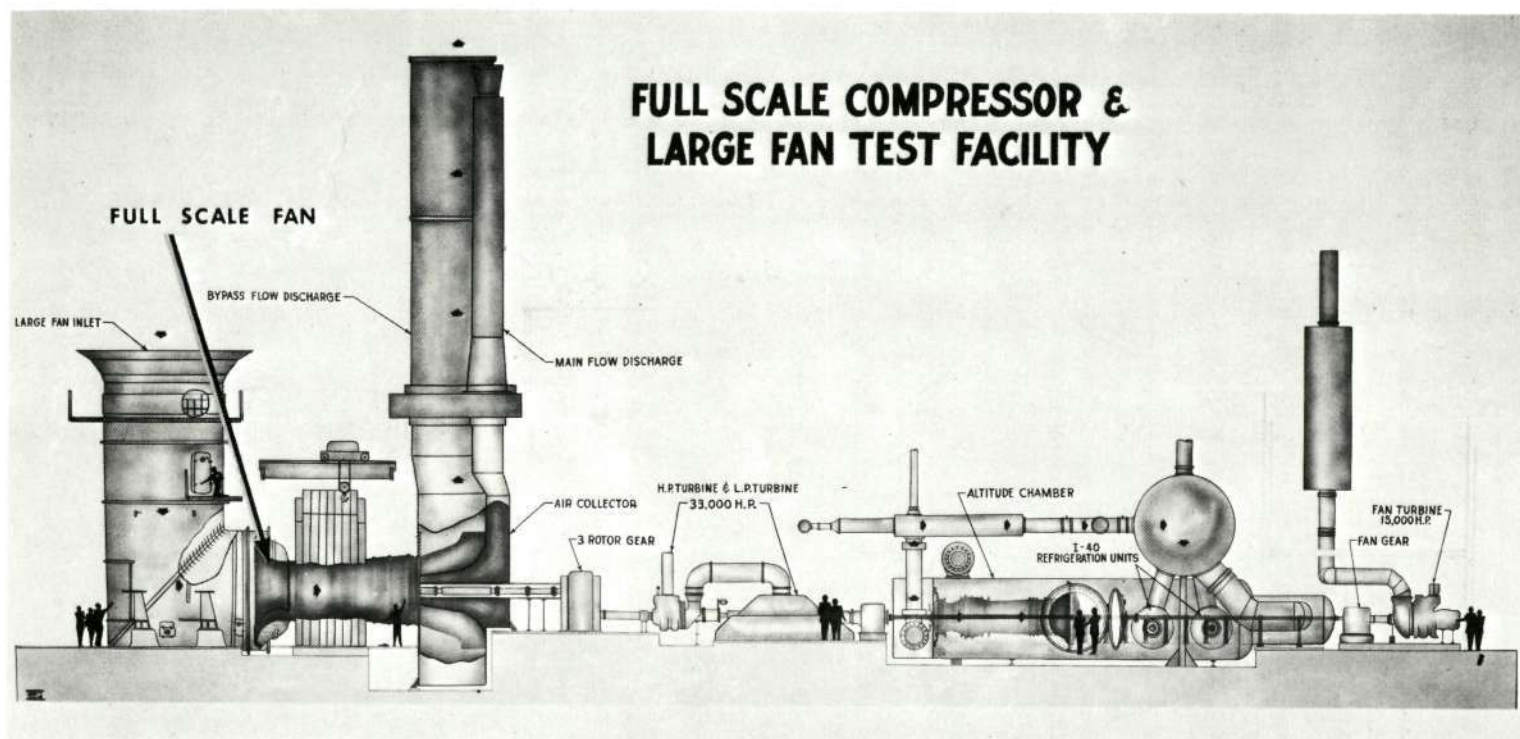
Performance tests of this fan were made in General Electric's Large Fan Test Facility, at Lynn, Massachusetts. The general aspects of the test vehicle facility installation are shown in Figure 2. The test fan draws air vertically downward from the atmosphere through a throttling device, which is located at the top of the inlet stack. The testing for this fan was performed with an open-inlet throttle except for the high-power extraction point where the facility power became limiting. The air then passes through a cascade of turning vanes and proceeds horizontally to a foreign object damage (FOD) protection screen and accelerates through an area ratio of 5.4 into the fan inlet. Downstream of the fan rotor the flow is split into a fan bypass portion and a fan core portion. The bypass flow is ducted from the vehicle discharge through an adapter into the facility where the bypass discharge valve is located. This air is collected and exhausted vertically into the atmosphere. The fan core flow is ducted from the vehicle discharge through an adapter into the facility where the main discharge valve is located. This air is collected and passed through a pipe containing a flow measurement system and is finally discharged vertically into the atmosphere. Dial indicators are attached to each of the discharge valves to indicate the relative valve position; zero indicates fully closed and 100 indicates fully open.

Power to drive the test fan is provided by a steam turbine rated at 30,000 horsepower (22.4 Mw).

B. OVERALL PERFORMANCE INSTRUMENTATION

Overall fan performance was determined from measurement of fan inlet and fan discharge total temperatures and total pressures. At fan inlet, the total pressure was measured by four six-element rakes located in the cylindrical section of the inlet duct between the bellmouth and the fan inlet. Twenty-four thermocouples attached to the inlet FOD screen were used for determination of inlet total temperatures. The pressure and temperature sensors were located approximately on centers of equal area. At fan discharge, the total temperature and total pressure were measured by circumferential arc rakes. Seven 12-element arc rakes were located behind the fan bypass OGV's and five seven-element arc rakes were located behind the fan core OGV's. In the bypass, the elements were circumferentially spaced so as to span one OGV passage for the two outermost rakes and two OGV passages for the remainder. In the fan core, the elements were circumferentially spaced to span two OGV passages. Radially, the arc rakes were located on centers of equal design mass flow of the fan bypass and fan core, respectively. A more detailed description of this and the other vehicle instrumentation is contained in Appendix I.

Preceding page blank



Reproduced from
best available copy.

Figure 2. Full-Scale Compressor and Fan Test Facility.

C. BYPASS RATIO SCHEDULE

The configuration of the Fan B test vehicle was designed to simulate the fan bypass and fan core flows through the fan frame region with independently controllable discharge valves for each portion. Cycle calculations for the Fan B engine system yielded a bypass ratio migration, as a function of fan speed, along a typical operating line. The procedure adopted for testing the Fan B vehicle was to set this bypass ratio, as a function of fan speed, for all operating points on a given speed line except those specific points aimed at determining the effects of bypass ratio swing on fan operation. The approximate total fan flow and fan core flow were calculated in real time by an analog computer and continuously displayed in the Data Recording center. These data were used as a guide in setting the bypass and core discharge valves to maintain the desired bypass ratio. Generally, the detailed reduced data showed that the bypass ratios for the test points were within 0.2 count of the desired values as is shown in Figure 3.

D. VEHICLE CONFIGURATION FOR TEST

There were three configurations tested. The initial test (build 1) had both vanes set at their design stagger angles. The rotor blades were made of 7075-T73 aluminum. Initial testing revealed that performance of the fan core outlet guide vanes was below expectations.

The fan stage was designed so that the stagger angle of all the stators could be adjusted. The stagger angle of the aft element of the tandem row fan core OGV was increased 6° so as to unload the blade row. The front element was left at the design setting. It was believed that the fairly high solidity struts in the fan core duct would remove this small amount of swirl with no significant increase in loss. This configuration is referred to as build 1A. Subsequently, titanium rotor blades were substituted for the aluminum blades; this configuration is referred to as build 2. There was no difference in the measured performance of the fan between the aluminum and titanium blade configurations except that the titanium blade could tolerate throttling to a higher limit line without exceeding acceptable stress levels in the 85 to 90% speed region. All test results presented herein are for the build 2 configuration, except as specifically noted.

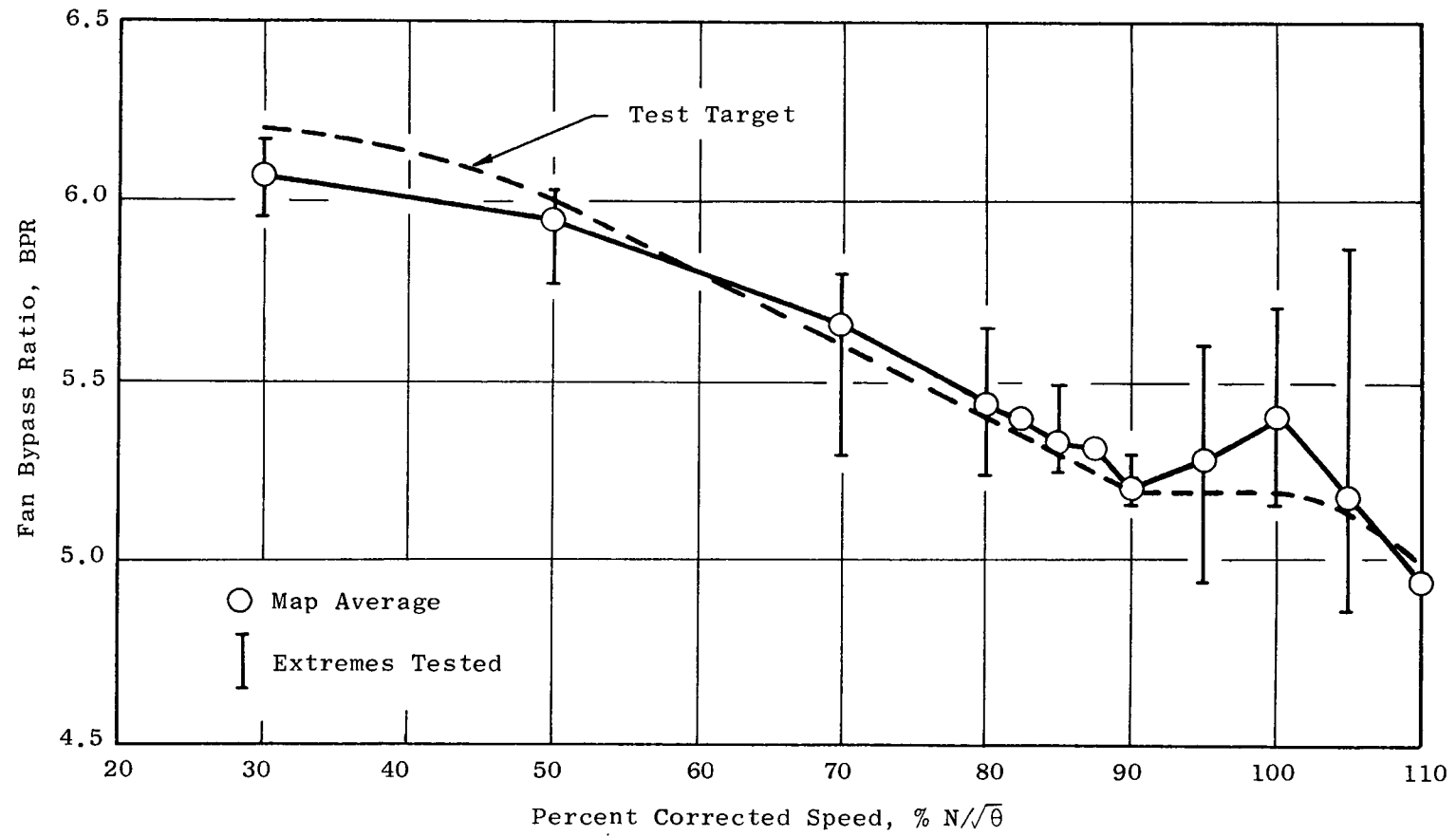


Figure 3. Fan B Component Test, Bypass Ratio Schedule.

5.0 RESULTS AND DISCUSSION

A. PRESENTATION OF OVERALL RESULTS

The basic design of Fan B incorporates radial variations in discharge total pressure and total temperature. Additionally, deviations from design intent and the migration of the fan to other operating conditions will produce differing radial variations. Accurate cycle representation of the fan component requires recognition of these variations. Accordingly, the overall fan performance is presented in the form of two maps to distinguish the performance characteristics in the fan bypass and fan core regions. One map presents fan bypass total pressure ratio and efficiency versus total fan flow. The second map presents fan core total pressure ratio and efficiency versus fan core flow. The utilization of total fan flow, rather than bypass flow, on the bypass map is somewhat arbitrary but does serve the purpose of providing an overall maximum flow constraint, at a given speed, when these maps are incorporated into the cycle performance calculations.

Presentation of the fan performance by two separate maps tends to imply that the results are independent, as would be the case if the splitter between the bypass flow and fan core flow extended forward through the rotor. This is not the case for the configuration employed by Fan B; a definite performance interdependence exists between the two streams. Although it is an oversimplification, it is meaningful to consider the case where the leading edge of the flow splitter is located aft of a single OGV which spans the entire annulus. In such a case, the OGV discharge pressure is largely controlled by the bypass discharge valve by virtue of the high-bypass ratio for the fan. At fixed bypass discharge valve settings, a change to the fan core discharge valve will directly affect its flow rate but not significantly affect the delivery pressure of the fan core flow. Also, at fixed fan core discharge valve setting, a change to the bypass discharge valve will affect the delivery pressure into the fan core duct and thereby also affects its flow rate. The actual configuration with the splitter behind the rotor is more complex than either of the two extremes because of the influence of the splitter on the operation of the core region and the off-incidence and loading conditions forced onto the OGV's. Accordingly, for each value of bypass ratio, a separate and distinct pair of performance maps will result. A series of test points were recorded to investigate the effects of off-design bypass ratio operation; the results are presented in a later section.

B. UNDISTORTED FLOW PERFORMANCE

1. Fan Bypass Region

The measured performance of the Fan B stage is shown in Figures 4 and 5. The measured flow at the design bypass pressure ratio of 1.50 was

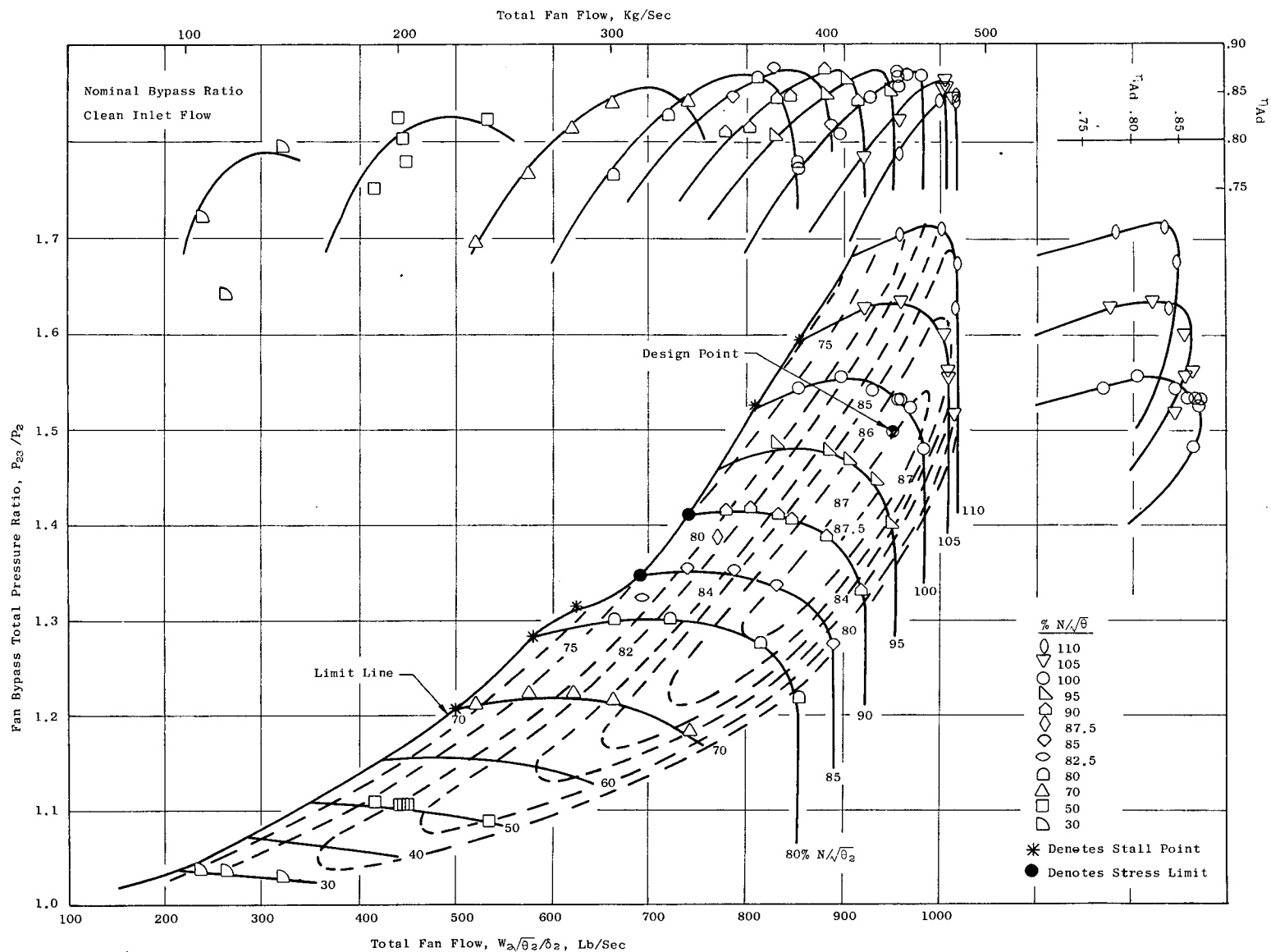


Figure 4. Fan B Performance Characteristics in the Bypass Region.

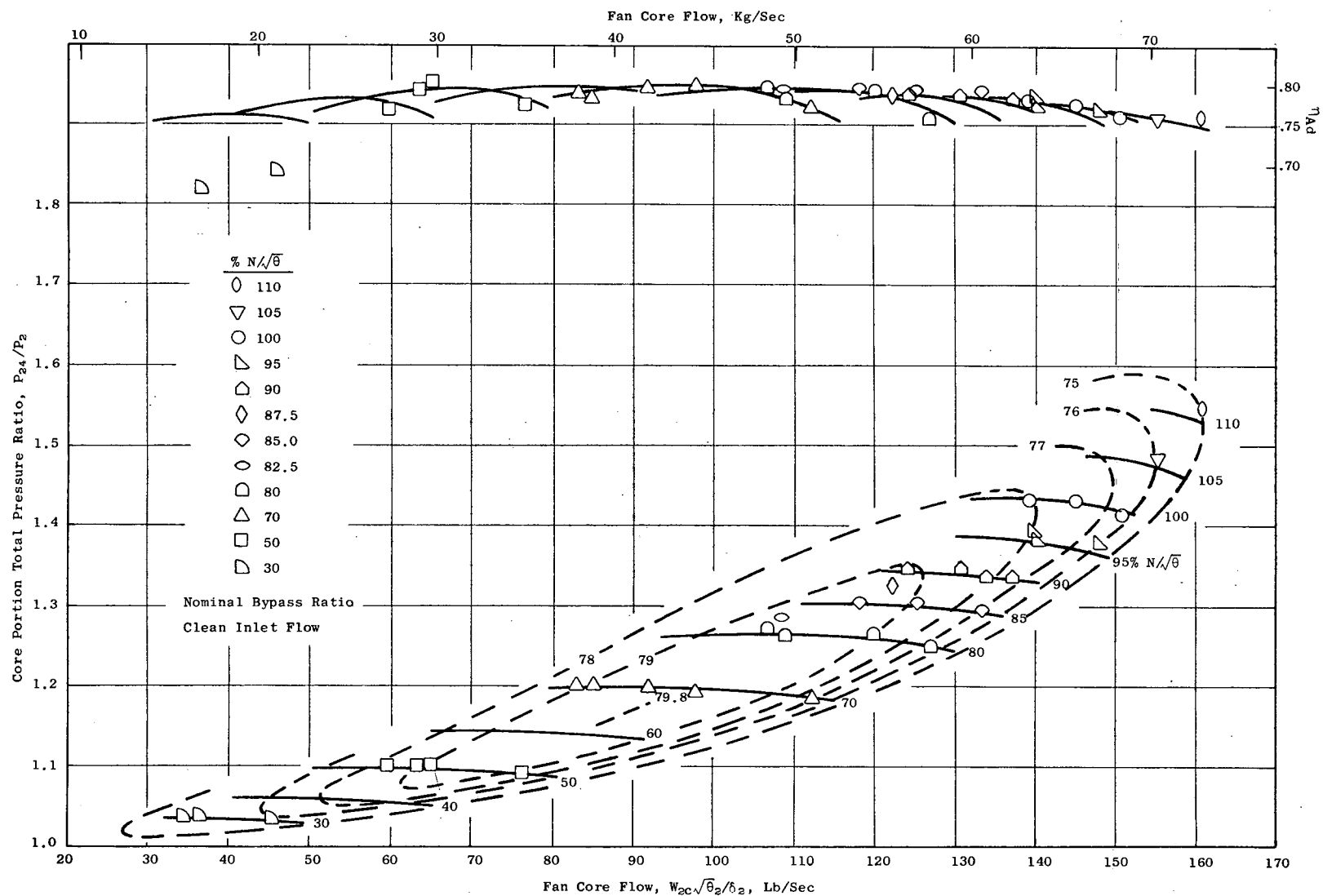


Figure 5. Fan B Performance Characteristics in the Core Region.

980 lb/sec (44.5 kg/sec), which is 3.16% greater than the design value of 950 lb/sec (430.9 kg/sec): the bypass adiabatic efficiency was 87.0%, the objective value. A more meaningful way to compare the measured performance relative to design is at the intersection of a constant throttle area line passing through the design point and the 100% corrected speed line. This method is significant since it reflects the manner in which the fan would operate in an engine system. At this point, the measured flow was 966 lb/sec (438.2 kg/sec) at a pressure ratio of 1.52. The bypass adiabatic efficiency was 86.9%. The peak efficiency at design speed was 87.1% at a bypass pressure ratio of 1.507 and a total fan flow of 976 lb/sec (442.7 kg/sec). At 110% corrected speed, a flow of 1020 lb/sec (462.7 kg/sec) was achieved, a specific flow of 44.3 lb/sec/ft² (211.5 kg/sec/m²) of annulus area.

The operational limit line was determined up to, and including, 100% corrected speed. The operational limit was determined to be rotating stall at all corrected speeds except 85 and 90% where high rotor stress precluded further increases in back pressure. The operational limit line was not determined at 30 and 50% corrected speed on build 2; the limits shown on the compressor map in this speed range were obtained from build 1. The operating margin* achieved at 100% corrected speed relative to the design operating line at altitude cruise conditions was 19.5%. At 90% corrected speed the operating margin was 10.9% relative to the design operating line at sea level static conditions.

2. Fan Core Performance

The fan was designed to deliver a core pressure ratio of 1.43 at a core flow of 147.3 lb/sec (66.8 kg/sec). The proper selection of the map point for comparison with the design objectives is less obvious for the fan core performance than for the bypass performance since the match point for the core is not necessarily along a constant throttle area line but, instead, depends upon the overall engine operating characteristics. Selecting the objective core flow at 100% corrected speed, a core pressure ratio of 1.425 was achieved. At this condition the core adiabatic efficiency was 77.0%. A peak adiabatic efficiency of 79.8% was achieved in the 60 to 70% corrected speed range.

The terminations of the constant speed lines on the low-flow side was arbitrarily made consistent with the average bypass ratio from Figure 3 and the total fan flow limit from the bypass map. These terminations do not represent an operating limit of the fan core map. Several data

$$* \text{ operating margin} = \left\{ \frac{\left| \frac{W}{P_{23}} \right| \text{ at operating line}}{\left| \frac{W}{P_{23}} \right| \text{ at stall}} - 1 \right\} \times 100; \% \text{ at constant speed}$$

points on the high-flow side of the constant speed lines in the high corrected speed range are not shown on the fan core map. The flow passing capacity of the facility (core portion) was found to be limiting for these conditions, and these points departed markedly from the bypass ratio of the remainder of the speed line. Once the fan core discharge valve is fully open, any reduction in fan discharge pressure, as a result of opening the bypass discharge valve, reduces the weight flow through the fan core. Under these conditions the fan core speed line appears to double back to lower flows as the back pressure is reduced. This characteristic is not consistent with the intended core map representation and tends to be misleading. Furthermore, since it was the intent to maintain a constant bypass ratio at each speed, a vertical bypass speed line results in a vertical fan-core speed line. A vertical fan-core speed line generated in this manner does not necessarily imply a choke condition in the core stream.

The measured fan core efficiency was below design objectives. The moderately high rotor hub loading and the high fan core OGV inlet Mach number and loading are contributing factors. The larger radial extent for which thick blade profile sections were employed (to ensure that the natural frequency of the blade does not coincide with a vibration stimulus occurring once per revolution) is a consideration. It is also the case, for high bypass ratio fans in general, that a significant portion of the fan core flow is what would normally be classified as the "end wall" flow from the fan blade. For the Fan B configuration, the height of fan core duct expressed as a ratio to the staggered spacing of the fan blade, a significant dimension when analyzing end wall flows, is 0.83. Figure 6 shows the radial efficiency profile at stage discharge as deduced from the discharge arc rake instrumentation. Shown on this figure is an assumed efficiency profile for a redesigned configuration without a splitter. Also shown are the locations of seven arc rakes used for the efficiency evaluation of this hypothetical fan. It is observed that the actual instrumentation density in the fan core tends to emphasize the low efficiency end wall flow relative to measurements of the more conventional hypothetical fan.

As a part of the data analysis performed on Fan B, the efficiency, total pressure and temperature, OGV total-pressure-loss, and static-pressure-rise coefficients were computed for each arc rake immersion as described in Appendix II. Radial plots of this information for three points at 100% corrected speed are shown in Figures 7 through 9. Also shown in Figure 10 is a similar radial plot, at 100% corrected speed near the operating line, of build 1 data for comparison. Referring to Figure 7, which shows build 2 data for a point near the operating line, the bypass stage efficiency is lower in the end wall region but higher in the free stream region than design. This is consistent with the General Electric design policy which does not design for the entire velocity drop-off which occurs deep within the end wall region but instead tends to distribute these losses across the span. The bypass OGV total-pressure-loss coefficient, related to the difference between rotor and stage efficiency, is relatively consistent with design intent except at the vane ends. It is believed

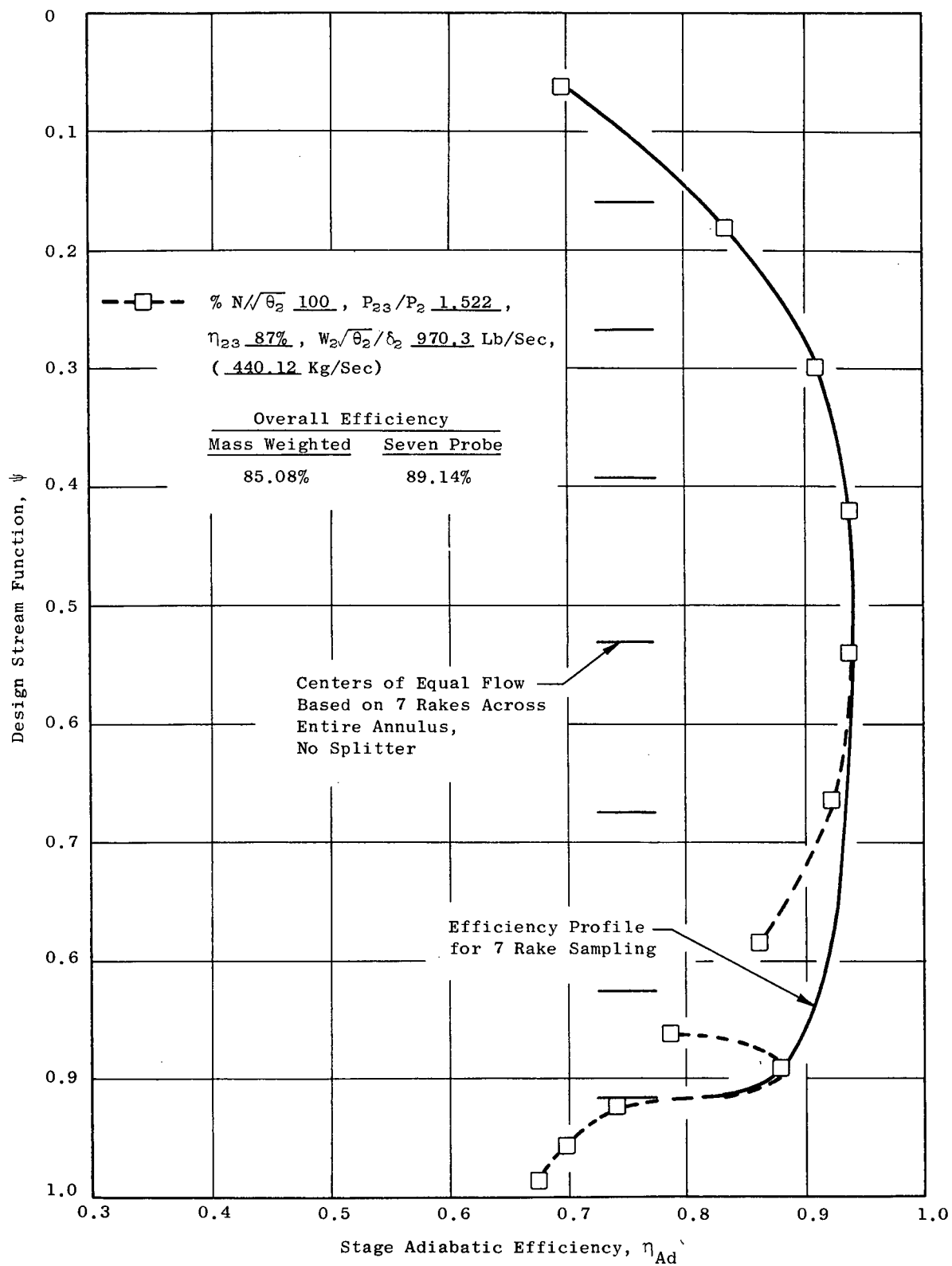


Figure 6. Radial Efficiency Profile at Discharge.

$\% N/\sqrt{\theta_2}$ 99.88 , P_{23}/P_2 1.530 , P_{24}/P_2 1.415 , $W_2\sqrt{\theta_2}/\delta_2$ 959.84 Lb/Sec
 (435.38 Kg/Sec), η_{Ad23} 87.24 % , η_{Ad24} 76.15 %

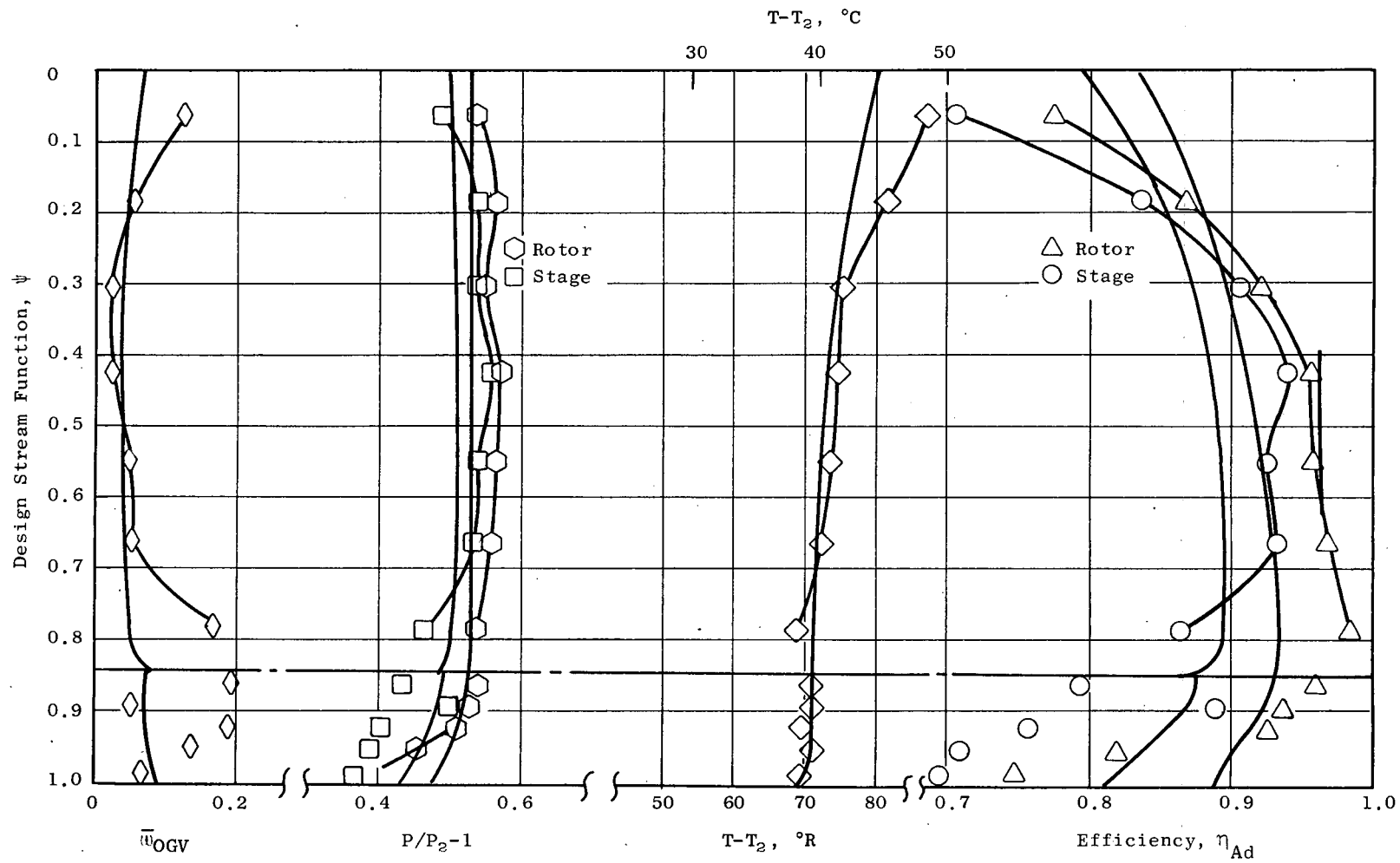


Figure 7. Radial Profiles.

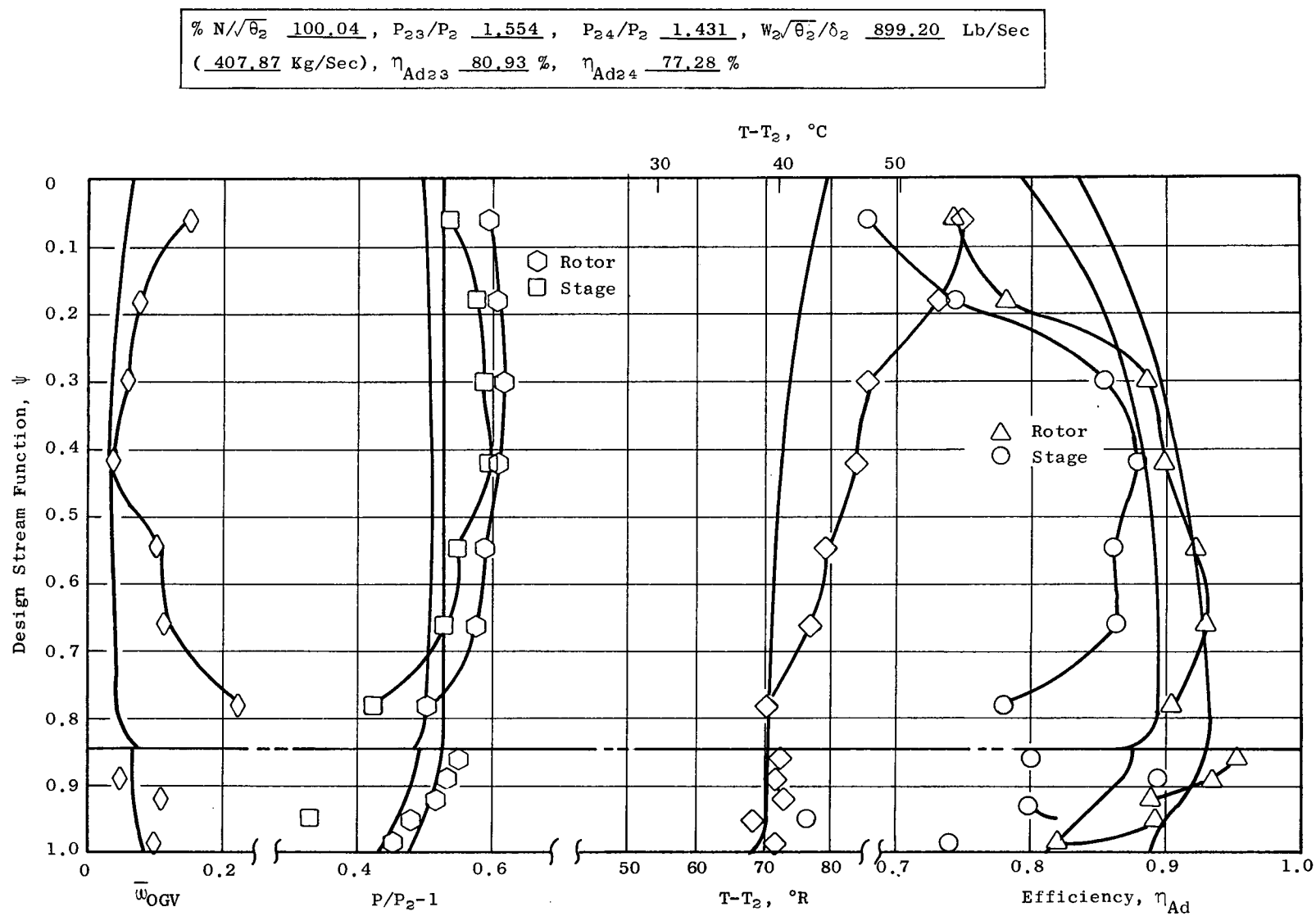


Figure 8. Radial Profiles.

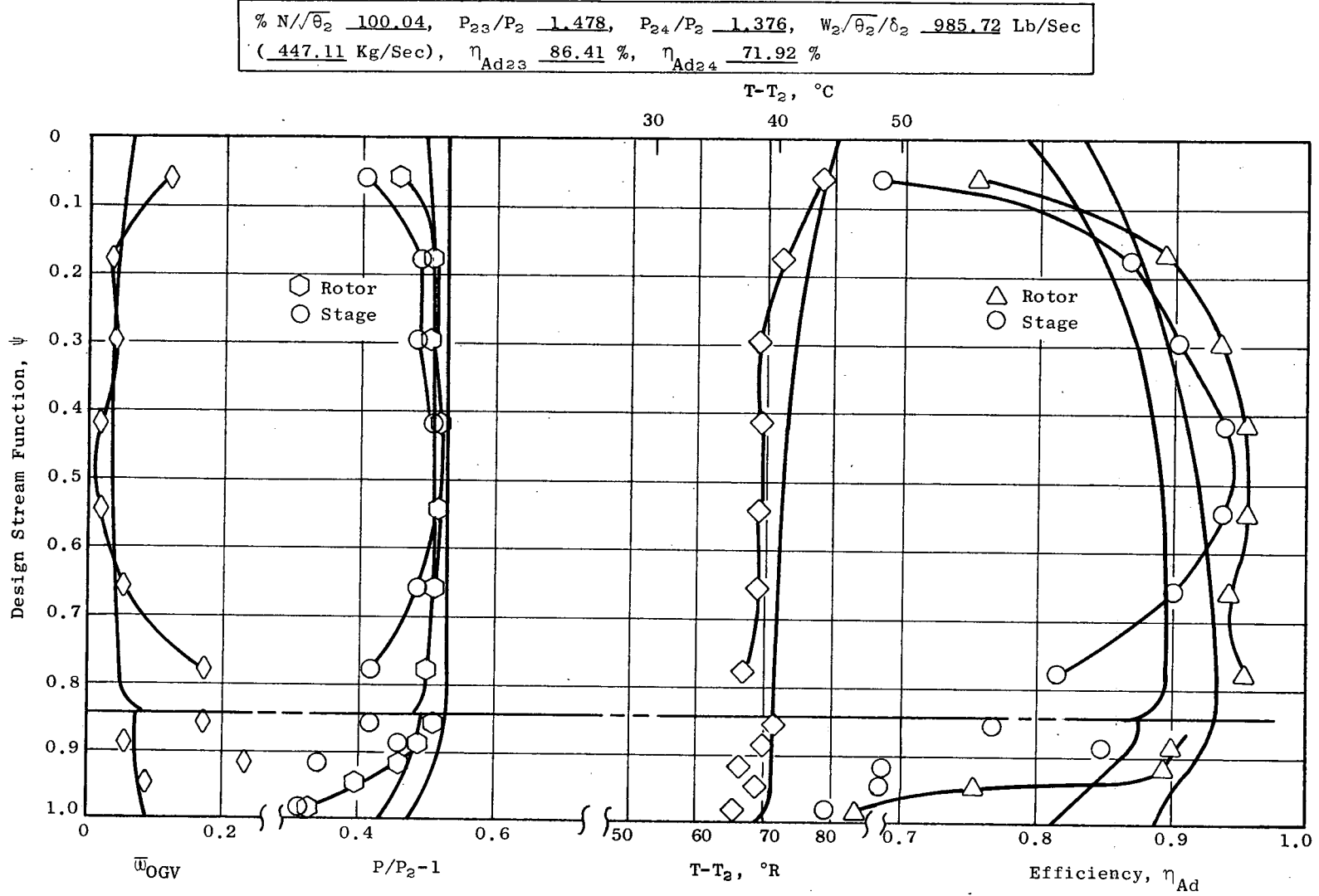


Figure 9. Radial Profiles.

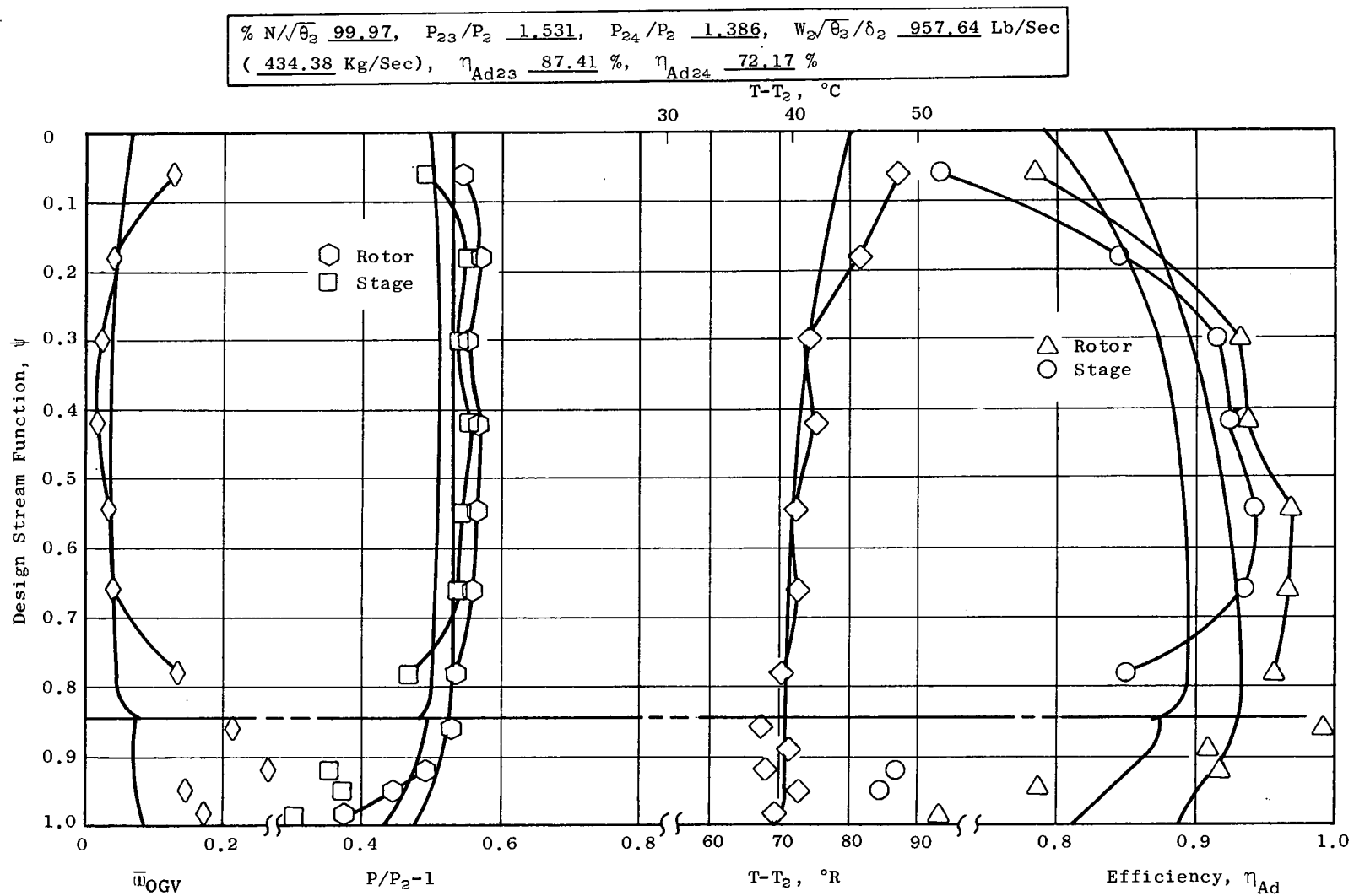


Figure 10. Radial Profiles, Build 1.

that the larger than design losses at the outside diameter and inside diameter of the OGV is caused by the relatively thick boundary layer entering the vane row as a result of the larger than normal axial spacing between the rotor and OGV, approximately 21 inches (0.53 m). In the fan core region, the rotor exit total temperature profile shows that the design work input was achieved. However, the total pressure profile tails off relative to design intent showing that the work input was not accomplished efficiently, as is shown also by the efficiency profile. The core OGV total-pressure-loss coefficients are high even though a significant improvement was observed relative to build 1, see Figure 10. The radial distribution of total-pressure-loss coefficient is peculiar in that the midimmersions show some of the highest losses whereas the end immersions normally show the higher losses. This may very well be caused by large secondary flows which are present in the low-aspect-ratio vane row.

The rotor and stage efficiency, OGV total-pressure-loss and static-pressure-rise coefficients are plotted against ideal throttle area for immersions 1, 3, 5, and 7 (which correspond to stream functions of 0.06, 0.30, 0.54 and 0.78, respectively) in the fan bypass and for each of the five immersions in the fan core (which correspond to stream functions of 0.86, 0.89, 0.92, 0.95, and 0.98) in Figures 11 through 19. The bypass throttle area on these figures is the nozzle throat area required to pass the bypass flow, assuming an isentropic expansion from measured discharge total pressure and total temperature, to ambient static pressure. For the bypass, the peak rotor efficiency and minimum OGV total-pressure-loss coefficient for each immersion occurs in the near vicinity of the design throttle area indicating that this portion of the fan is well matched radially. The outer two immersions of the fan core behave similarly. The inner two immersions of the fan core show a large improvement in rotor efficiency with throttling; the peak efficiency being observed at the most highly throttled point. Immersions 3 and 4 show a marked decrease in the OGV total-pressure-loss coefficient with increased throttling. This observation tends to be inconsistent with the result that the fan core OGV loading reduction between build 1 and build 2 resulted in a significant efficiency improvement. However, caution must be used in the literal acceptance of the decreased total-pressure-loss coefficients because of the strong three-dimensional flows present in the low-aspect-ratio OGV.

3. Bypass Ratio Excursion

Tolerance of the fan to off-design bypass ratio operation was systematically investigated as a part of the test investigation on Fan B. This investigation was performed on build 1A with a square-celled distortion screen support structure installed in the inlet. The distortion screen support structure was approximately 6 inches (15.2 cm) deep in the direction of flow with 8-inch (20.3 cm) square cells formed by 3/16-inch-thick (0.48 cm) plates. Except for the wakes from the support structure, the fan inlet conditions were not changed from the clean inlet testing. Although absolute levels of inlet and exit pressure for these tests may have been somewhat

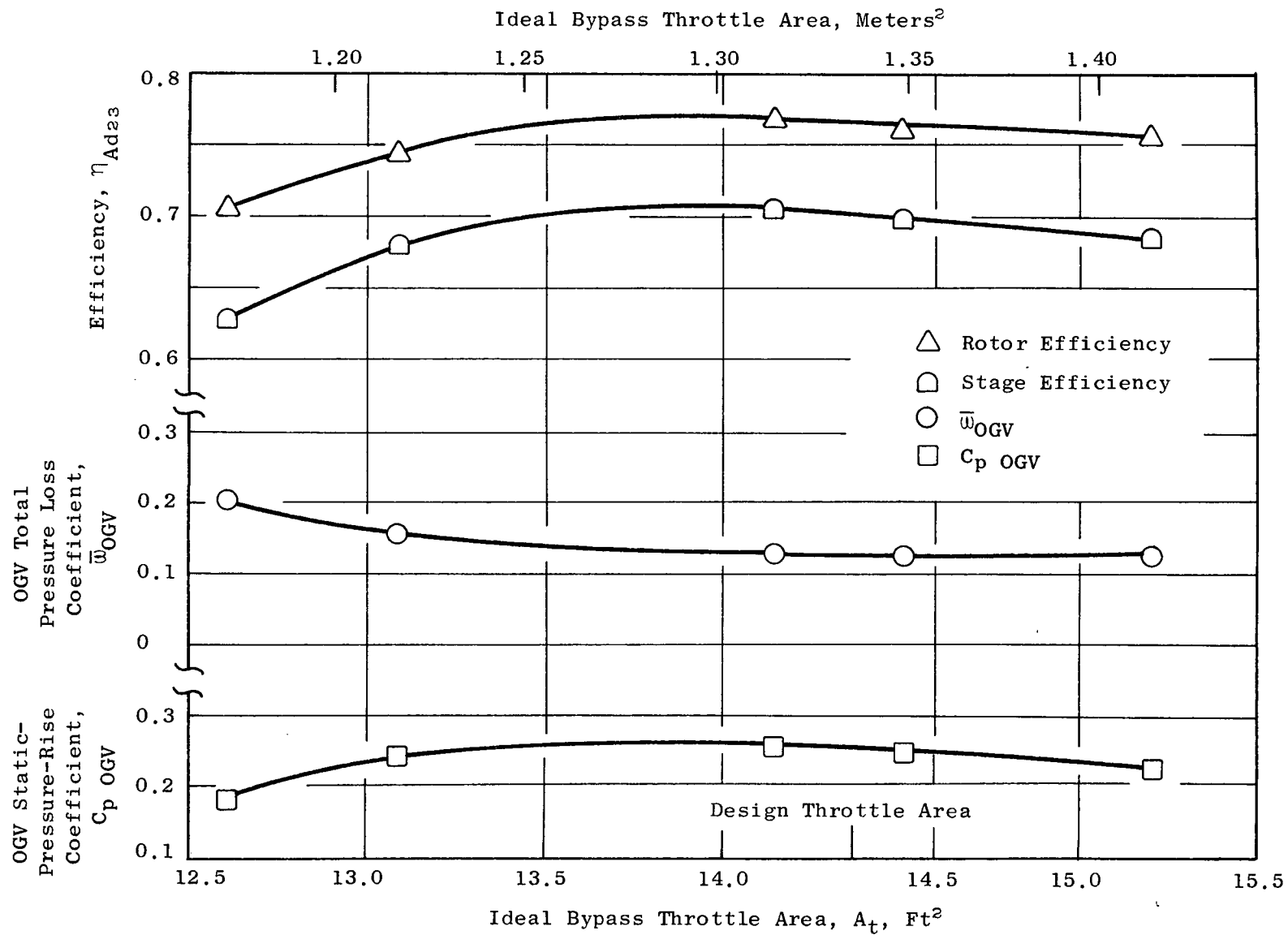


Figure 11. Variation of Element Properties with Throttling, Design Stream Function = 0.06 (Bypass OD, Immersion 1).

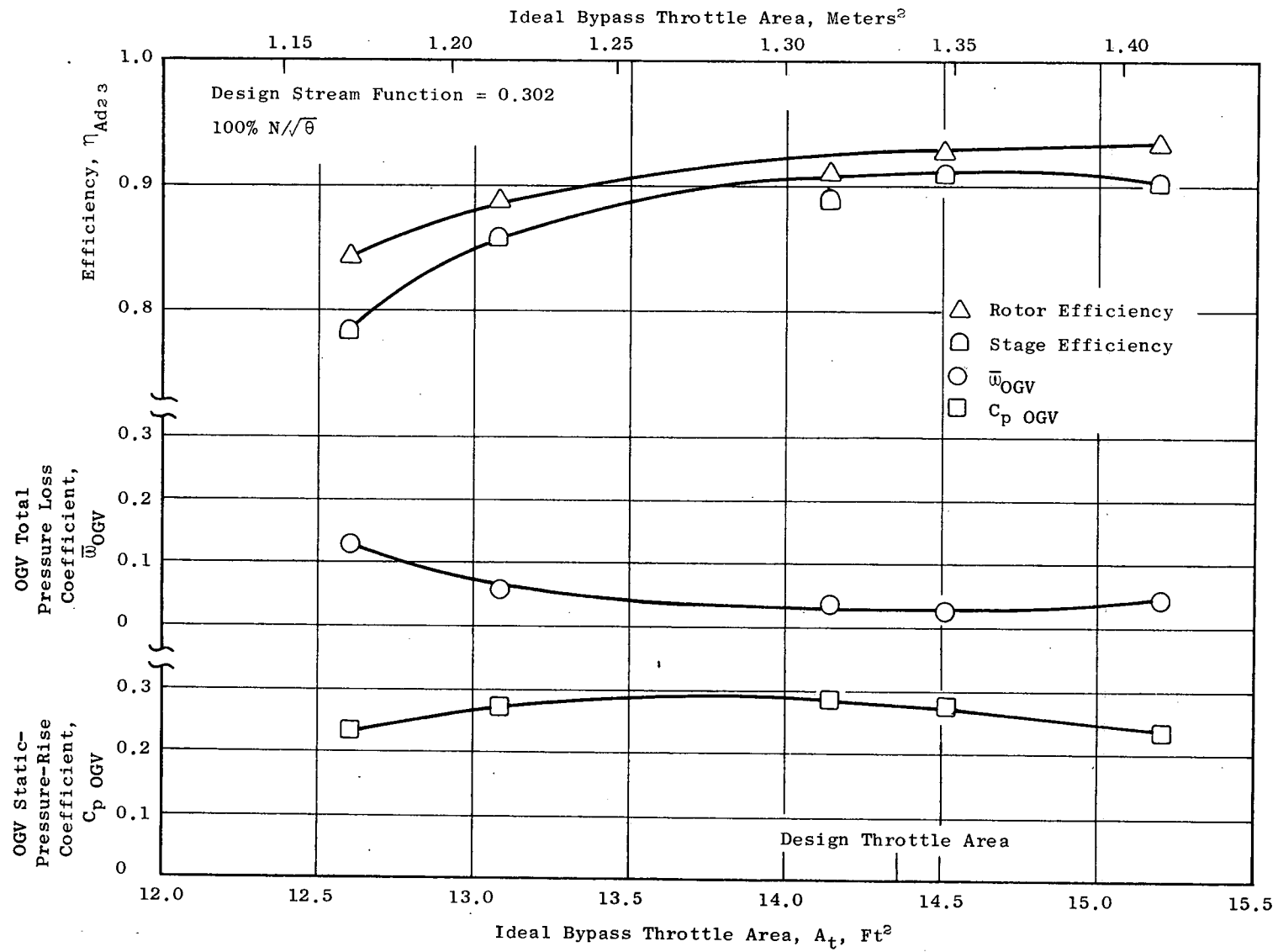


Figure 12. Variation of Element Properties with Throttling, Design Stream Function = 0.302 (Bypass Immersion 3).

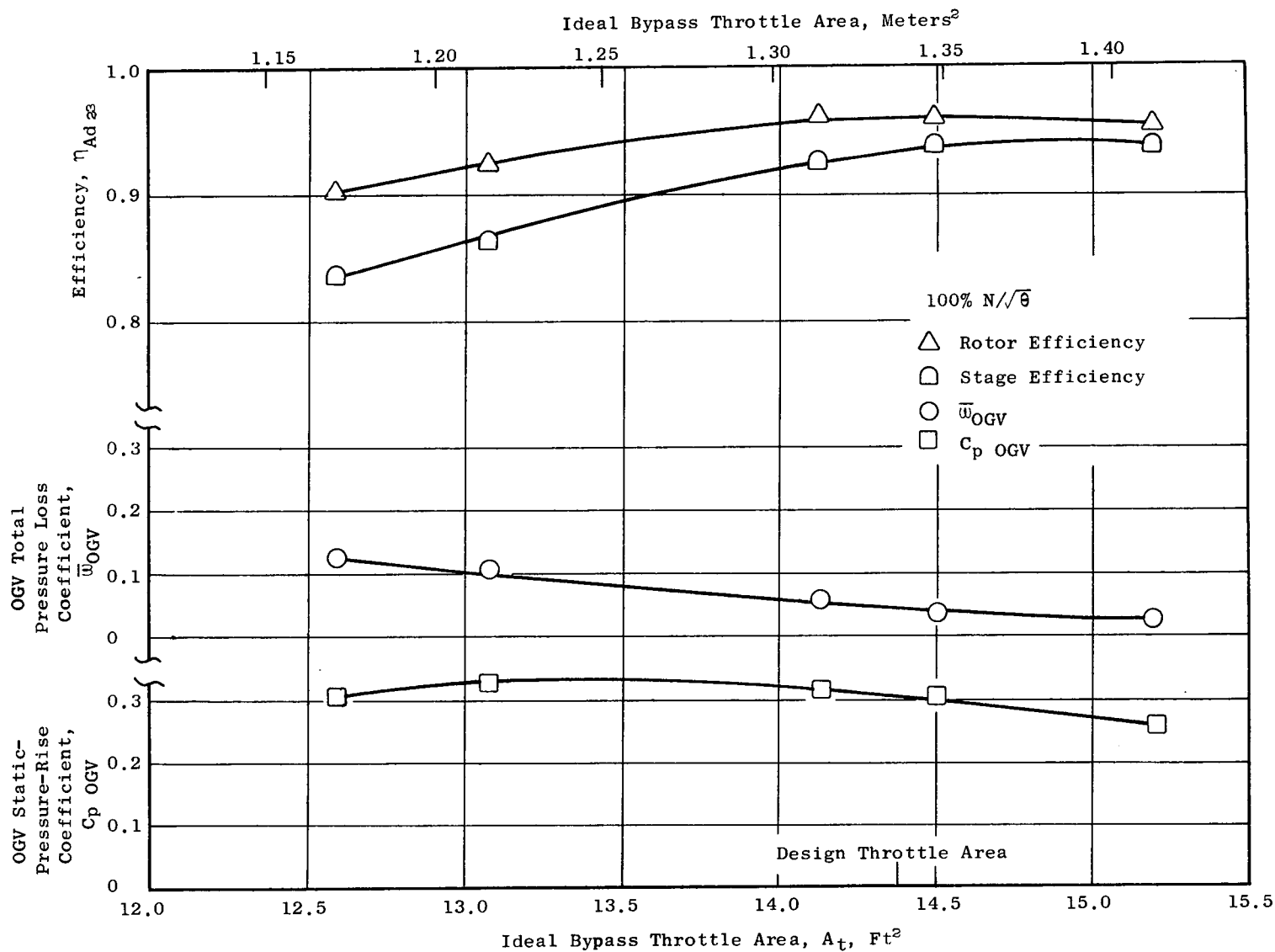


Figure 13. Variation of Element Properties with Throttling, Design Stream Function = 0.543 (Bypass Immersion 5).

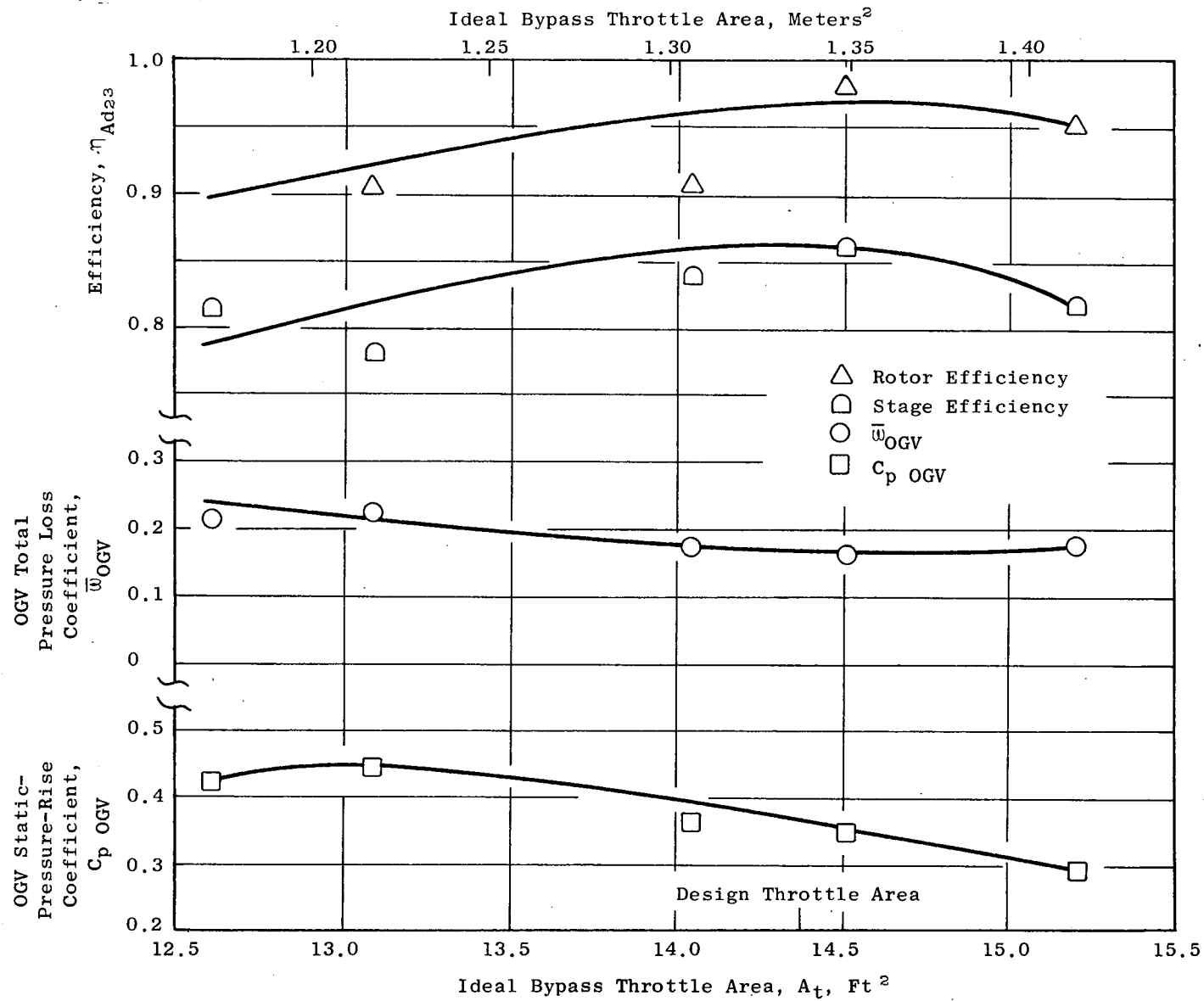


Figure 14. Variation of Element Properties with Throttling, Design Stream Function = 0.785 (Bypass ID, Immersion 7).

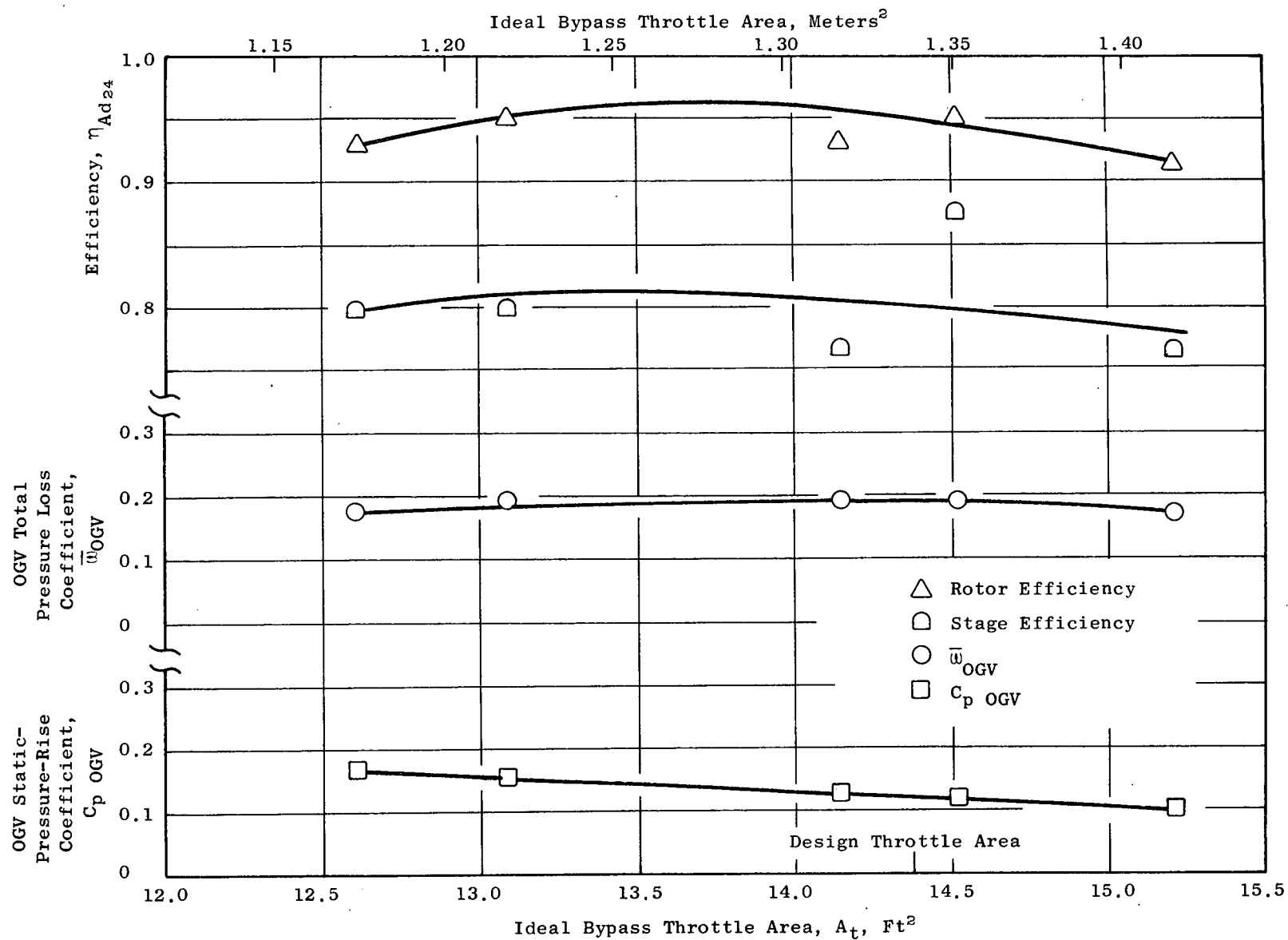


Figure 15. Variation of Element Properties with Throttling, Design Stream Function = 0.861 (Core OD, Immersion 1).

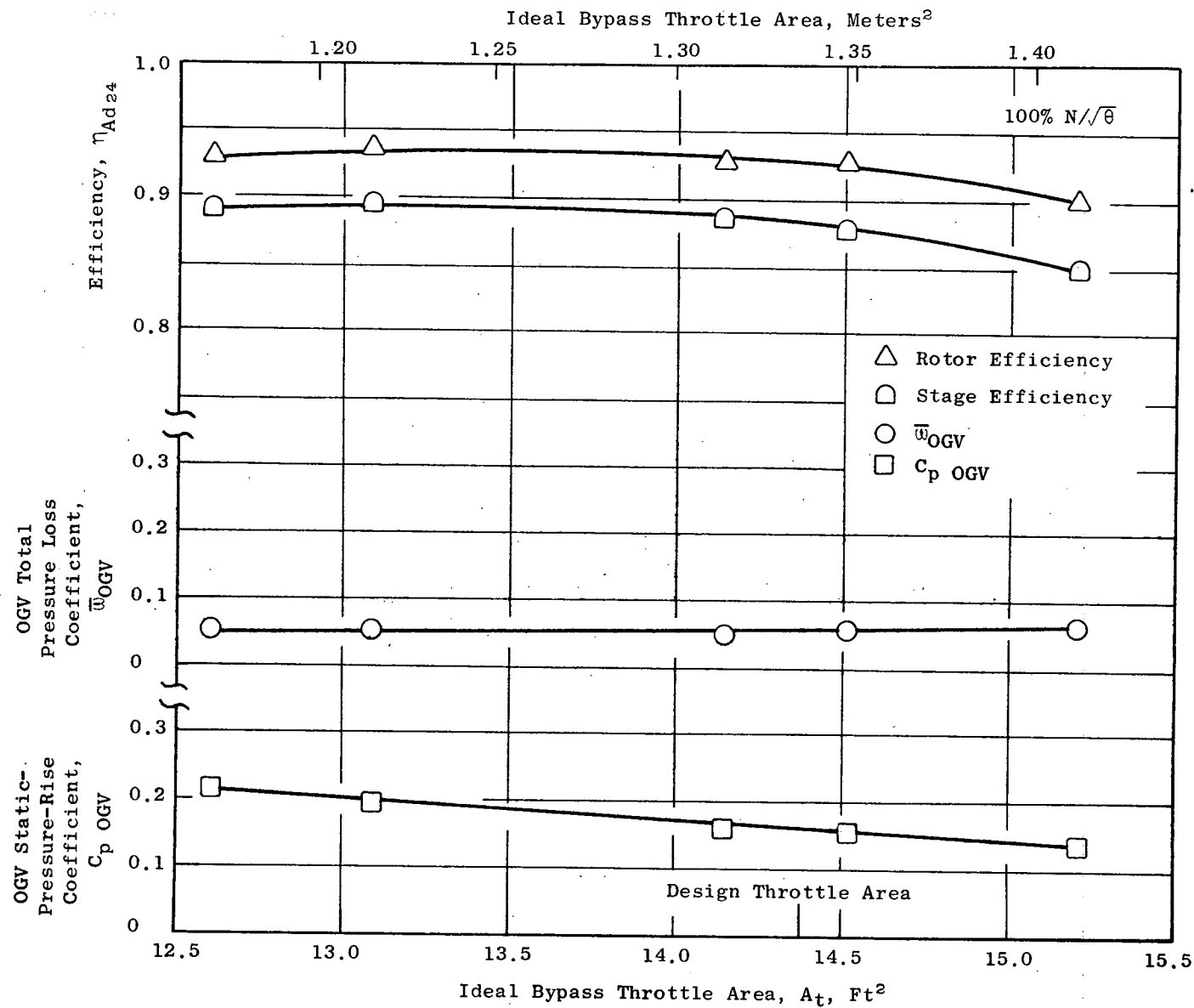


Figure 16. Variation of Element Properties with Throttling, Design Stream Function = 0.892 (Core Immersion 2).

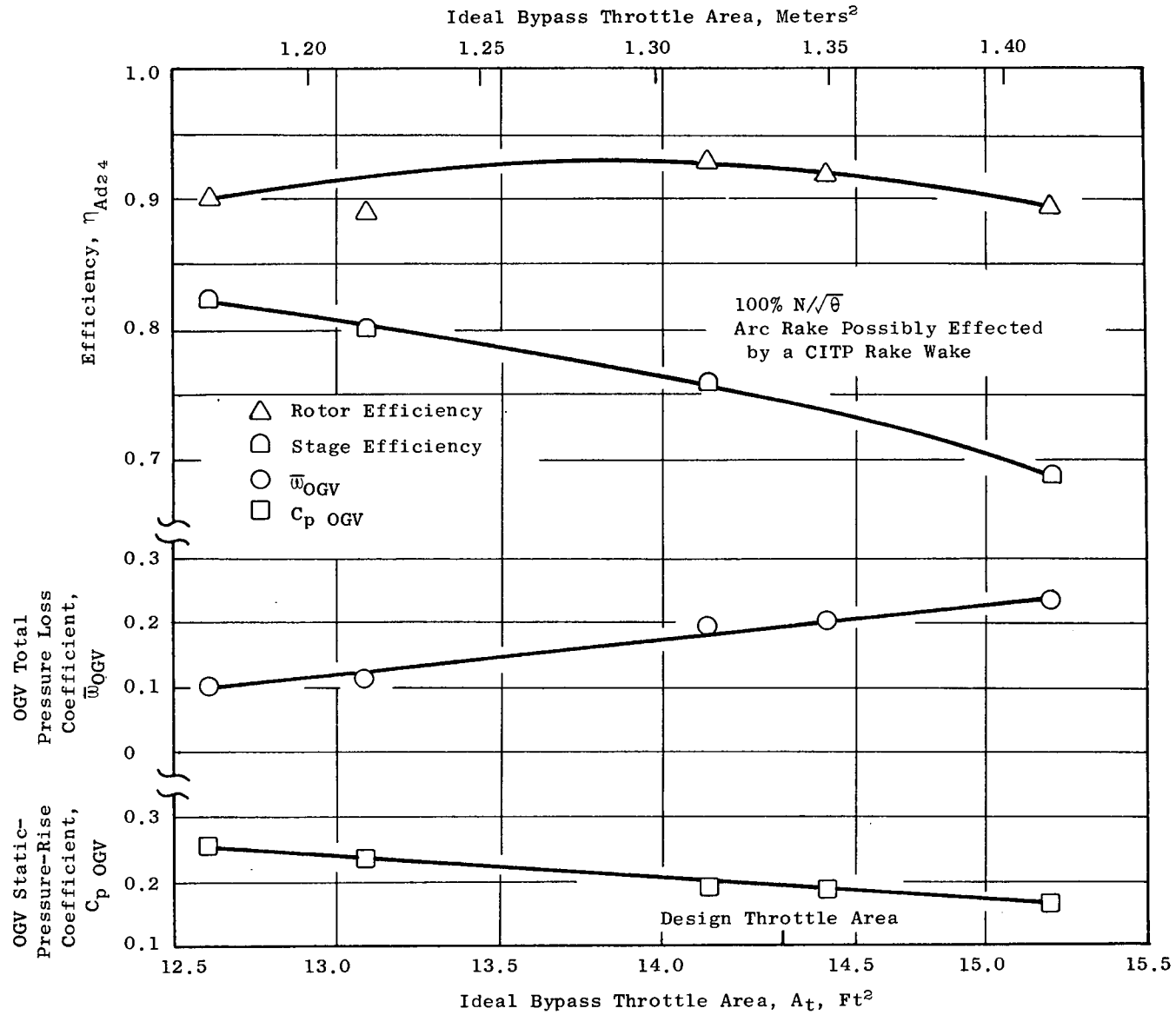


Figure 17. Variation of Element Properties with Throttling, Design Stream Function = 0.923 (Core Immersion 3).

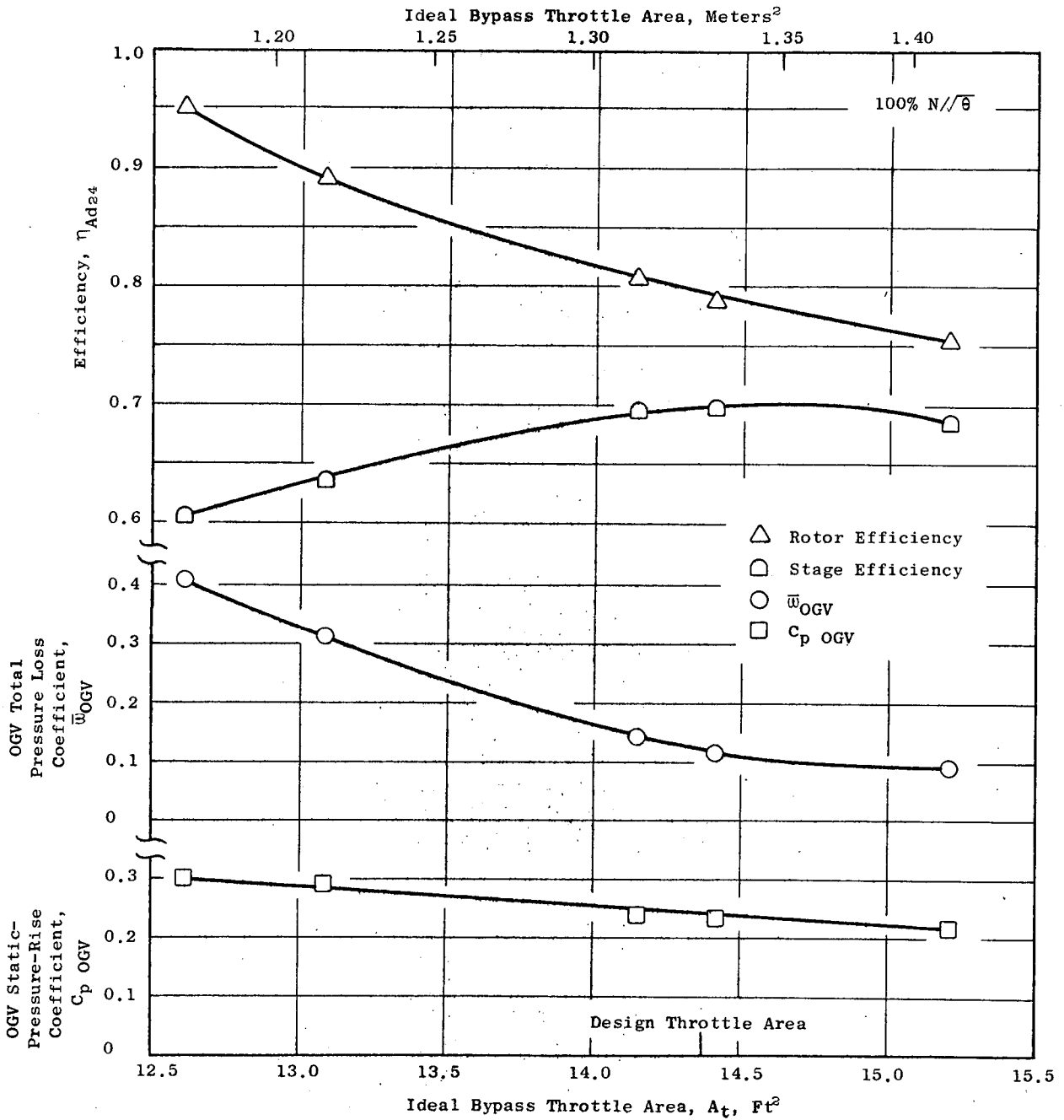


Figure 18. Variation of Element Properties with Throttling, Design Stream Function = 0.954 (Core Immersion 4).

Re

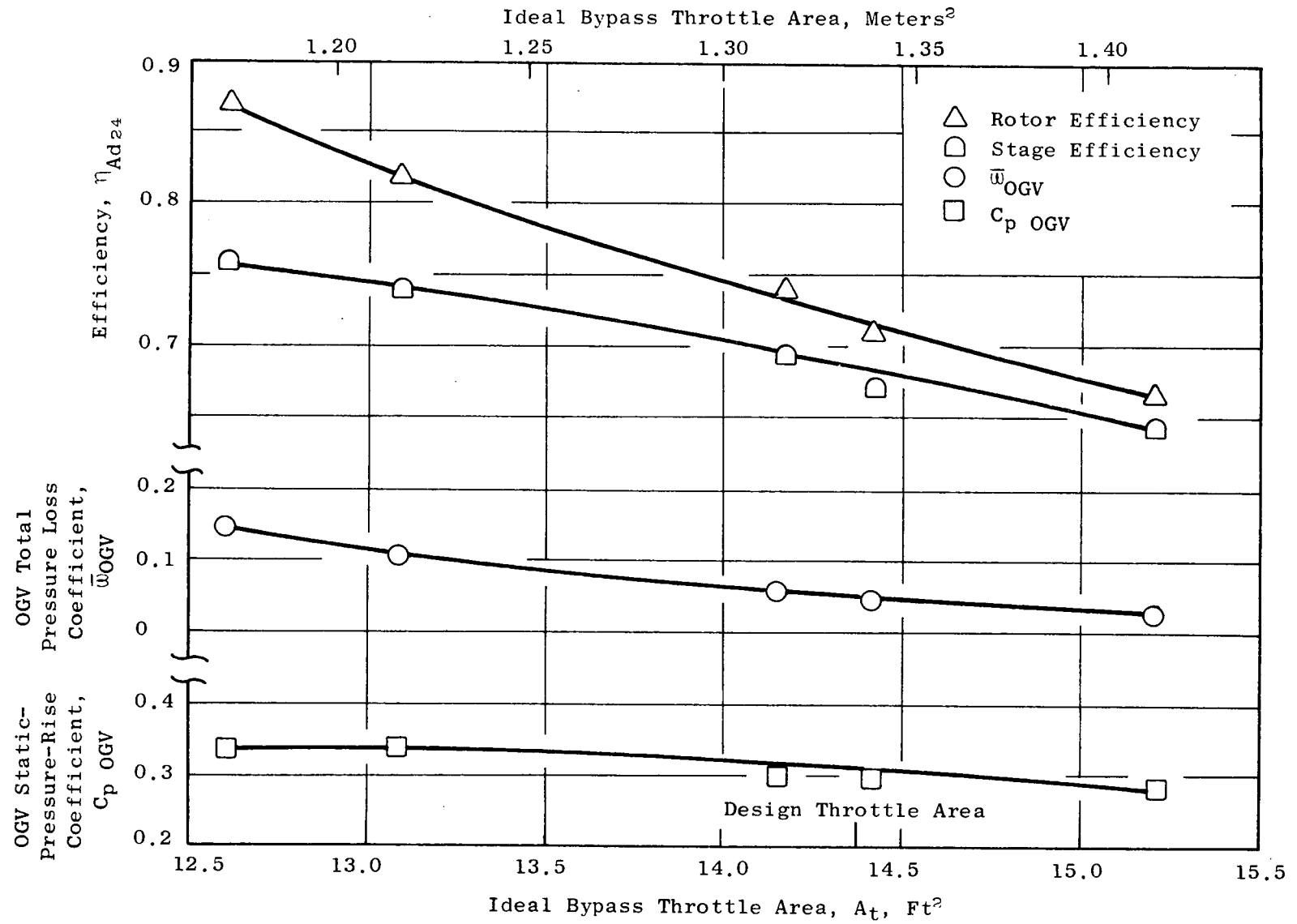


Figure 19. Variation of Element Properties with Throttling, Design Stream Function = 0.985 (Core ID, Immersion 5).

affected by screen support friction losses, the trends of these data are believed valid. A fan corrected speed of 90% was selected as representative, and for each of three bypass discharge valve settings, readings were taken for four fan core discharge valve settings. The overall performance maps are shown in Figures 20 and 21. Superimposed on these performance maps are lines of constant bypass ratio. The peak efficiency bypass ratio is observed to be approximately 5.5; the design bypass ratio was 5.4. For increased bypass ratios, Figure 21 shows that the core portion suffers large efficiency losses while the bypass portion (Figure 20) has only moderate losses. This resulted because, to simulate engine operation, the core discharge valve variation employed was much greater than that of the bypass valve. At the highest bypass ratios, the core portion incidence angles and diffusion factors were significantly greater than their design values, particularly for the outlet guide vanes, and the splitter was subjected to a high enough incidence to cause high losses on its upper surface, implying flow separation there.

The stage and rotor efficiencies, OGV total-pressure-loss and static-pressure-rise coefficients were computed, as described in Appendix II, for each arc rake immersion at a bypass discharge valve setting 39.6, which is near the nominal operating line, of the bypass ratio investigation. The instrumentation matrix employed during this investigation manifolded the individual rake elements for the outer three immersions of the bypass flow which precludes the computation for these immersions. The results of these computations are shown in Figures 22 through 30. The immersion for each of the figures is identified in terms of its design stream function, 0 being the OD, 0.84 being the splitter, and 1.0 being the ID. Referring to Figures 22 through 25, which correspond to the inner portion of the bypass flow, only very modest changes to stage and rotor efficiency and OGV total-pressure-loss and static-pressure-rise coefficients are observed. This indicates that the bypass configuration is tolerant to bypass ratio migrations, at least over the range tested, and that no significant flow breakdown occurs. Referring to Figures 26 through 30 for the fan core, the two innermost elements actually indicate an improvement in the rotor core efficiency as the fan core flow is reduced and bypass ratio increased. The performance of the fan core OGV deteriorates, however, such that the element stage efficiency actually deteriorates. (Of a total of seven elements on the 0.985 stream function arc rake, only three of the elements were reading properly which undoubtedly affects the accuracy of results for this immersion.) Although some evidence of flow breakdown in the inner OGV is present as bypass ratio increases, it is not of sufficient magnitude, over the range of bypass ratio tested, to cause any significant engine operational problems. Furthermore, continuous monitoring of blade and vane vibratory stresses and high-response pressure transducers flush mounted in the casing over the fan tip and in the core flowpath did not indicate a fluctuating flow field as would be caused by a rotating stall zone.

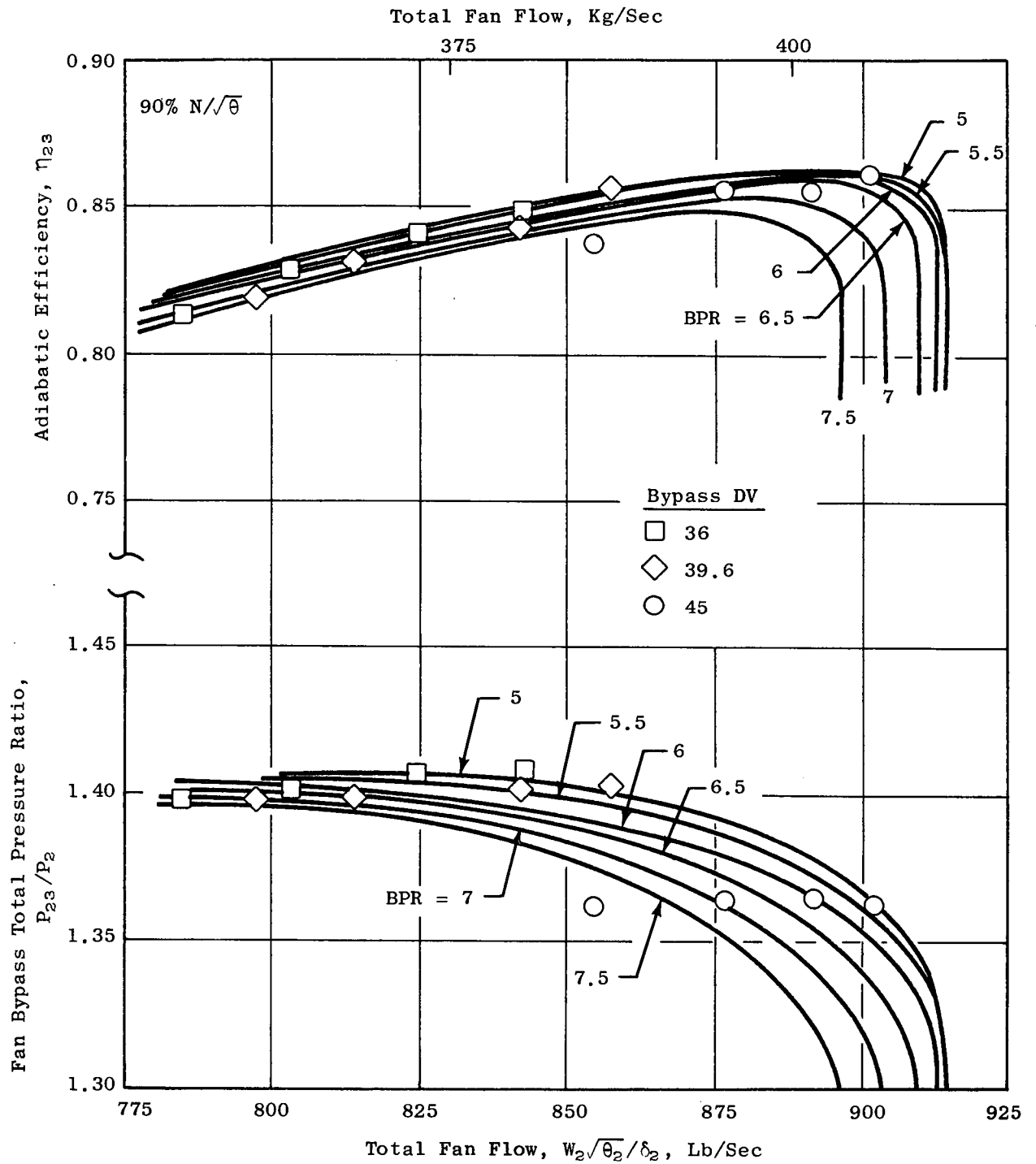


Figure 20. Bypass Ratio Excursion, Bypass Performance.

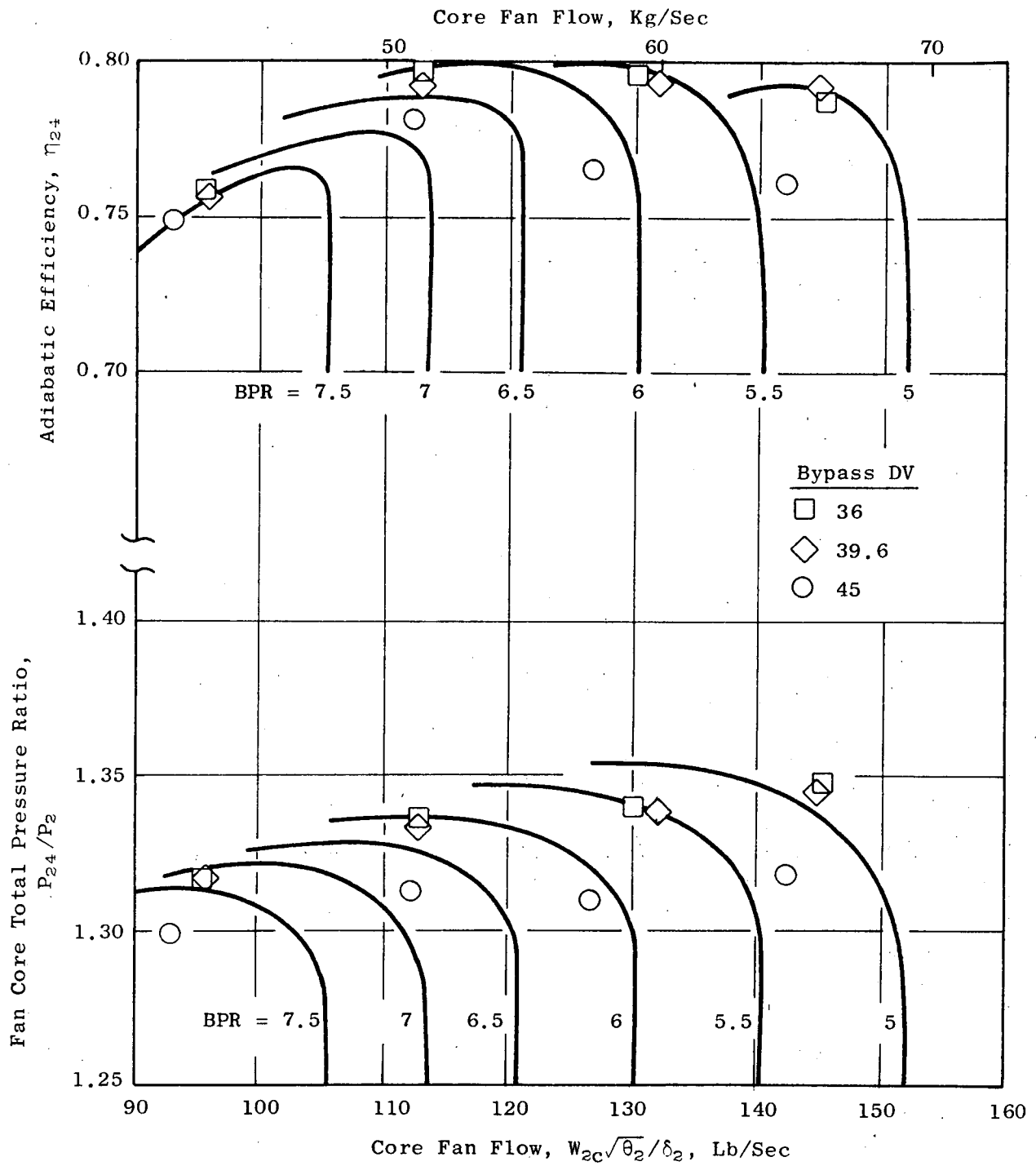


Figure 21. Bypass Ratio Excursion, Core Performance.

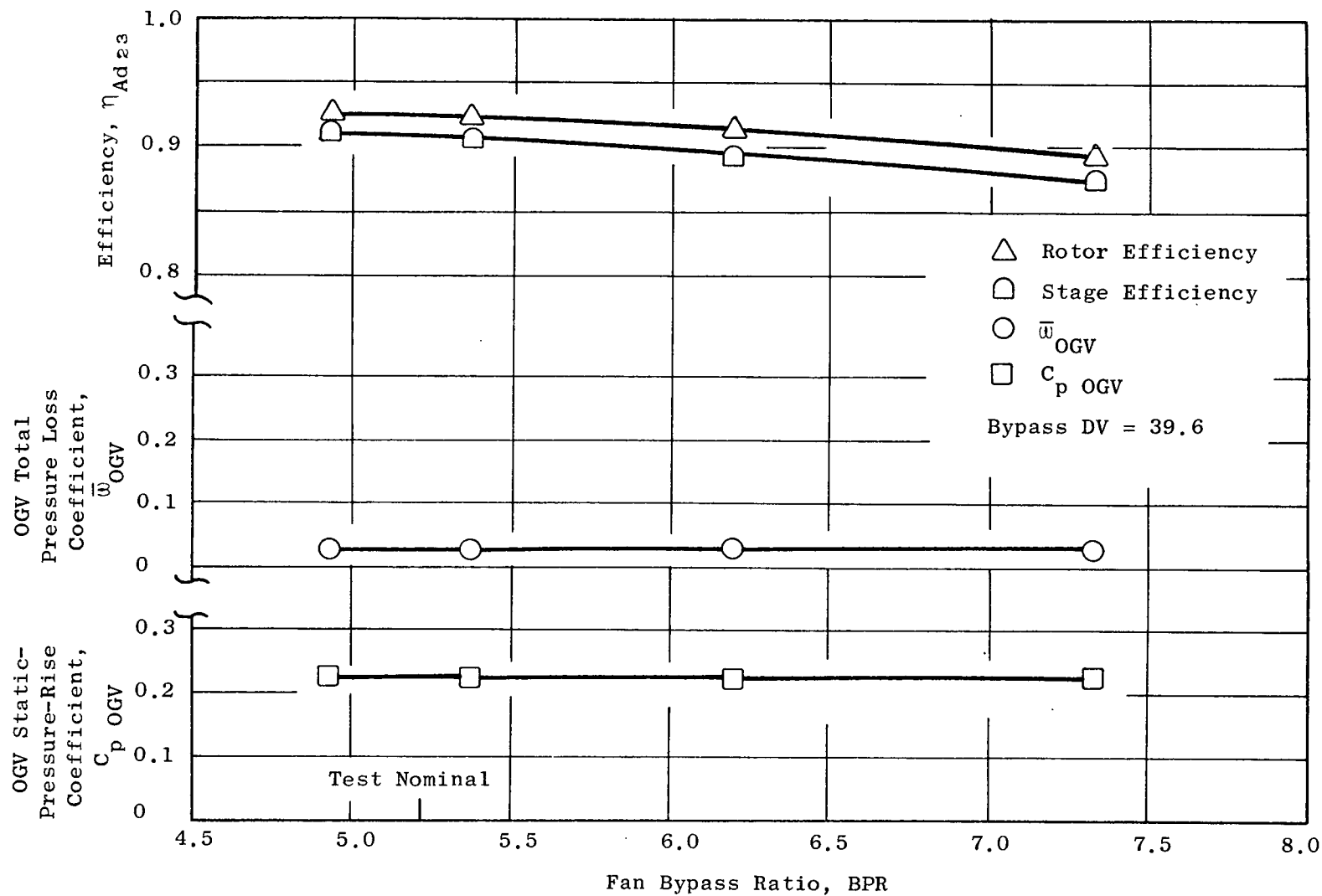


Figure 22. Variation of Element Properties with Bypass Ratio, Design Stream Function = 0.422.

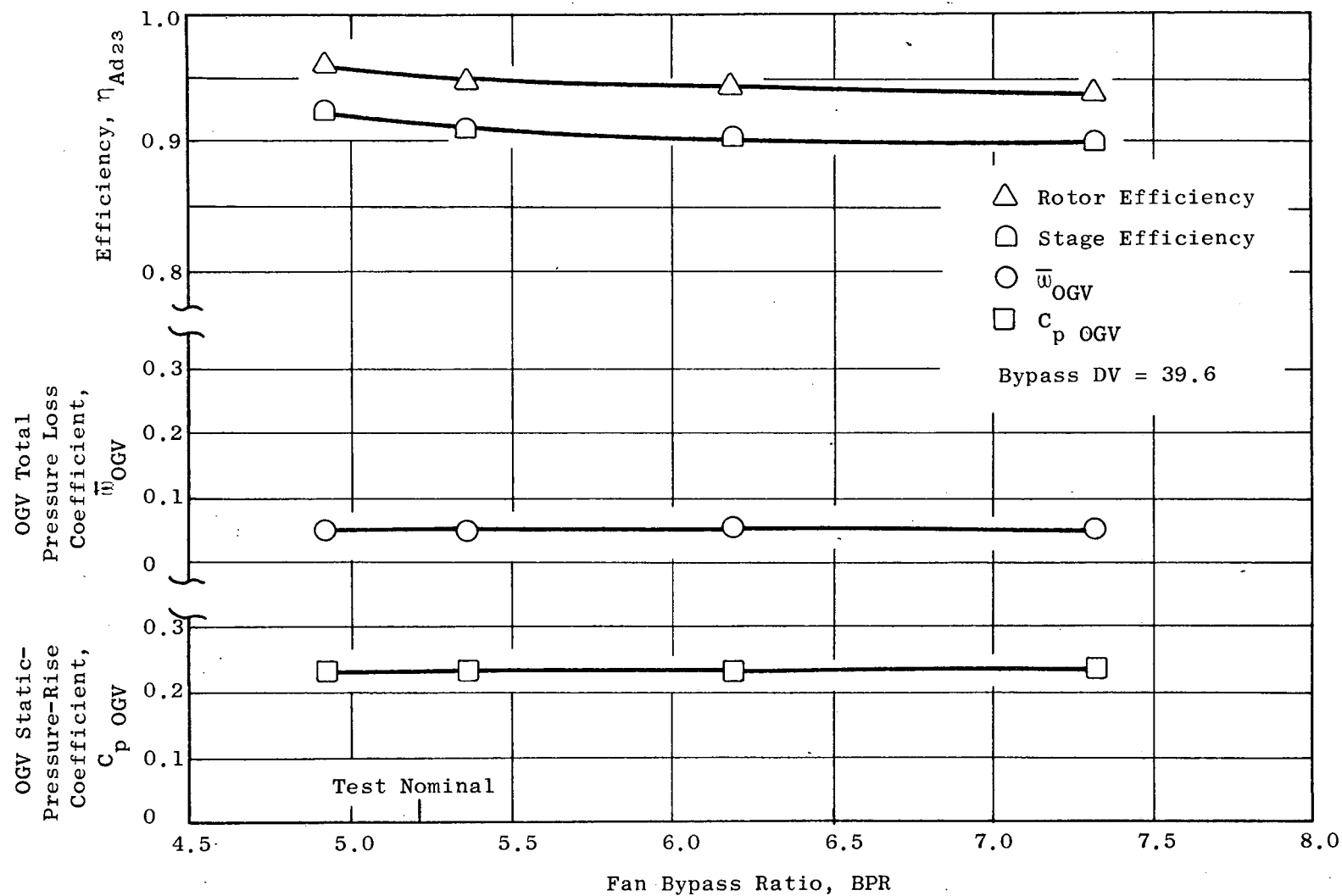


Figure 23. Variation of Element Properties with Bypass Ratio, Design Stream Function = 0.543.

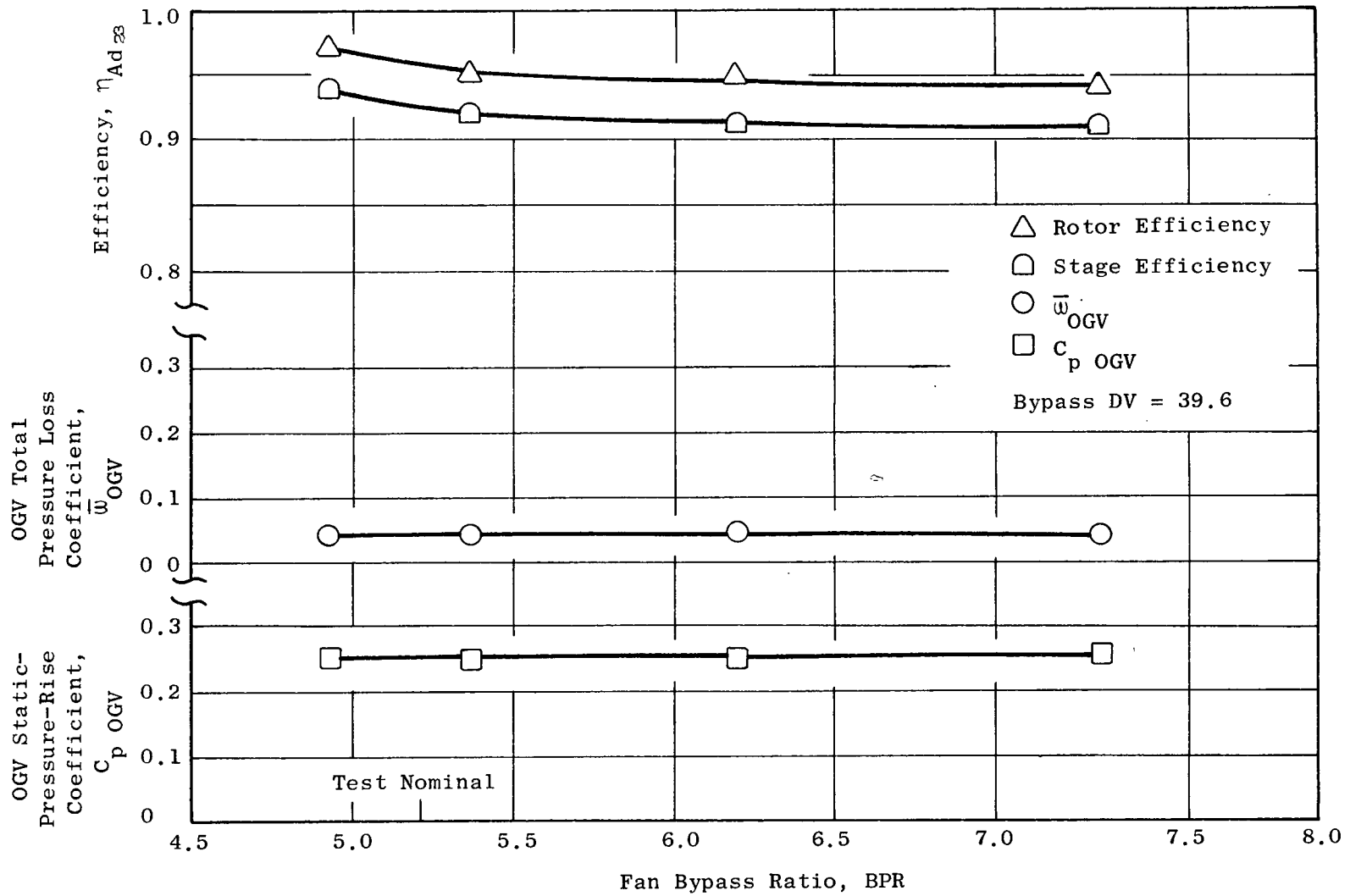


Figure 24. Variation of Element Properties with Bypass Ratio, Design Stream Function = 0.664.

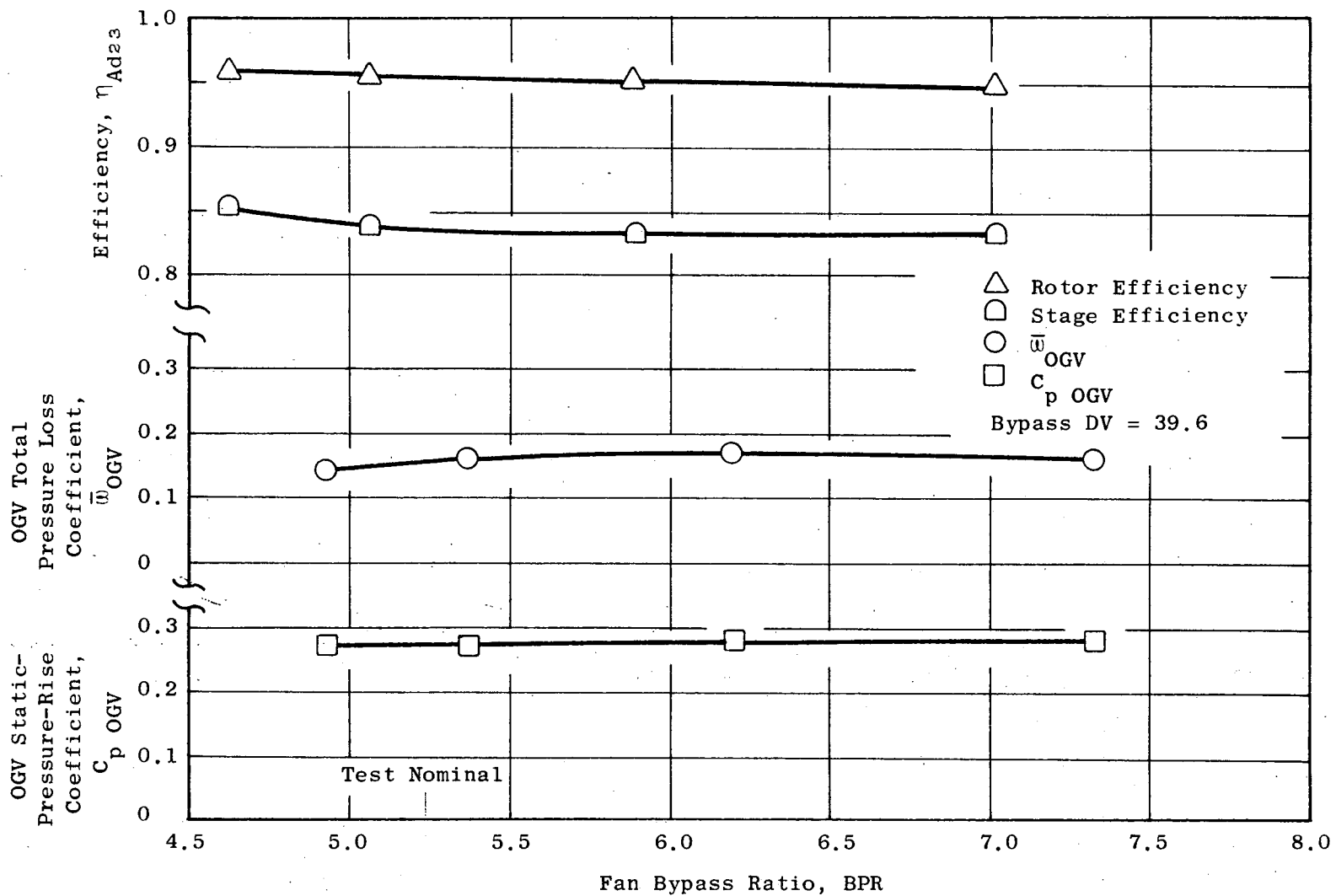


Figure 25. Variation of Element Properties with Bypass Ratio, Design Stream Function = 0.785.

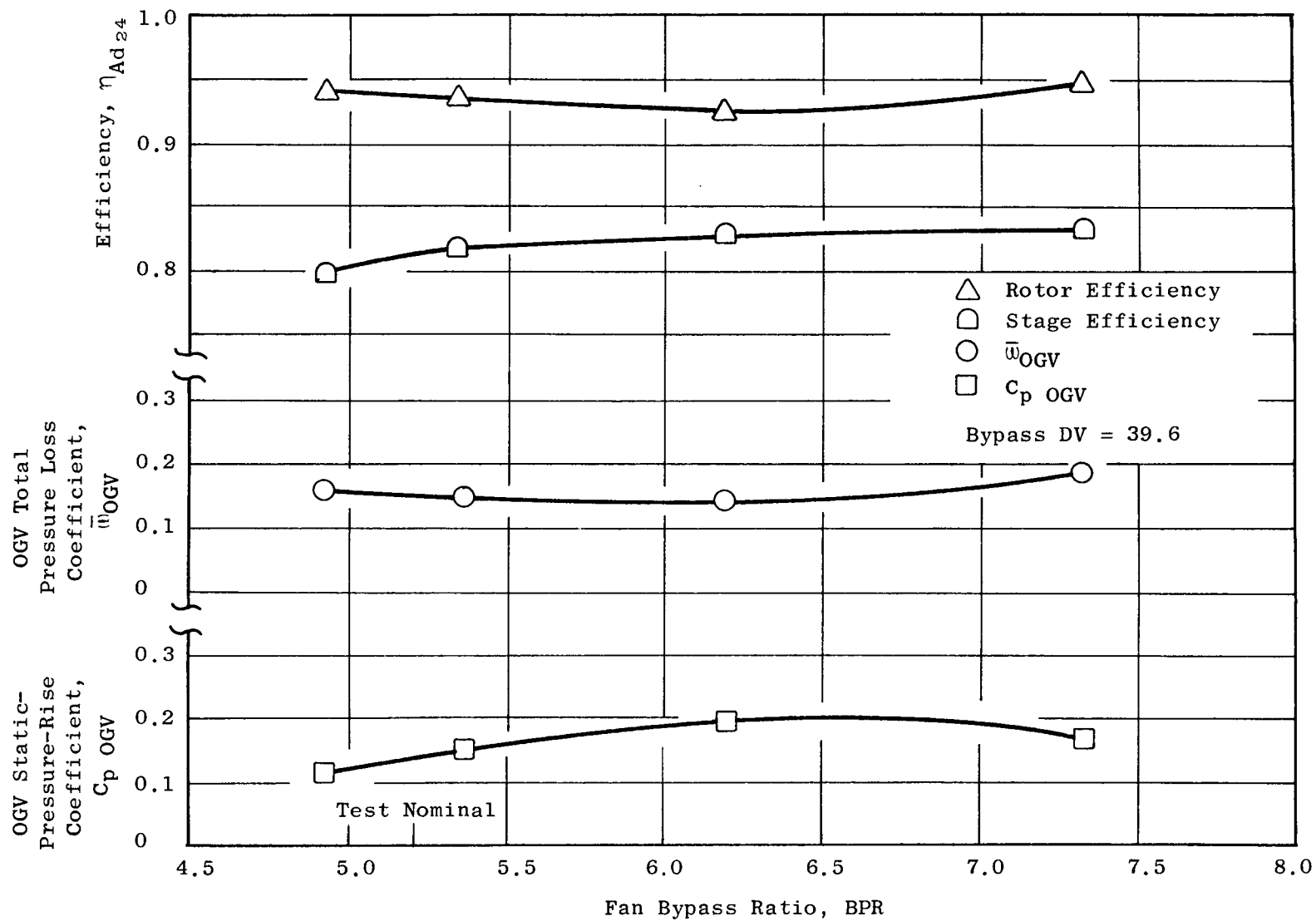


Figure 26. Variation of Element Properties with Bypass Ratio, Design Stream Function = 0.861.

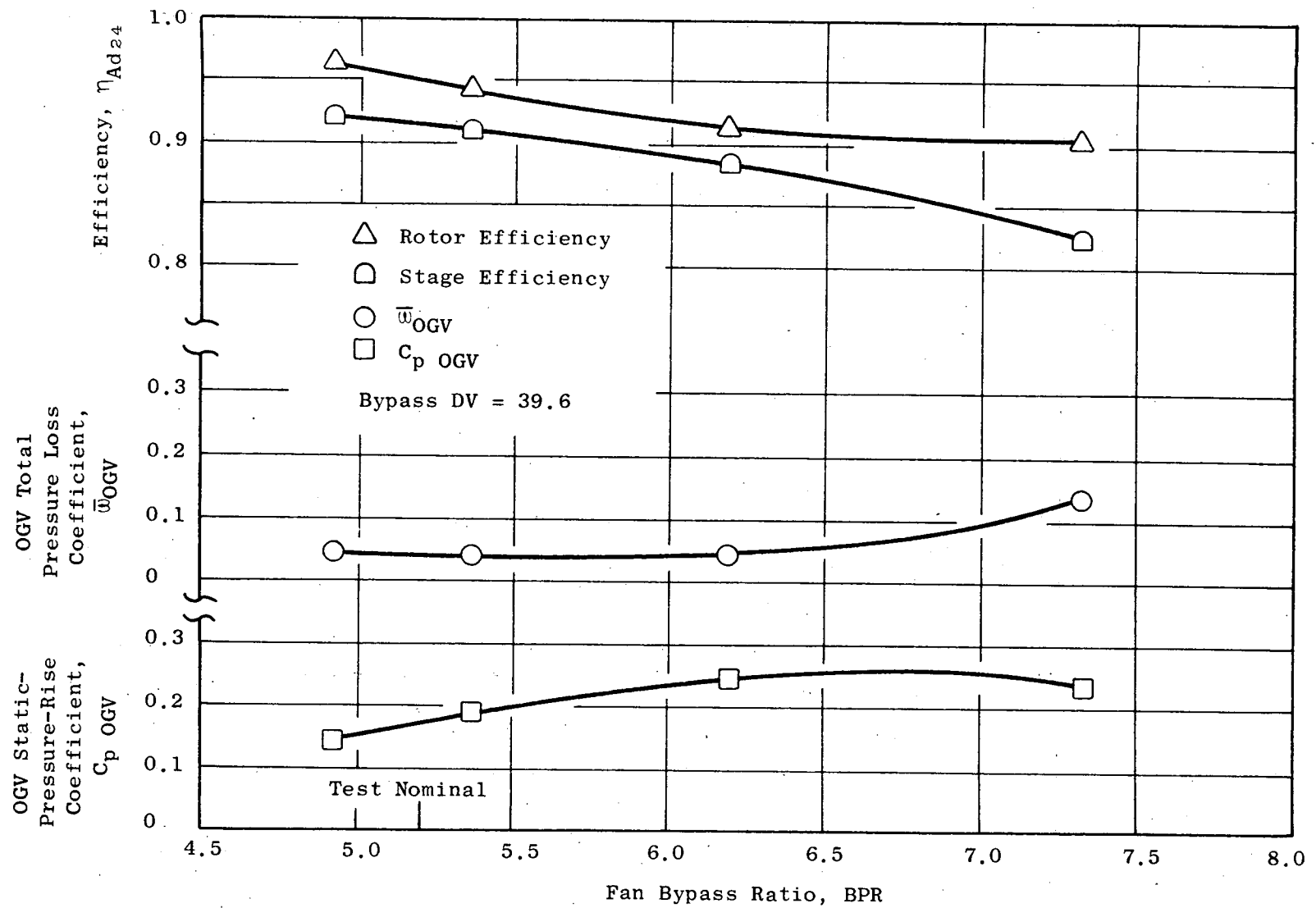


Figure 27. Variation of Element Properties with Bypass Ratio, Design Stream Function = 0.892.

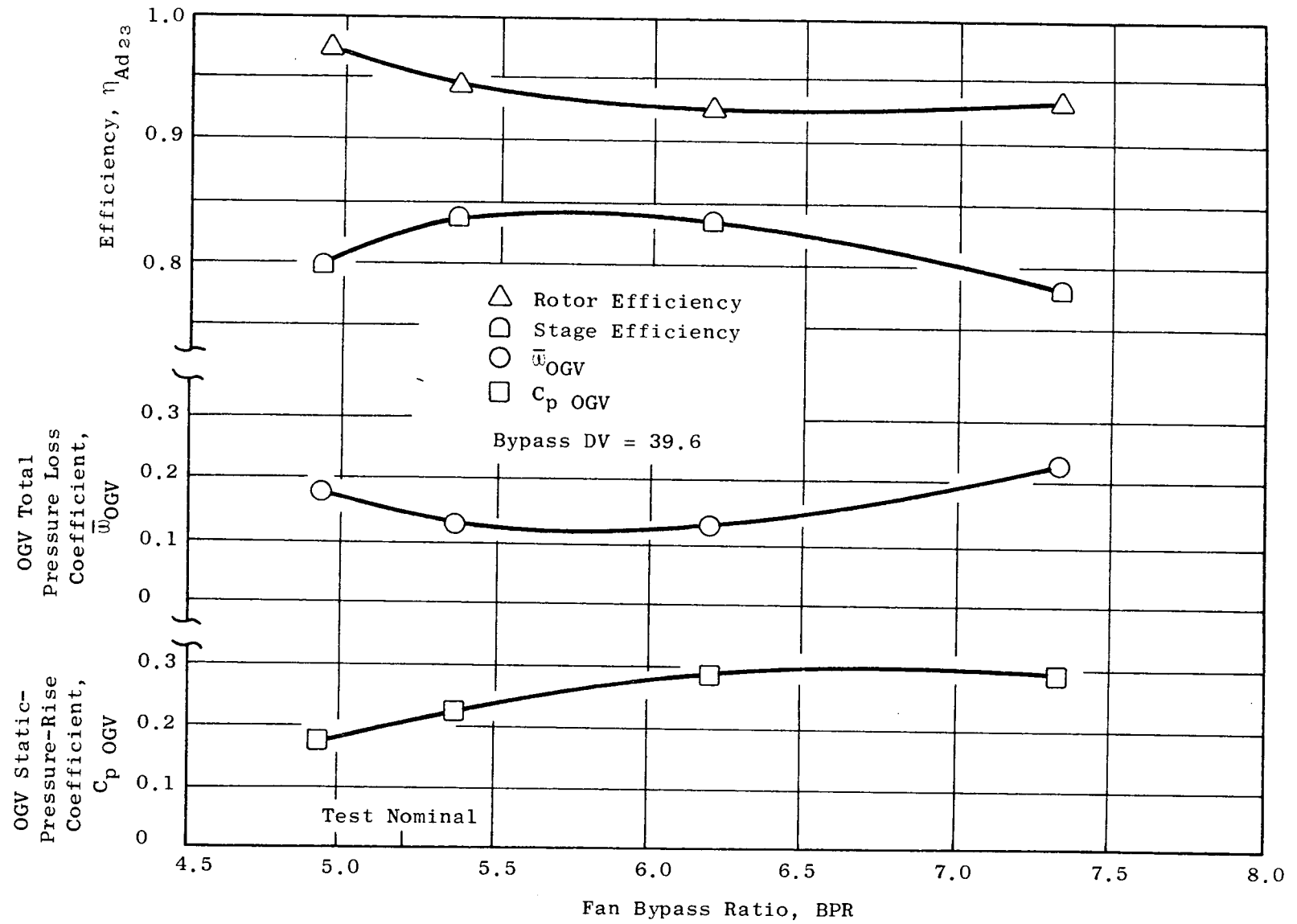


Figure 28. Variation of Element Properties with Bypass Ratio, Design Stream Function = 0.923.

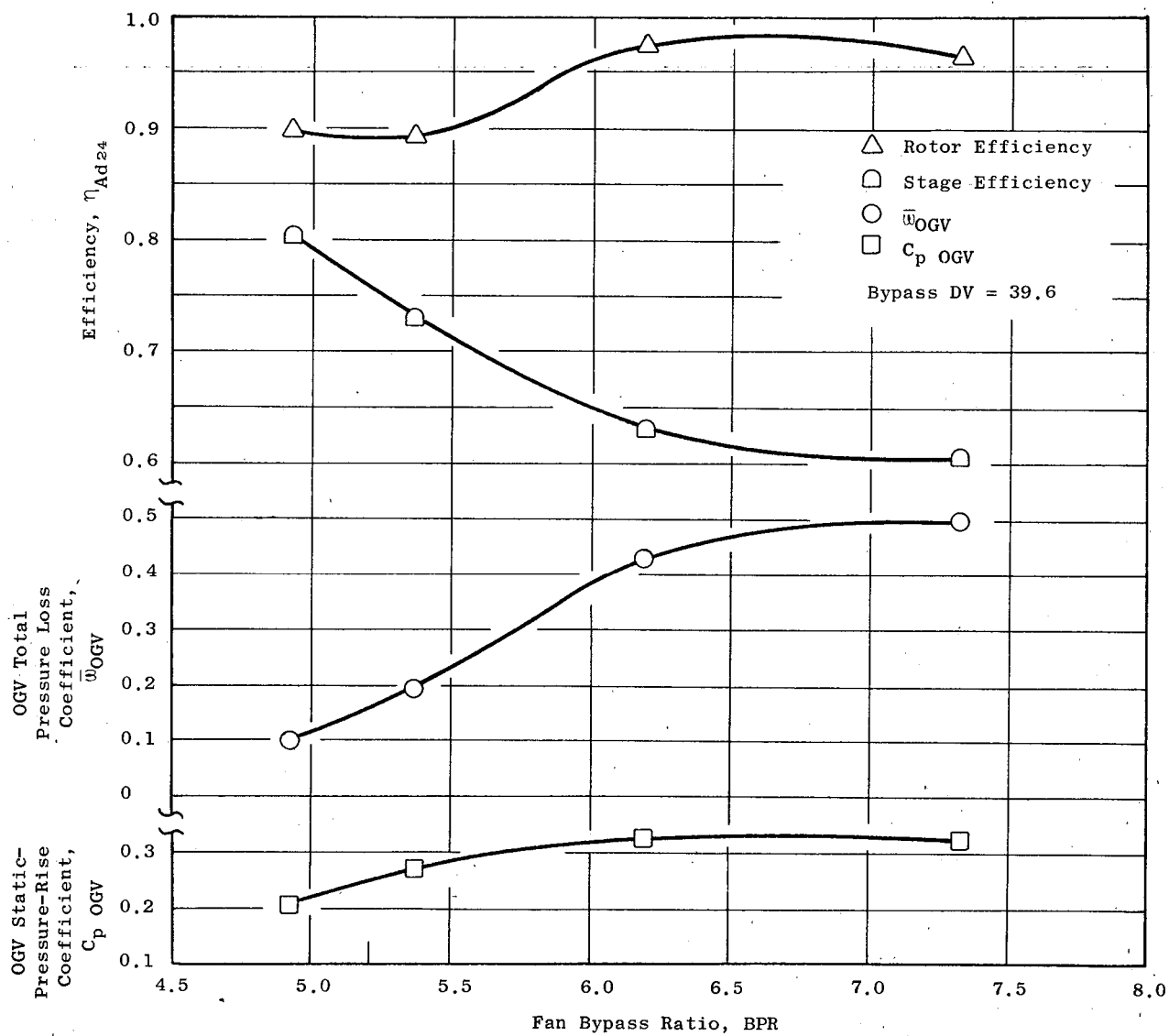


Figure 29. Variation of Element Properties with Bypass Ratio, Design Stream Function = 0.954.

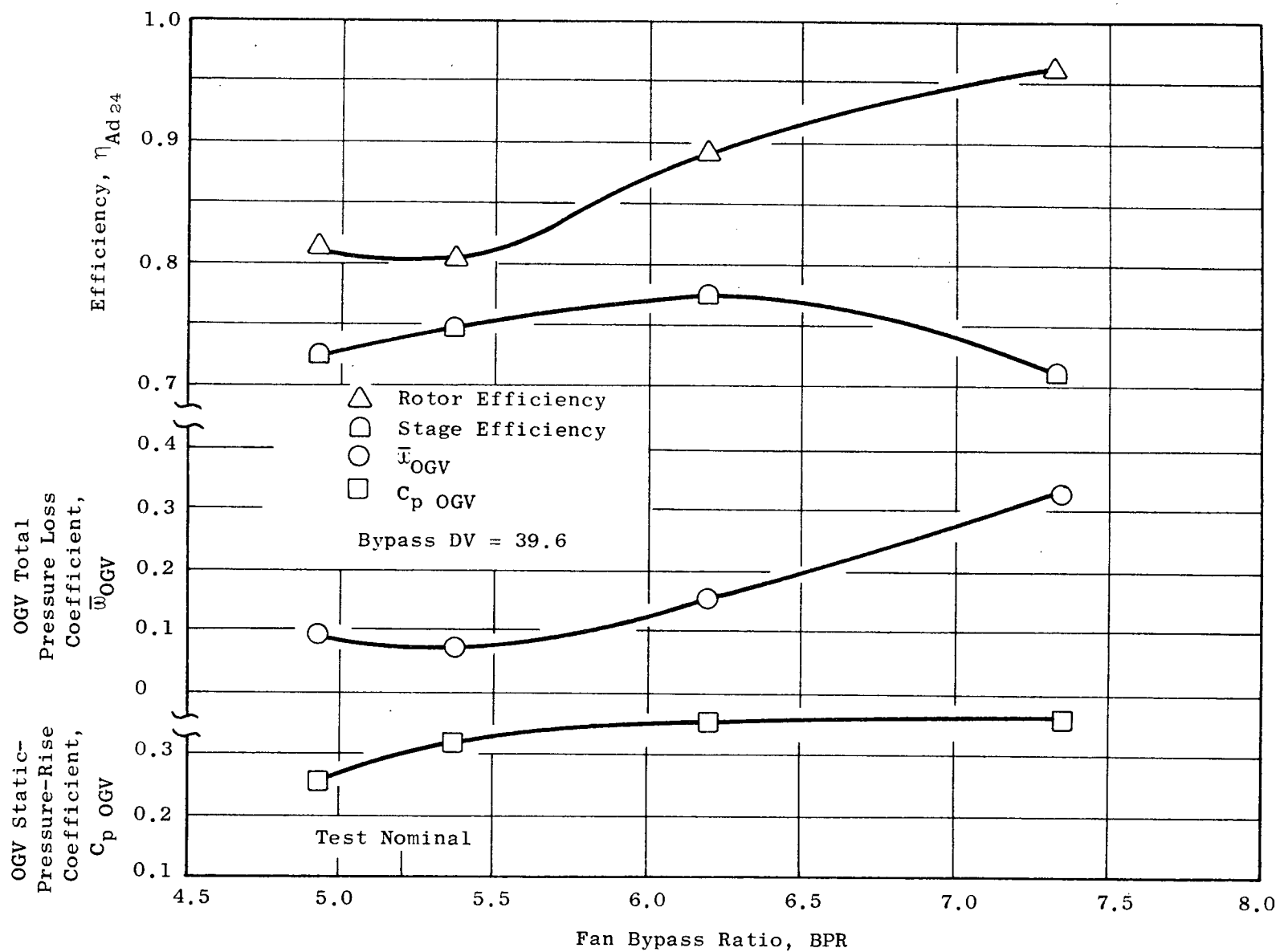


Figure 30. Variation of Element Properties with Bypass Ratio, Design Stream Function = 0.985.

4. Fan Bypass OGV Schedule

A brief investigation to determine the optimum setting of the bypass OGV was conducted at 100% corrected speed for two fan bypass operating lines. The results are presented in Figure 31 which shows the series of test points recorded for this investigation on a bypass performance map. The two operating lines are approximately equidistance on the high and low sides of the nominal operating line. The high operating point data indicate performance improves with OGV closure. However, the low operating point data indicate a performance deficit with OGV closure. It was judged that the nominal vane setting was near optimum at the design operating line.

5. Fan Core OGV Schedule

Early results from the build 1 configuration showed low efficiency in the fan core region. Analysis of the build 1 data indicated that the rotor core efficiency was down from expectations and also that the fan core OGV losses were markedly higher than expectations. Modification to the rotor hub geometry was difficult and time consuming and the probability of success was uncertain. However, the flexibility to restagger both the forward and aft portions of the OGV in 2° increments plus the ability to adjust the relative circumferential positioning of the two elements was incorporated into the vehicle mechanical design. Analysis of the build 1 results indicated that the design setting of the OGV forward element matched the test inlet vector diagram. It was concluded, therefore, that a closure of the aft element, to lower the aerodynamic loading, would result in a significant improvement. A 6° closure was selected on the basis of providing the maximum loading reduction consistent with not raising the discharge swirl to a magnitude that would cause separation from the frame strut leading edge. The rotational axis of the aft element is approximately at center chord, hence the closure of this element opens the circumferential slot between the fore element trailing edge and aft element leading edge. Since the initial slot geometry apparently did not fulfill its intended objective and since the slot geometry resulting from the 6° closure was aerodynamically reasonable at a significantly increased slot flow rate, no circumferential adjustment was made.

The OGV aft element closure was made between build 1 and 1A tests. Since the inlet performance instrumentation was different between these two builds (the inlet distortion rakes were used on build 1A), it is believed that a better absolute comparison can be made by using build 2 (identical instrumentation to build 1), which was the same as build 1A except for the substitution of titanium rotor blades.

The comparison of the fan core performance between builds 1 and 2 is presented in Figure 32 in terms of the fan core map. The data at 90 and 100% corrected speed are shown since they are representative and are of greatest interest. At 100% corrected speed, the pressure ratio is observed to increase by about 0.02 counts with a corresponding efficiency improvement of about 3 points. The efficiency improvement at 90% corrected speed is about 3 points with a significant improvement in pressure ratio.

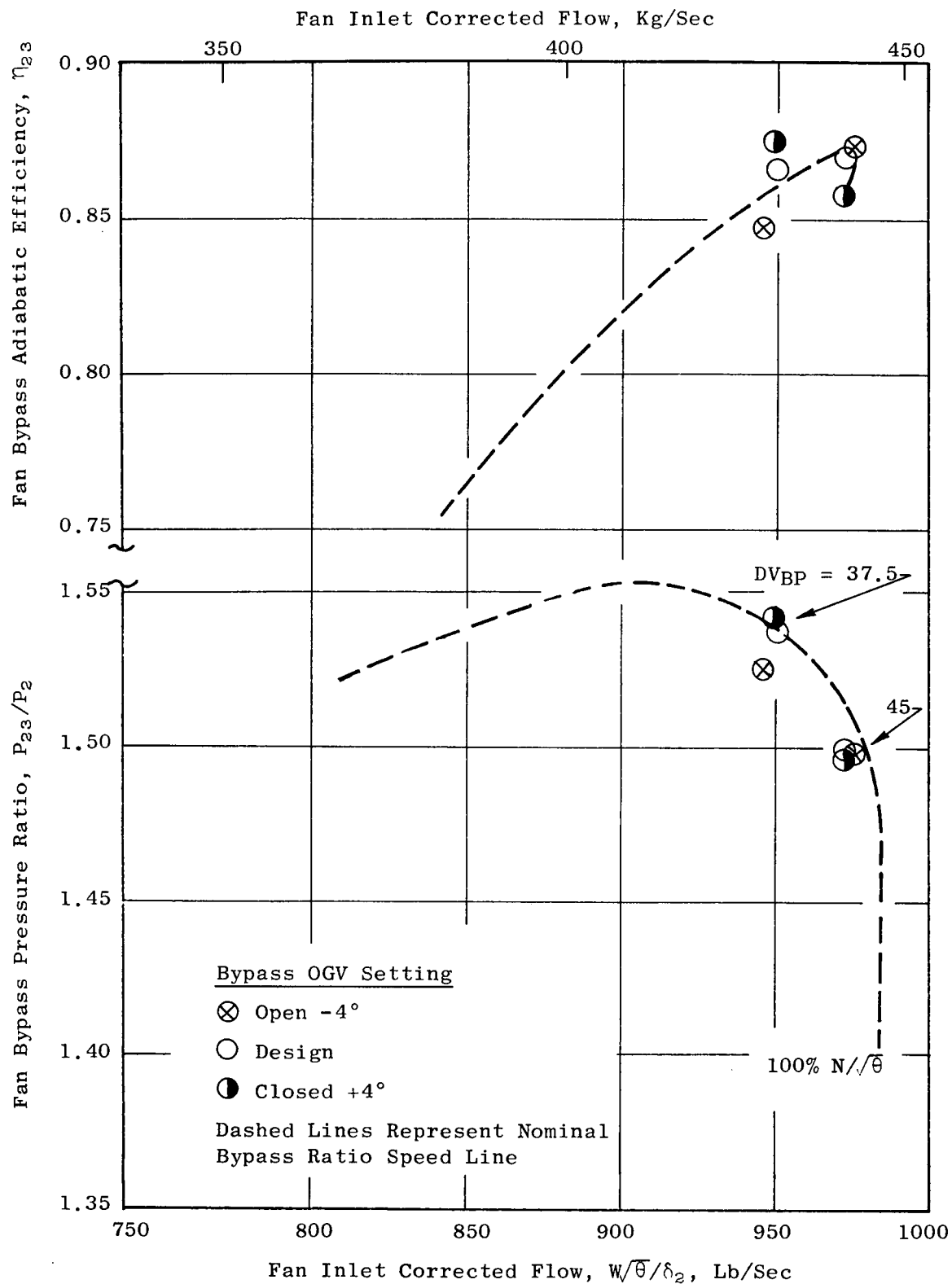


Figure 31. Effects of OGV Setting Angle on Bypass Performance.

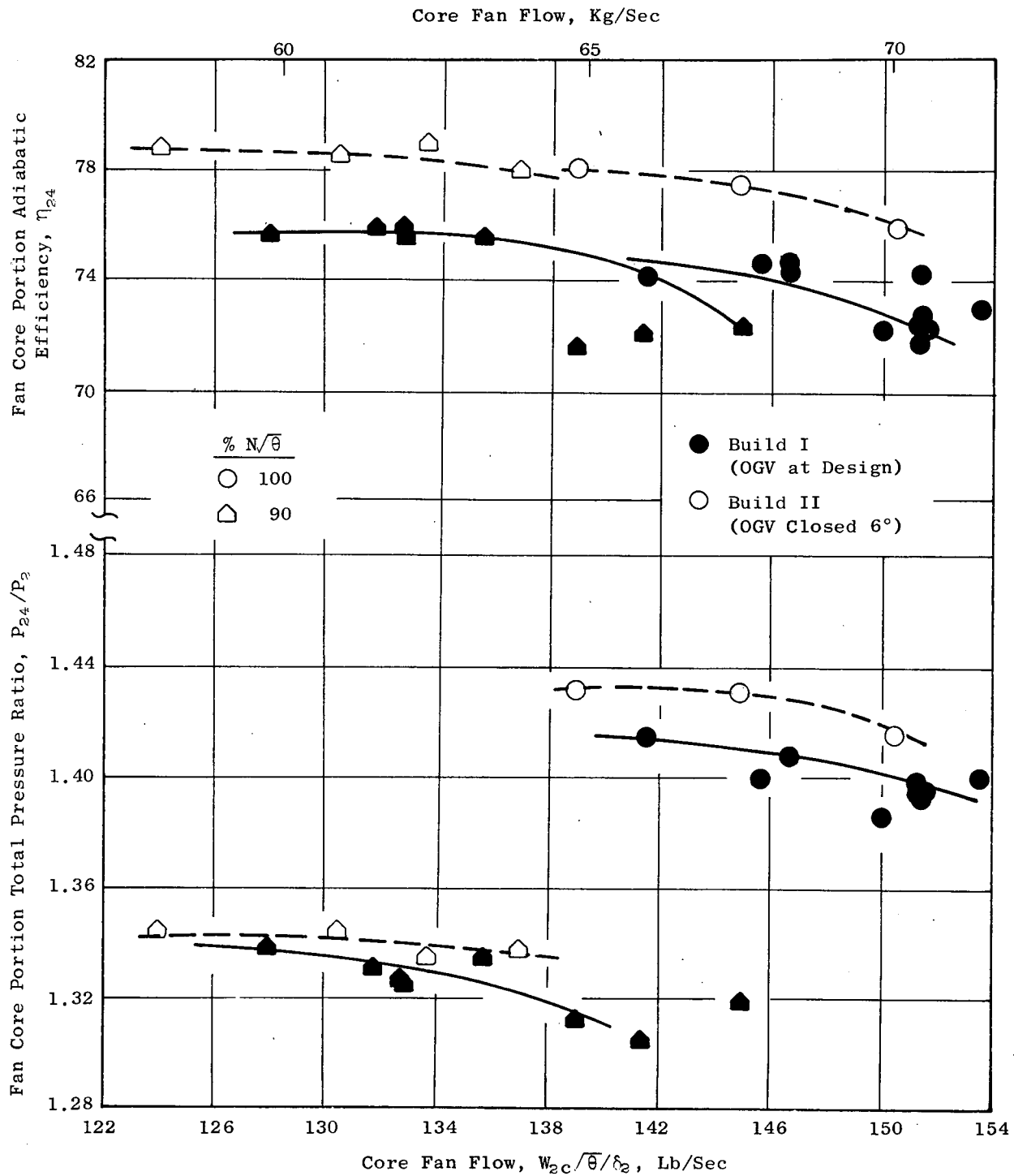


Figure 32. Effect of OGV Closure on Fan Core Performance.

6. Traverse Data

Traverse data at 100% corrected speed, at an operating point slightly above the design operating line, are presented in Figures 33 through 41. These data were recorded on build 1. These data are presumed applicable to either build since the aerodynamic shape of the build 2 blades was the same as the build 1 blades and the overall performance of the two builds was virtually identical to the OGV leading edge. Traverse data was taken at four axial planes: rotor inlet, rotor discharge, bypass OGV inlet, and fan core OGV inlet. A major purpose for the traverses at two axial locations behind the rotor was the determination of any detrimental effects on the flow caused by the large axial gap between blade rows.

In the bypass, Figures 33 through 37, no obvious serious defects are observed. Careful examination of the outside diameter portion of the total-pressure traverse, Figure 33, indicates a relatively larger wall boundary layer velocity defect at OGV inlet than at rotor exit. This is evidenced by the larger difference between the local tip value of total pressure and the adjacent free-stream (the increase in total pressure between the two probe locations is, of course, impossible). The increased velocity defect is a contribution to the larger design OGV total-pressure-loss coefficient in the tip region. For the fan core, Figures 38 through 41 show the rotor total pressure and efficiency defects which were discussed previously. A second item is the difference between the two measurements of absolute air angle, particularly in light of the poor OGV performance. Two factors tended to discredit the lower angle measurement: (1) a computation of blockage and work input using wall static pressure, measured angle, and continuity resulted in poor agreement with past blockage experience and did not check the measured temperature rise, and (2) the vane throat area was not sufficient to pass the measured flow at such a low inlet angle. Accordingly, the level of the lower angle reading was treated as incorrect. From a choke and optimum incidence angle standpoint on the inner OGV, the deviation of the assumed correct measured flow angle from the design intent is significant. However, as previously indicated from Figures 15 through 19, there were no apparent signs of choking or of an off-optimum incidence angle problem. Accordingly, when the change to the inner OGV setting was made, the apparent nonoptimum incidence angle was ignored.

C. DISTORTED FLOW PERFORMANCE

The build 2 Fan B was tested with a tip radial, hub radial, and one-per-rev circumferential inlet distortion. The distortion was generated by screens mounted on a support structure which was located approximately 0.6 fan diameters in front of the rotor. The tip and hub radial distortion generating screens covered the outer and inner 40% of the annulus, respectively. The one-per-rev distortion extended over the full annulus height and was 180° in circumferential extent. The distortion levels generated by the screens are shown in Figure 42. Plots of the actual distortion patterns for the most

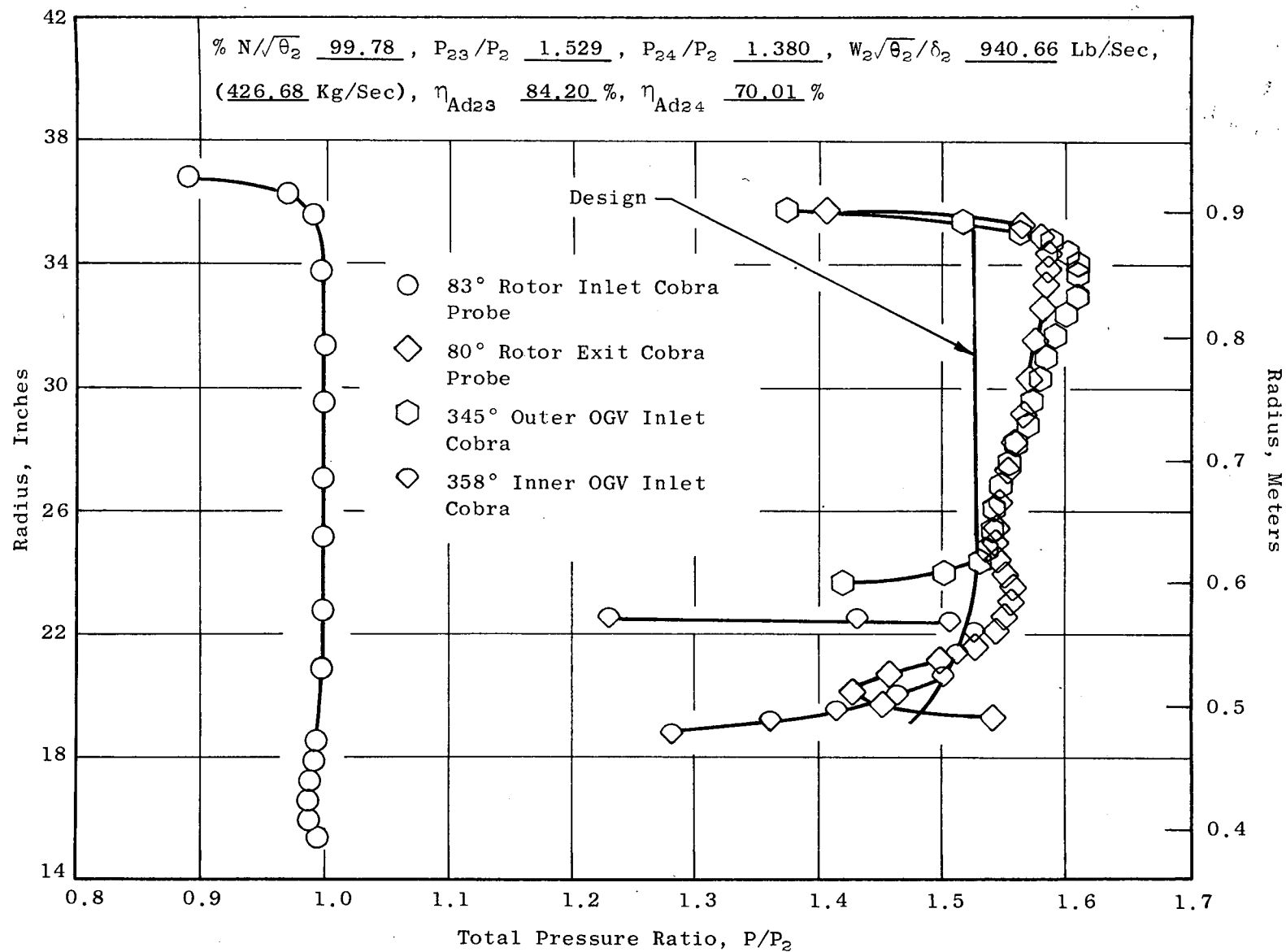


Figure 33. Traverse Radial Profiles, Radius Vs. Total Pressure Ratio (Bypass).

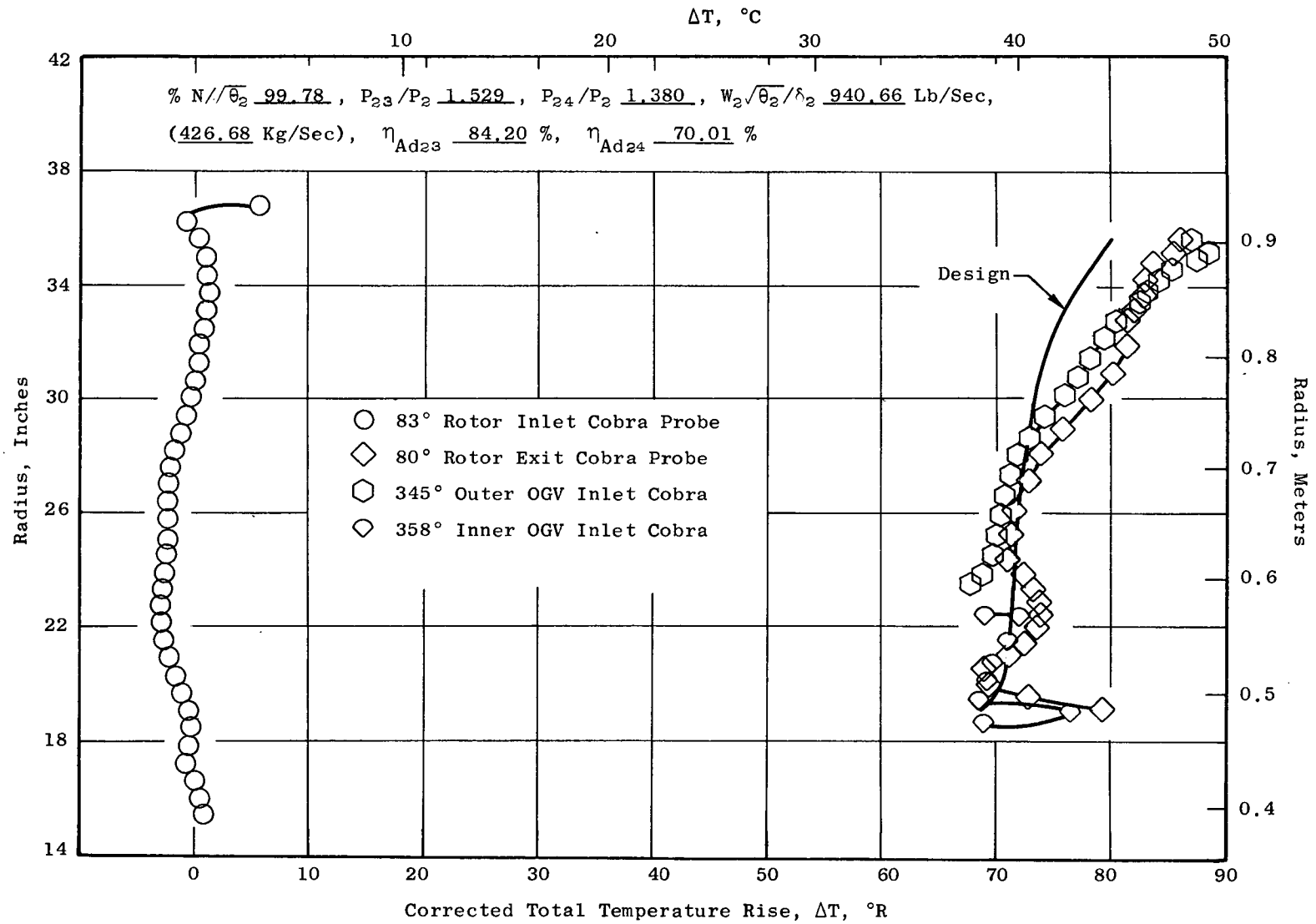


Figure 34. Traverse Radial Profiles, Radius Vs. Corrected Total Temperature Rise (Bypass).

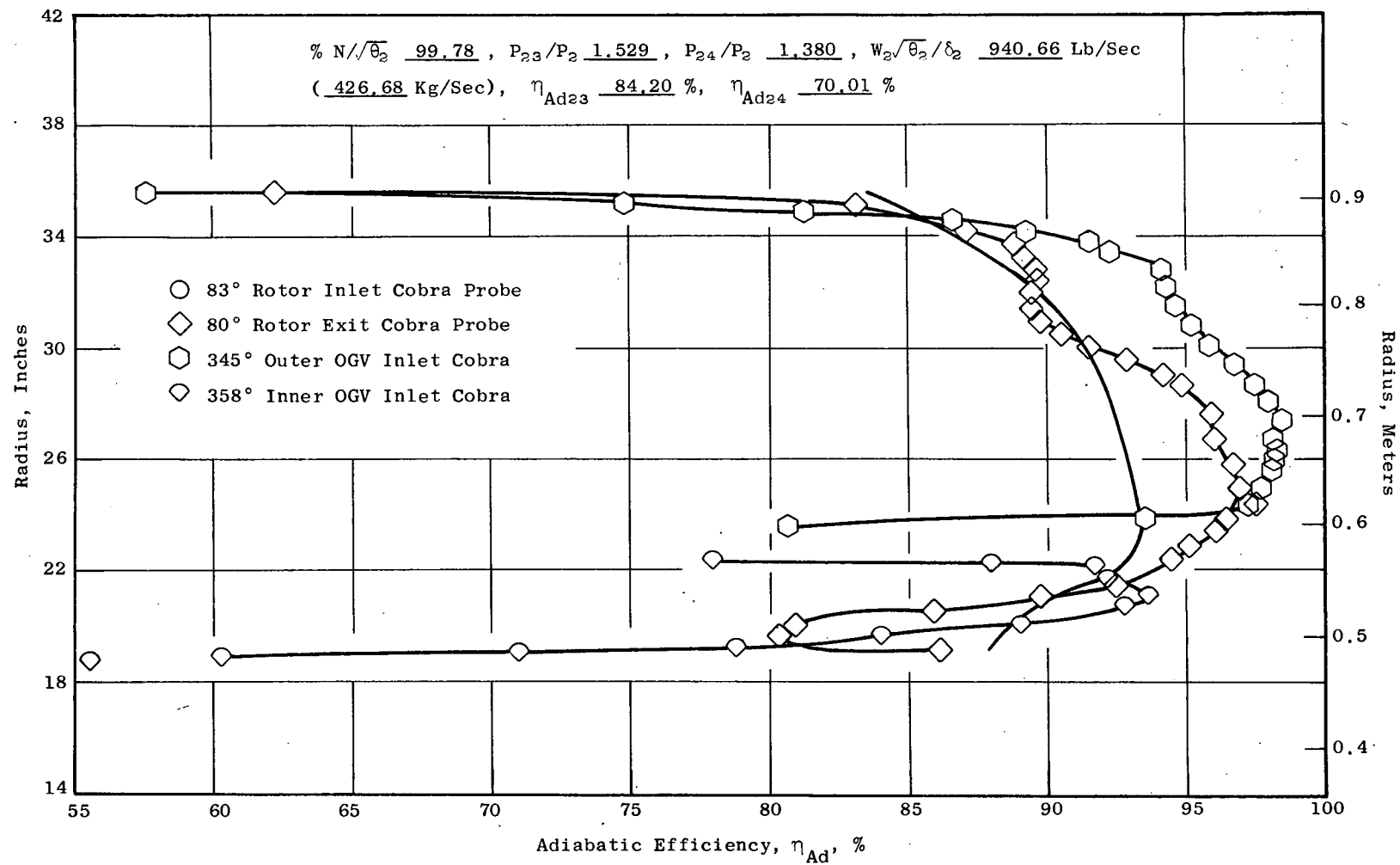


Figure 35. Traverse Radial Profiles, Radius Vs. Adiabatic Efficiency (Bypass).

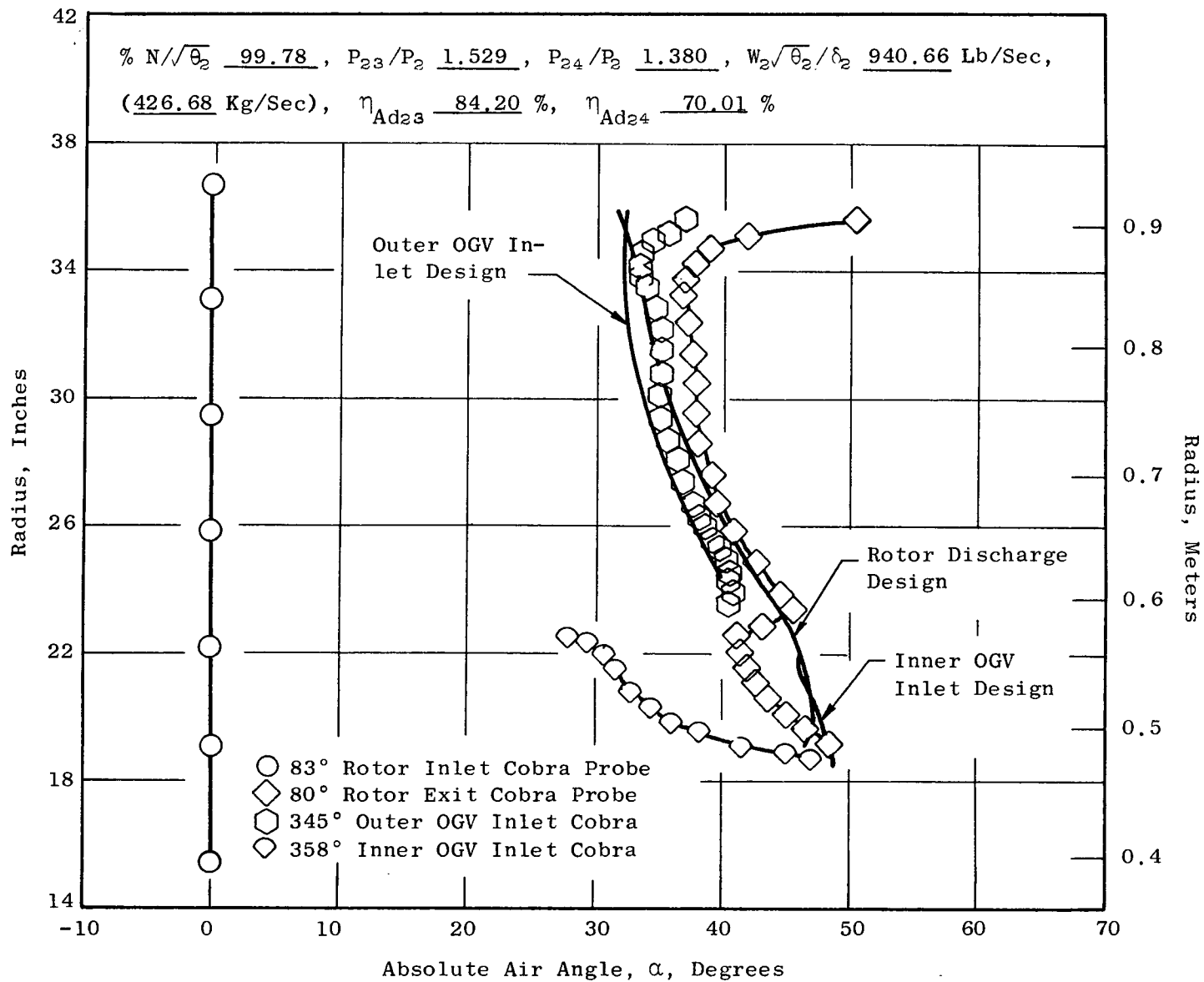


Figure 36. Traverse Radial Profiles, Radius Vs. Absolute Air Angle (Bypass).

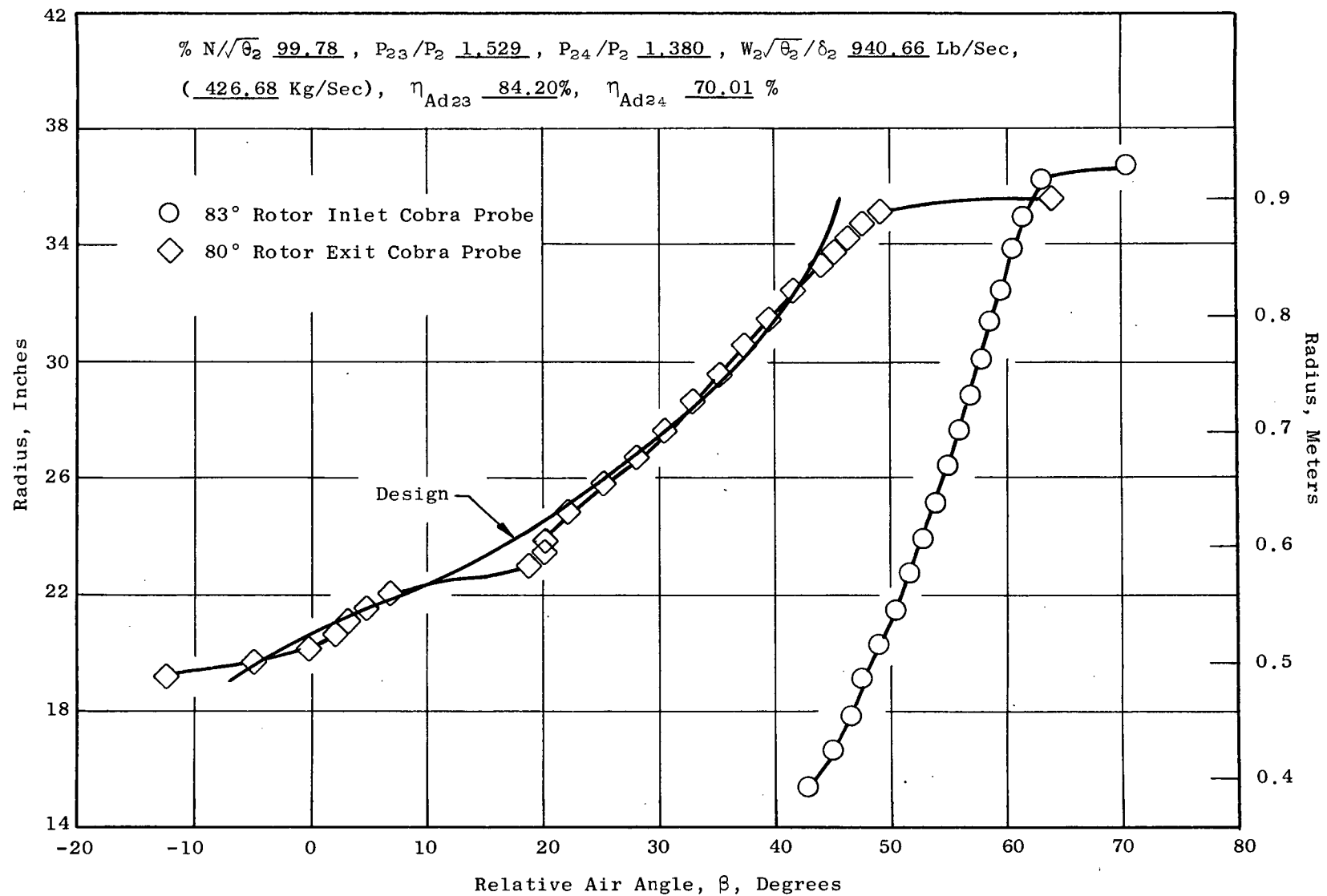


Figure 37. Traverse Radial Profiles, Radius Vs. Relative Air Angle (Bypass).

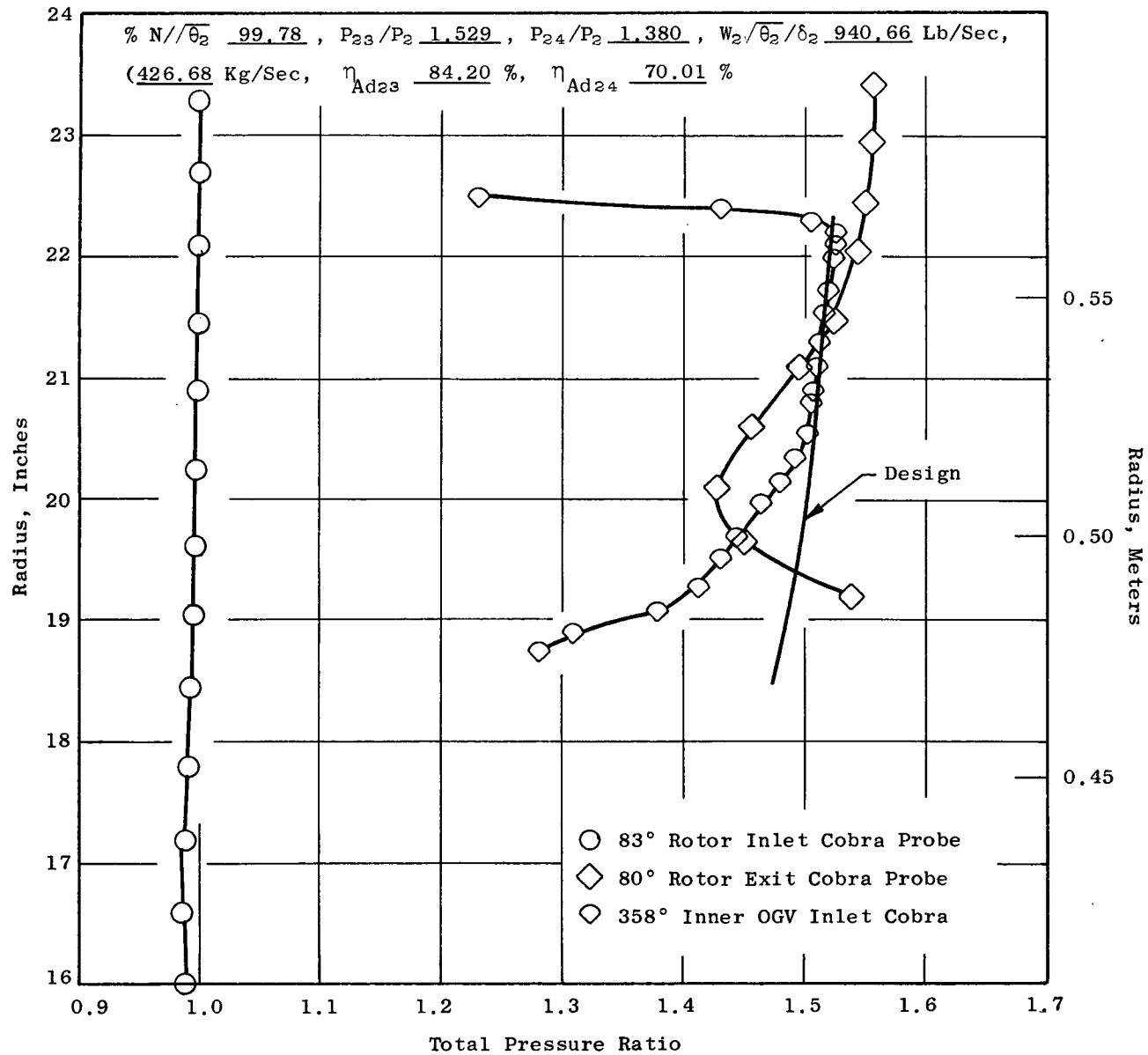


Figure 38. Traverse Radial Profiles, Radius Vs. Total Pressure Ratio (Core).

$\% N/\delta_2$ 99.78 , P_{23}/P_2 1.529 , P_{24}/P_2 1.380 , $W_2\sqrt{\theta_2}/\delta_2$ 940.66 Lb/Sec,
 (426.68 Kg/Sec), η_{Ad23} 84.20 %, η_{Ad24} 70.01 %
 $\Delta T, ^\circ C$

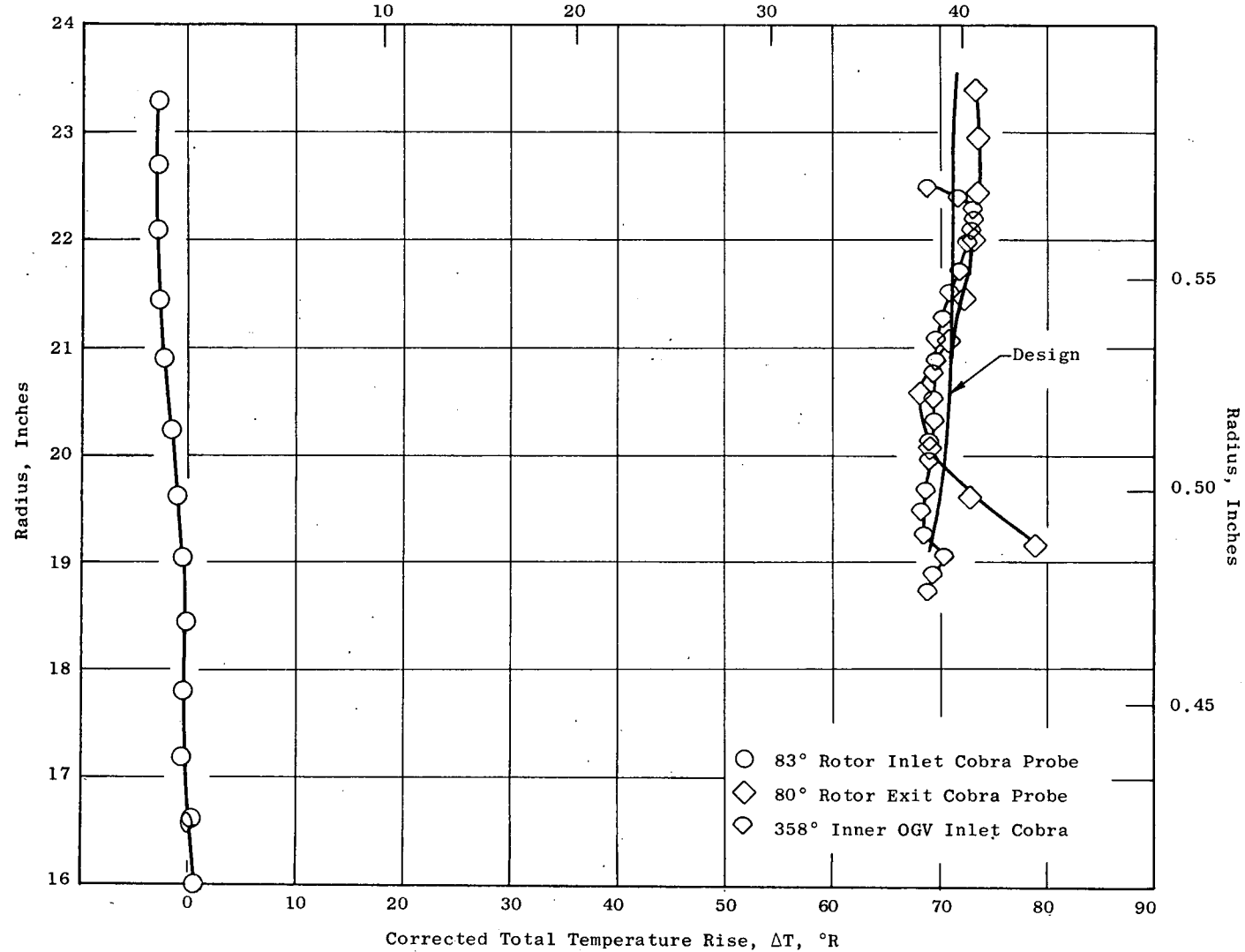


Figure 39. Traverse Radial Profiles, Radius Vs. Corrected Total Temperature Rise (Core).

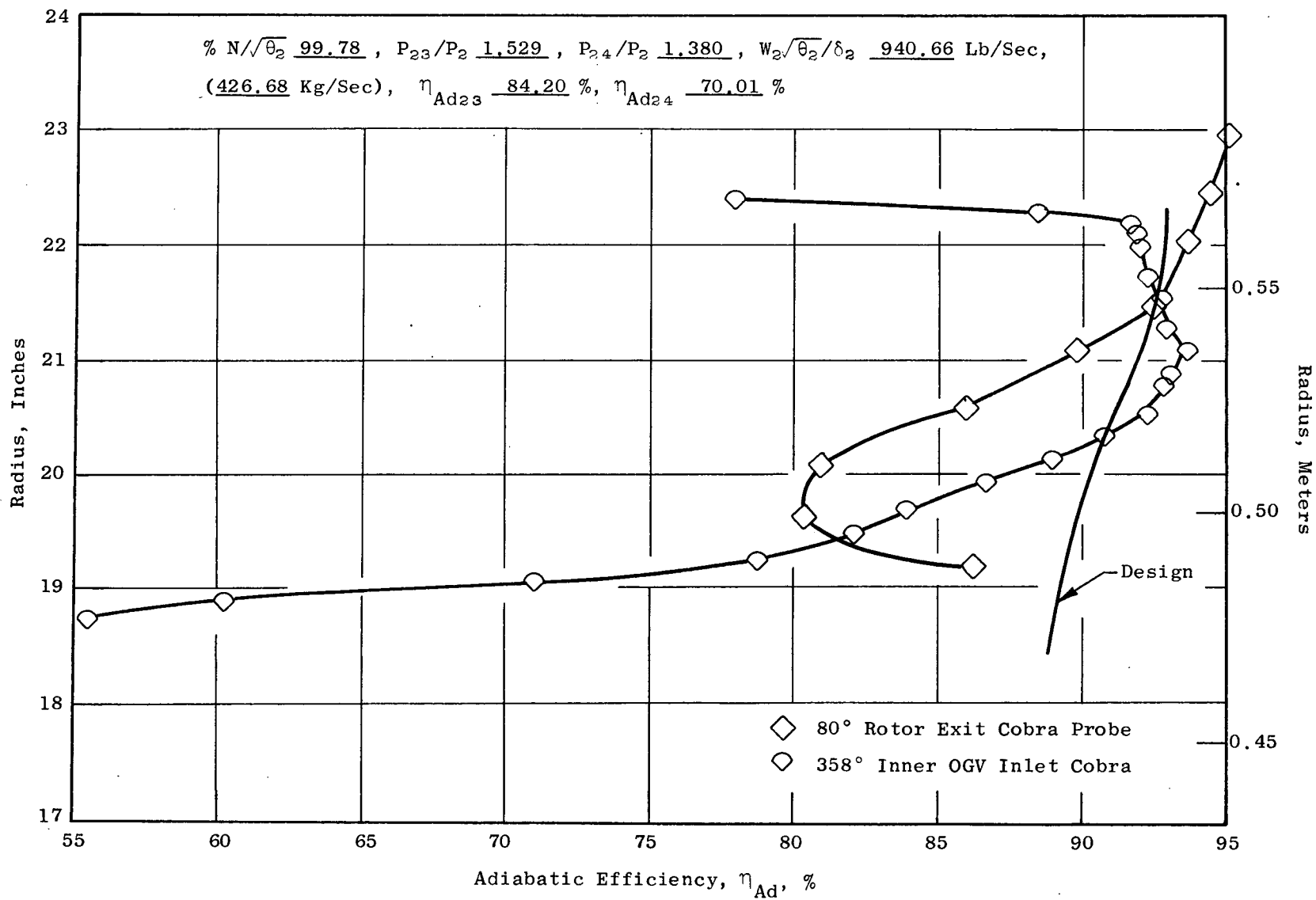


Figure 40. Traverse Radial Profiles, Radius Vs. Adiabatic Efficiency (Core).

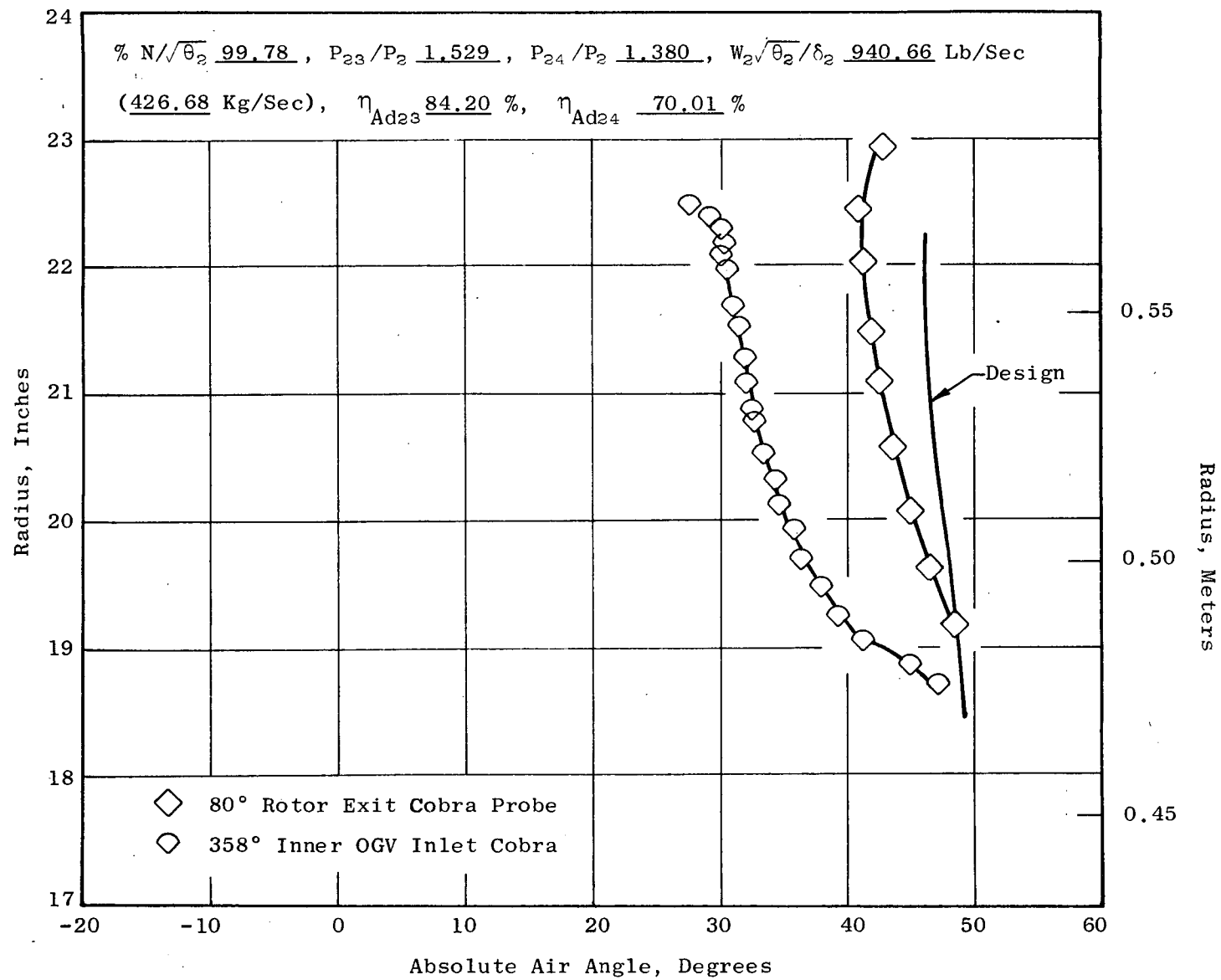


Figure 41. Traverse Radial Profiles, Radius Vs. Absoulte Air Angle (Core).

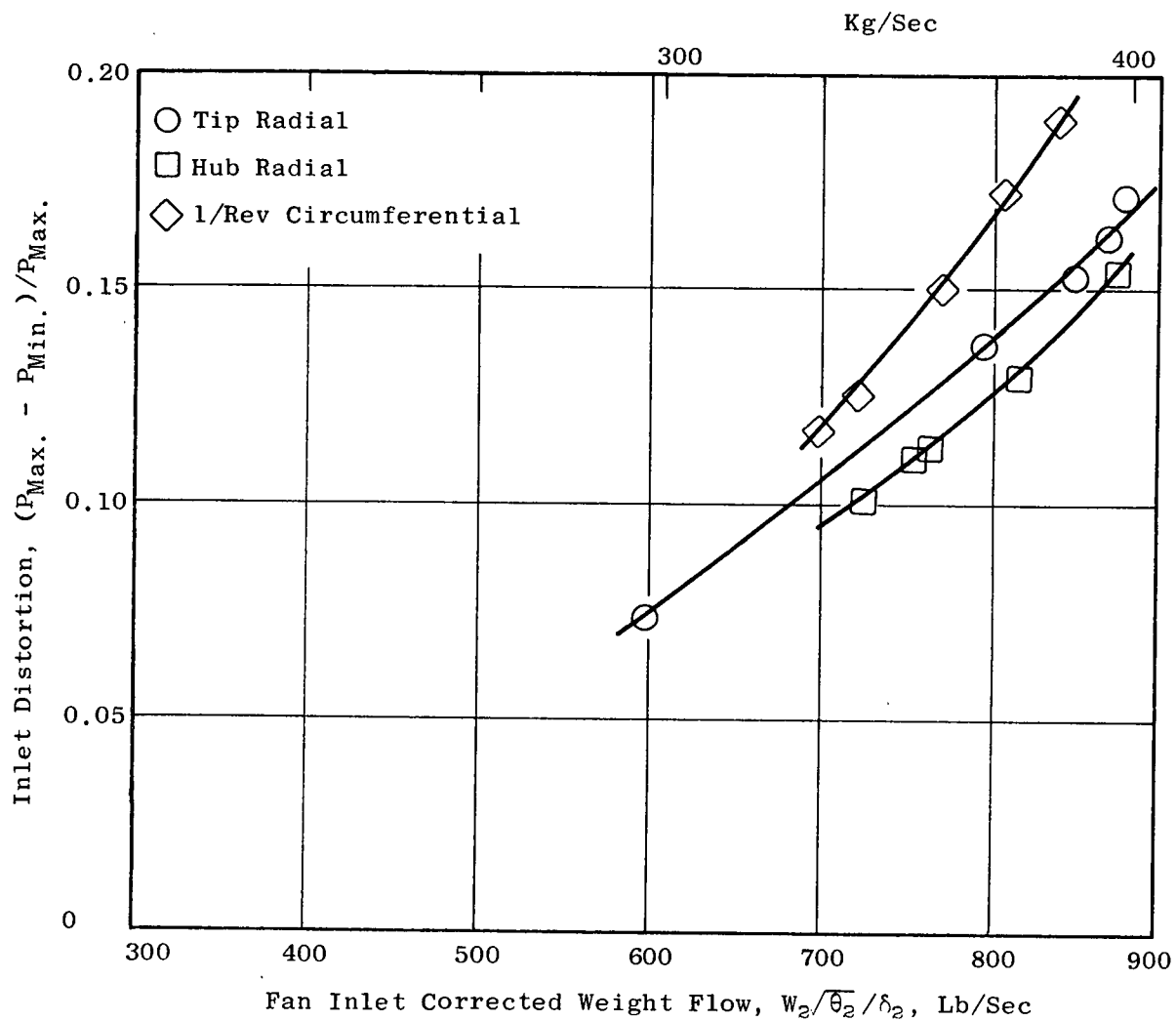


Figure 42. Inlet Flow Distortion Level.

closed throttle condition at 90% speed are shown in Figures 43 through 45. Prior to the distortion testing, a brief run was conducted with the screen support structure and backup screen installed to determine any changes to the overall performance that might be induced by this structure.

The overall performance maps for the distorted flow testing are shown in Figures 46 and 47. Also shown in the background is the clean inlet performance to facilitate comparison. The calibration run with the support structure installed shows reasonable repeatability of the speed line data with the clean inlet; the most significant aerodynamic effect expected was inaccuracy due to data sampling problems. The seeming increase in operating margin at 90% speed of the calibration run above the clean inlet run may be a result of some interaction between the wakes from the distortion screen support structure and the rotor blading, of inaccuracies in the methods of locating the stall line, of screen support wakes on inlet pressure measurements, or a combination of these with other unidentified effects. The hub radial distortion resulted in no significant effect on the fans operating margin using the calibration run as the base for comparison. The one-per-rev distortion resulted in a moderate decrease in the fan operating margin. The tip radial distortion resulted in a far greater reduction in fan operating margin than either of the other two patterns with the greatest reduction in operating margin occurring at 80% speed. The large fan operating margin reduction observed with tip radial inlet distortion is consistent with test experience on other single-stage fans. In the distortion data reduction, no attempt was made to segregate the inlet pressures to account for a lower than average pressure entering the bypass portions with the tip radial distortion and a higher than average pressure entering the bypass portion with the hub radial distortion.

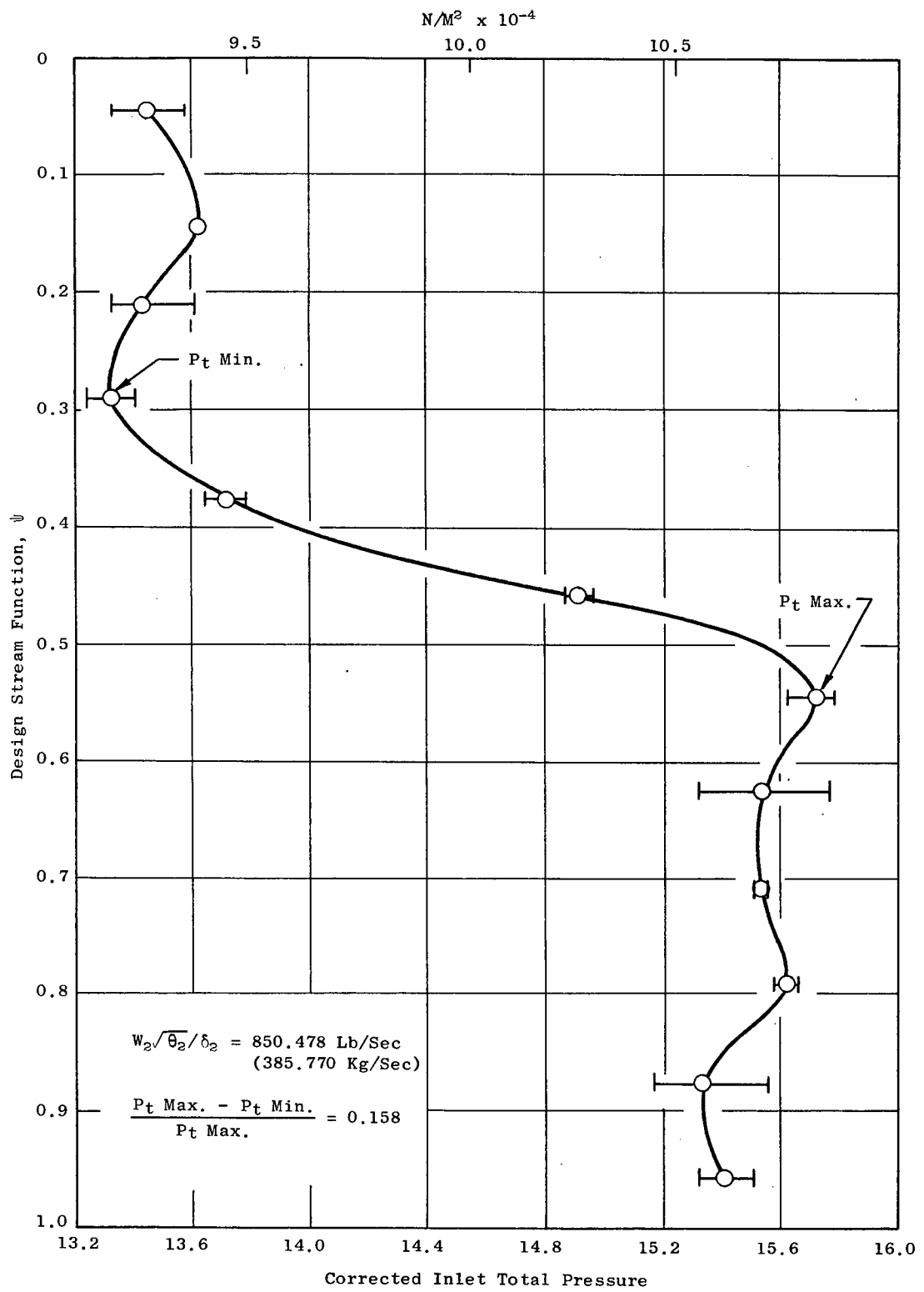


Figure 43. Tip Radial Distortion Inlet Pressure Profile.

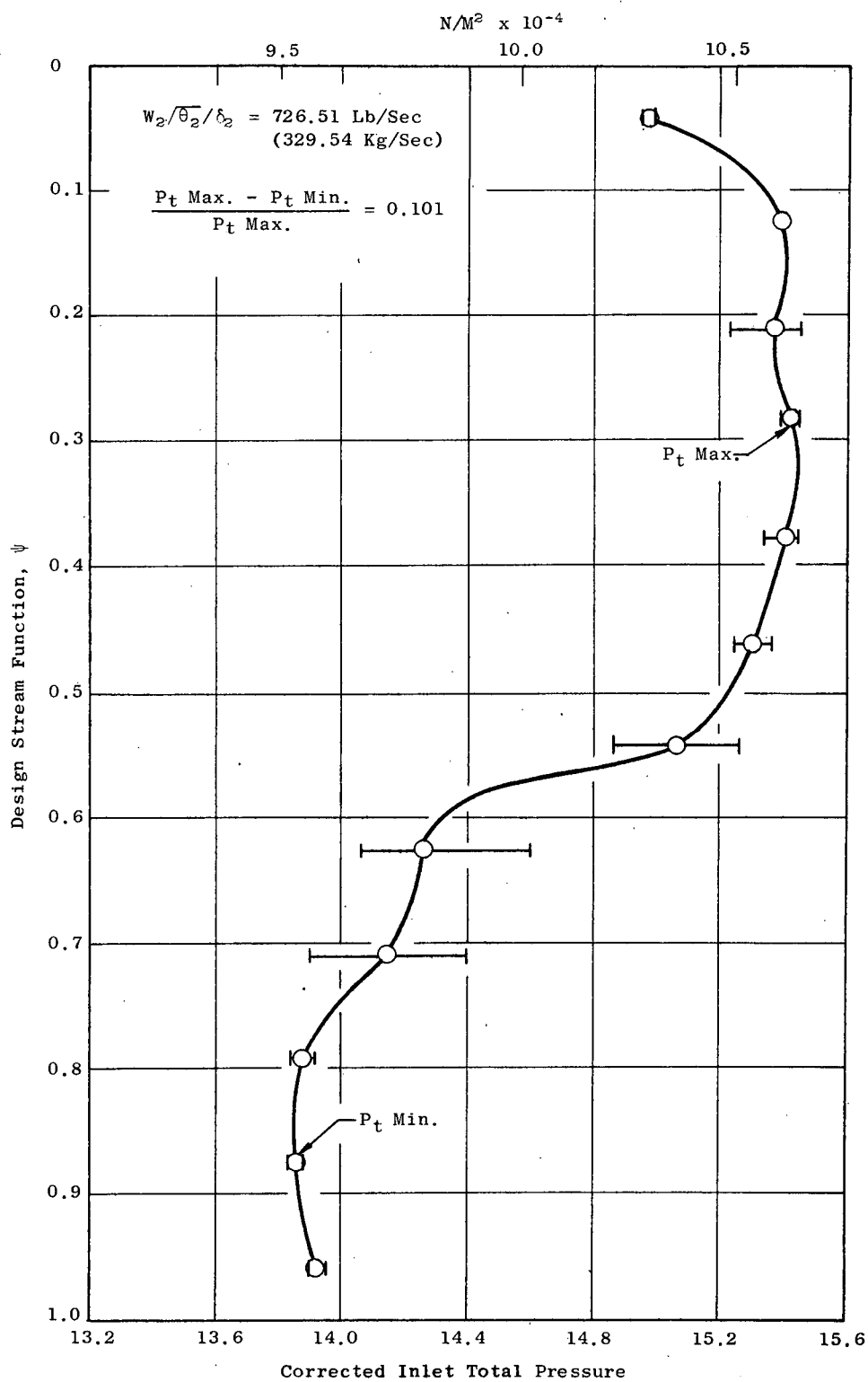


Figure 44. Hub Radial Distortion Inlet Pressure Profile.

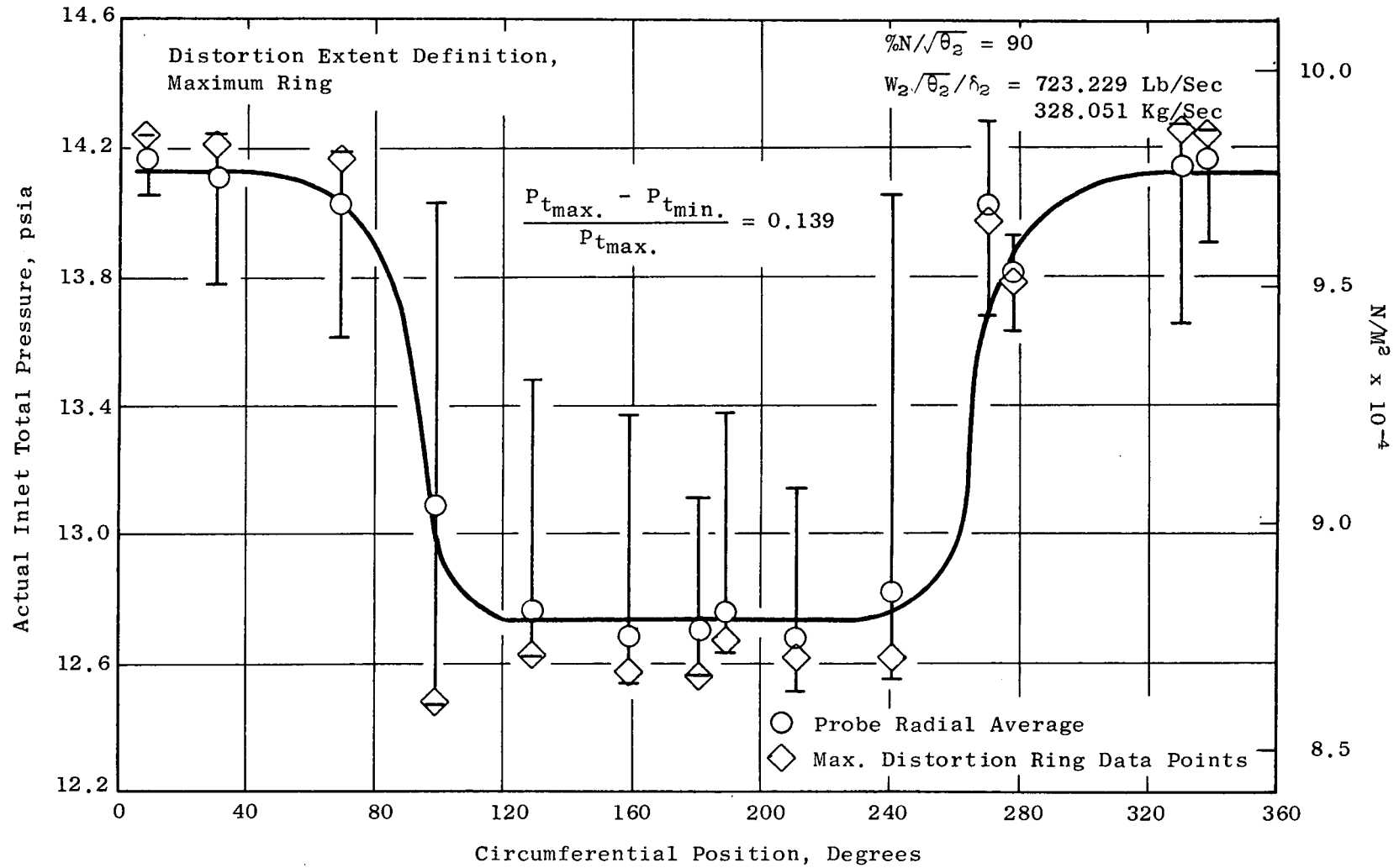


Figure 45. One/Rev Distortion Pattern.

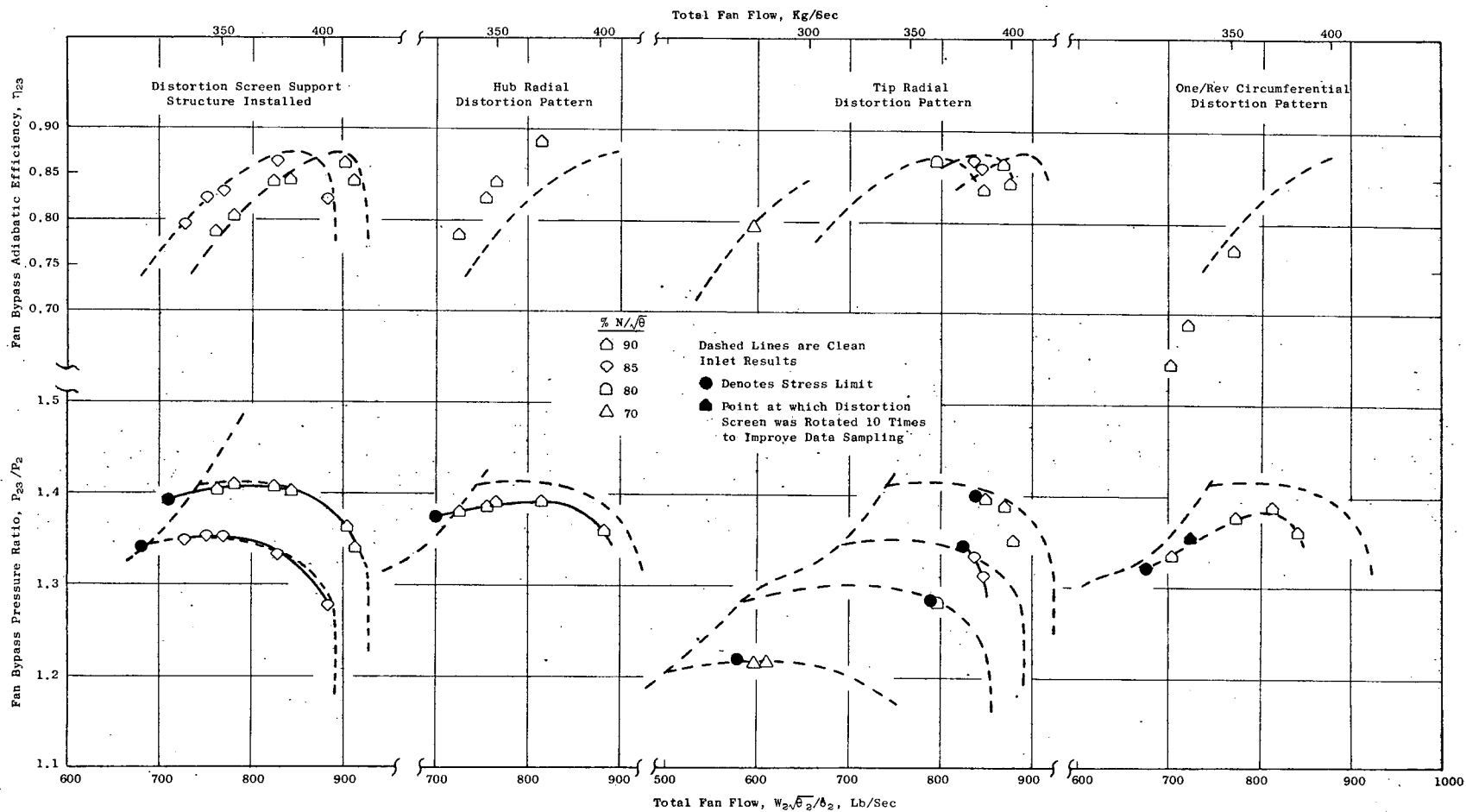


Figure 46. Demonstrated Fan Performance Distortion Patterns in Inlet.

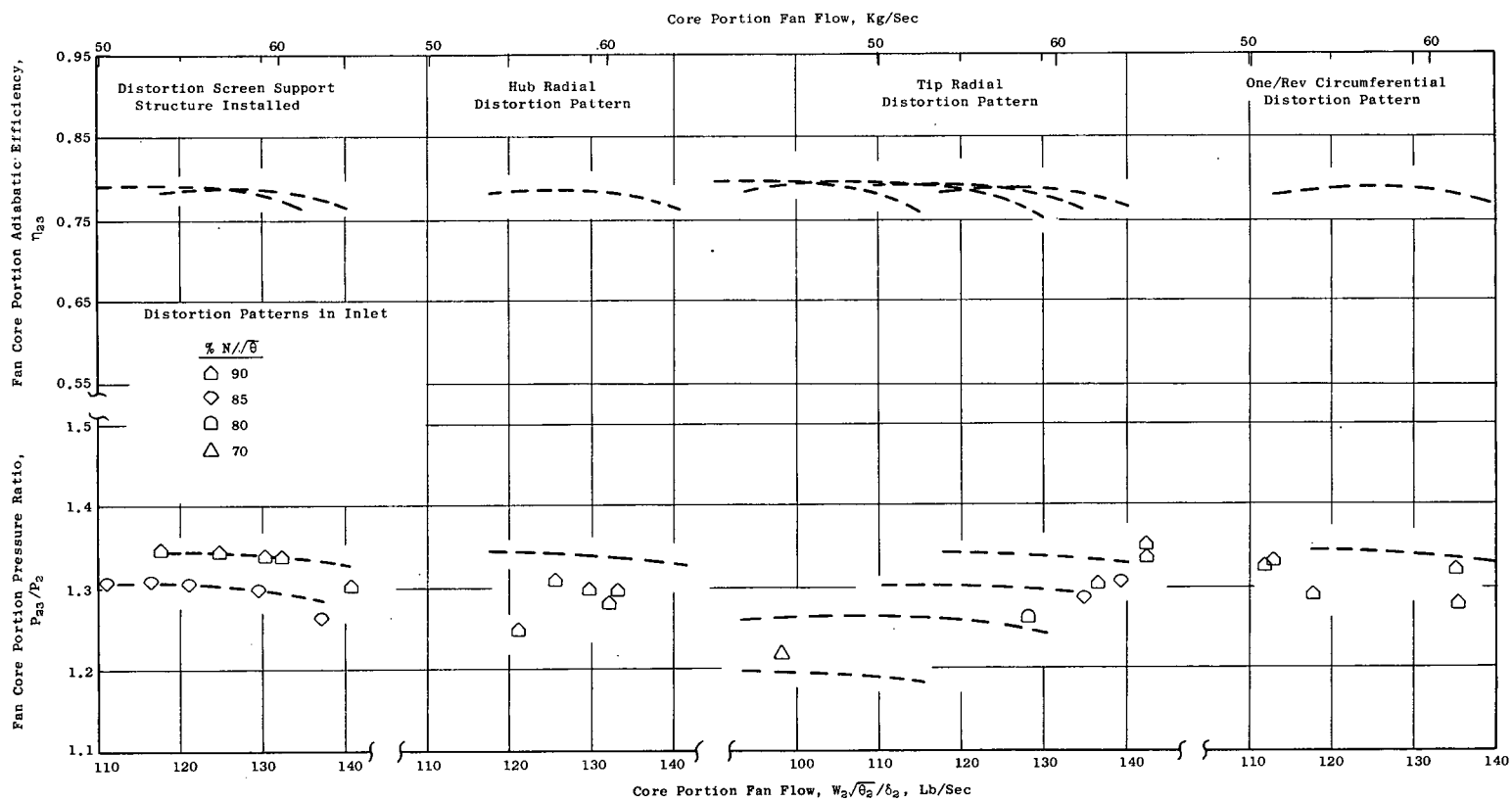


Figure 47. Demonstrated Core Portion Fan Performance Distortion Patterns in Inlet.

6.0 SUMMARY OF RESULTS

The aerodynamic component test results of Fan B, one of two high-bypass-ratio, 1160 feet per second (353.6 m/sec) single-stage fans, which was designed to deliver a bypass pressure ratio of 1.50 with an adiabatic efficiency of 87.0% at a total fan flow of 950 lbs/sec (430.9 kg/sec) yielded the following principal results:

1. With undistorted inlet flow, a bypass pressure ratio of 1.52 and an adiabatic efficiency of 86.9% at a total fan flow of 966 lb/sec (438.2 kg/sec) were actually achieved at design speed. The peak adiabatic efficiency at design speed was 87.1% at a bypass portion pressure ratio of 1.507 and a total fan flow of 976 lb/sec (442.2 kg/sec). The operating margin achieved at this speed was 19.5% and was 10.9% at 90% speed. At 110% corrected speed, a total fan flow of 1020 lbs/sec (462.7 kg/sec) was achieved which gave a specific flow of 44.3 lb/sec/ft² (211.5 kg/sec/m²) of annulus area. A fan core pressure ratio of 1.425 at an adiabatic efficiency of 77.0% was achieved at 100% corrected speed and the design flow of 147.3 lb/sec (66.8 kg/sec).
2. With the distorted inlet flow, the hub radial and one-per-rev circumferential distortions resulted in no decrease and a slight decrease in fan operating margin, respectively. The loss in operating margin with the tip radial distortion was far greater, with the largest loss occurring at 80% corrected speed. The pressure profile distortion level was approximately 15% at 90% corrected speed.

PRECEDING PAGE BLANK NOT FILMED

7.0 REFERENCES

1. Experimental Quiet Engine Program, Contract No. NAS3-12430,
Phase 1 Engine Design Report, Volume 1, Section 4.0
Fan Aerodynamic Design, NASA CR-72967, March 15, 1970
2. Seyler, D.R. and Gostelow, J.P; "Single Stage Experimental
Evaluation of High Mach Number Compressor Rotor Blading,
Part 2 - Performance of Rotor 1B," NASA CR-54582, Sept.
22, 1967.

Preceding page blank

APPENDIX I

INSTRUMENTATION

An overall meridional view of the test vehicle with the test instrumentation superimposed is shown in Figure 48. The fan inlet conditions were measured by four six-element pitot-static rakes located in the cylindrical section of the inlet duct between the bellmouth and the fan inlet. Twenty-four thermocouples attached to the inlet FOD screens were used for determination of inlet total temperature. The pressure and temperature sensors were located approximately on centers of equal area. The fan discharge total temperature and total pressure were measured by arc rakes. Seven arc rakes were located behind the fan bypass portion outer OGV's, and five arc rakes were located behind the fan core portion inner OGV's. Radially, the arc rakes were located on centers of equal design mass flow of the bypass portion and fan core portion, respectively.

The bypass portion arc rakes were composed of 12 elements with each element containing one temperature and one pressure sensor. This construction technique enables pressure and temperature sampling from a common fluid region and minimizes the effects of spatial variation in computing efficiency. The two outer arc rakes spanned one OGV spacing. The remaining five arc rakes spanned two OGV spacings. The five core portion arc rakes were of similar construction to that of the bypass portion arc rakes but with seven elements each containing one total pressure and total temperature sensor. These rakes spanned two OGV spacings.

The rotor discharge total pressure in the fan core portion was measured by three five-element radial rakes. The radial positioning of the elements were on centers of equal design flow. The total pressure at discharge from the transition duct leading to the core compressor was measured by five five-element radial rakes with the elements being located on centers of equal area. (These rakes are identical with those used for core compressor inlet instrumentation on the TF39/CF6 engines.)

In addition to this instrumentation, there were wall static pressures located in the inlet duct and along the outer casing, along the inside diameter of the bypass portion, around the splitter leading edge, and throughout the ducting for the fan core portion flow. Total pressure profile rakes were located on the inlet duct outer casing just forward of the fan rotor and on the inside diameter of the bypass portion midway between rotor exit and outer OGV inlet. The total number of pressure sensing elements exceeded the recording capability of the test stand. Three alternate pressure matrices were employed to record those pressures judged most useful for the particular test configuration objectives. Traversing probes were located at fan rotor inlet (a cobra and a wedge static), fan rotor exit (a cobra, a disc static, and a high response Kulite transducer), outer OGV inlet (a cobra), and inner OGV inlet (a cobra). The traverse probes

Preceding page blank

were used only at selected operating points near the aerodynamic design point. Also, 10 Kulite transducers were mounted in the casing over the rotor tip for determination of the time-varying static pressure field.

For the distortion testing, the fan inlet total pressure was measured by three 12-element radial rakes located just upstream of the fan rotor. The elements were positioned radially so as to be on centers of equal design flow.

APPENDIX II
COMPUTATION OF OVERALL FAN PERFORMANCE

The total fan flow was computed from the inlet total and static pressure, the inlet screen total temperature, a measured area, and an assumed flow coefficient of 0.992. Figure 49 is a plot of the normalized outer casing velocity profile forward of the fan face as deduced from the wall static pressure and the total pressure profile rake. The results are presented for four typical flow rates. A computation of the displacement thickness from the boundary layer profile yields an equivalent effective area coefficient of 0.994. The total temperatures and total pressures were recorded individually and arithmetically averaged. Generally, the static pressures were manifolded with only the single manifold value being recorded. However, the first instrumentation matrix recorded the individual static pressures from one of the inlet rakes as a check on the radial pressure profile. The inlet total and static pressure profiles for a typical high flow point are presented in Figure 50. The static pressure profile is nearly constant radially, as expected. The total pressure profile is slightly skewed towards the outside diameter; however, this skew is typical of all data points. It is believed that the closeness of the inlet bellmouth to the facility protection screen is responsible for the skew since the potential flow field in front of the bellmouth will have its highest velocity along the centerline, and, hence, this location will yield the largest screen pressure drop. The fan core portion flow was measured by a calibrated flow meter located in the facility discharge piping. The bypass portion flow is obtained by subtracting the fan core portion flow from the total fan flow; no independent measurement of the fan bypass flow was made.

The fan face total temperature and total pressure was taken as the arithmetic average of the screen-mounted total temperatures and pitot-static total pressures. At discharge, the fan bypass portion and fan core portion are treated separately. For each portion, the arithmetic average of the pressures and temperatures for each arc rake is computed. (The average excludes the last element on each rake, the 12th element on the fan bypass portion rakes, and the seventh element on the fan core portion rakes since this element is spaced one blade pitch from the first element and is, therefore, redundant for performance computation. This last element was incorporated to provide a check on the periodicity of the flow leaving the OGV's.) A linear variation in static pressure between wall measured values at the outside diameter and inside diameter was assumed. The averaged total temperature reading at each immersion is corrected for static wire (the error encountered in measuring an oil bath temperature) and Mach number at the Mach number and temperature of that immersion. The procedure then mass weights, radially, the actual enthalpy to obtain an average discharge total temperature and the ideal enthalpy rise to obtain an average discharge total pressure; Reference 2 presents the calculation procedure in detail. With the average pressure ratio and temperature rise of fan bypass portion and fan core portion, the actual air properties, including the effects of humidity, are used to compute the efficiency of the two streams.

Preceding page blank

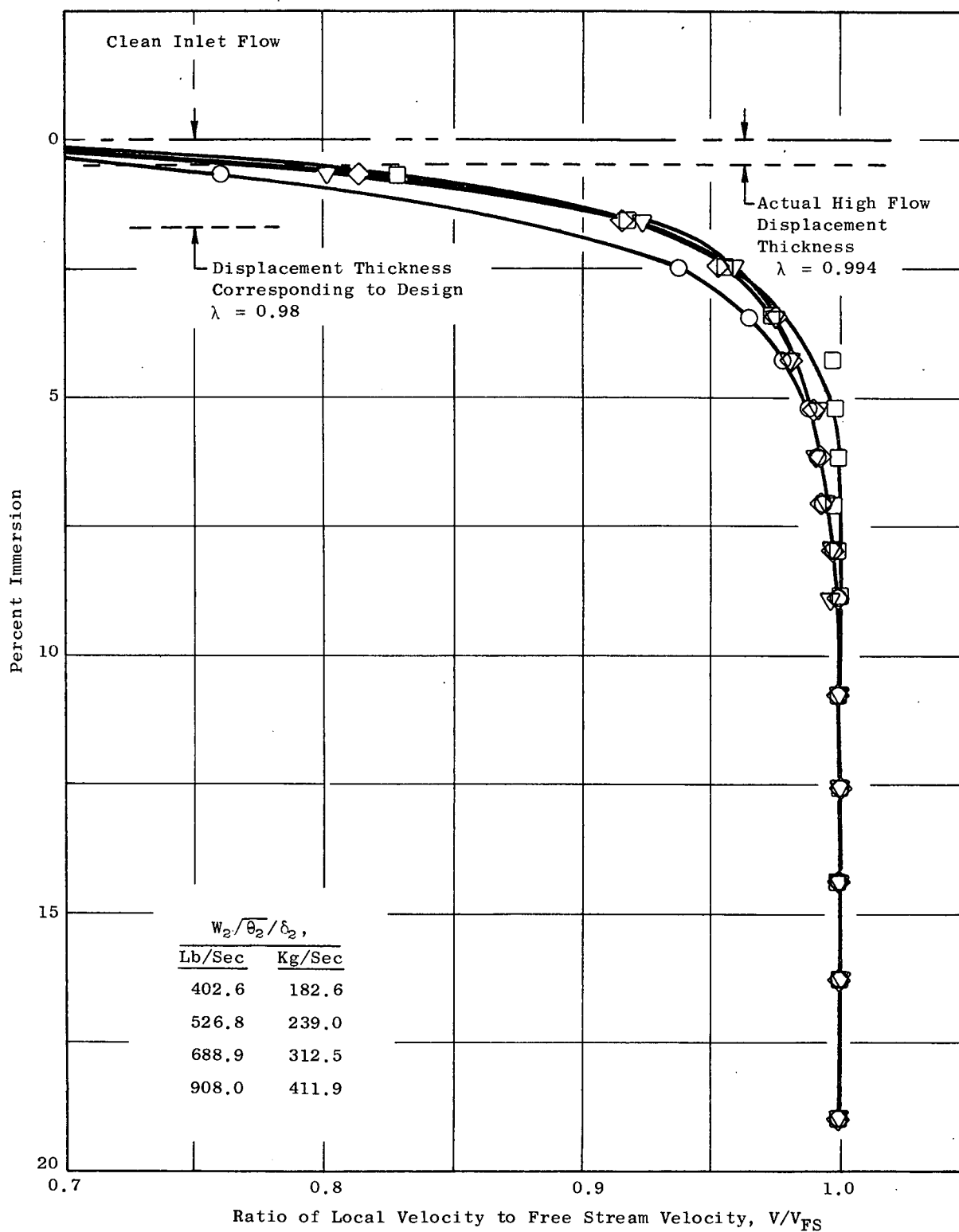


Figure 49. Inlet Boundary Layer Description.

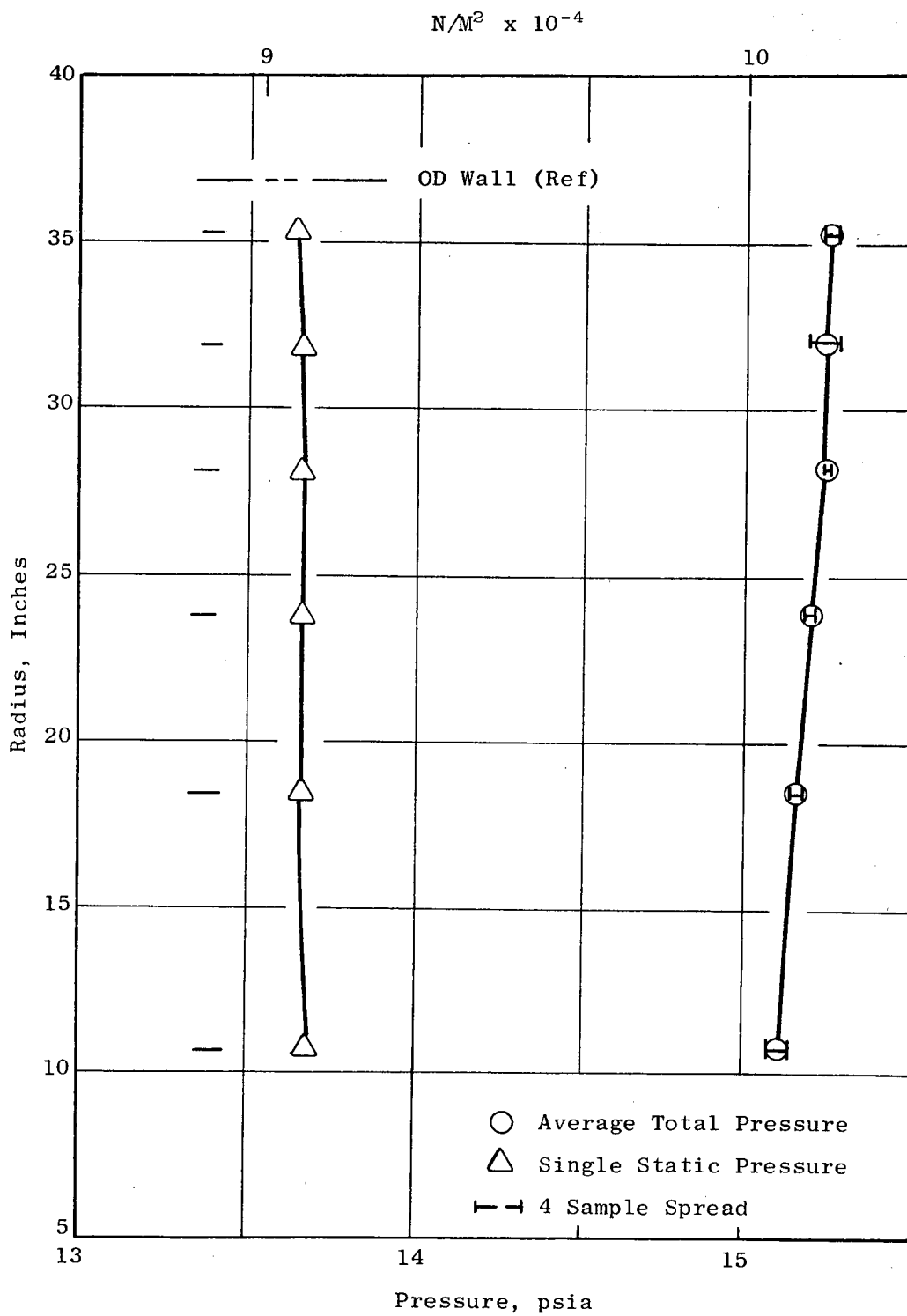


Figure 50. Typical Inlet Duct Pressure Profiles.

A computation was performed to determine the radial variation of stage and rotor only adiabatic efficiency and OGV total-pressure-loss coefficient and static-pressure-rise coefficient. A constant ratio of specific heats is used in these computations. The calculations assume the arithmetically averaged wake rake total pressure and total temperatures at OGV discharge. No change in total temperature is permitted through the OGV. For the bypass portion, the average of the three highest total-pressure-wake-rake elements is assumed to be the pressure in front of the OGV. In the fan core portion, each of the five elements on the three radial rakes at rotor exit were averaged circumferentially to determine the OGV inlet total pressure. At inlet and discharge the stream static is obtained by linear interpolation between wall values.

DATA ACCURACY

Pressure

The recording system for pressure uses a method whereby each transducer (which measures up to 10 vehicle pressures) is calibrated on each reading against a CEC electromanometer which in turn is calibrated before and after each test against a dead-weight tester which can be traced to the National Bureau of Standards. This procedure results in an overall accuracy of pressure measurements of $\pm 0.25\%$ of level.

Temperature

The recording system used for temperatures has a readability of one microvolt and is periodically calibrated against a standard which is traceable to the National Bureau of Standards giving an overall accuracy of recording of ± 3 microvolts or approximately $\pm 0.12^\circ$ F.

In addition, static wire and dynamic recovery ratio calibrations are performed on all sensors used for performance measurements. It is estimated that the overall RMS temperature measurement accuracy is $\pm 0.5^\circ$ for CC wire and $\pm 0.75^\circ$ for CA wire.

Flow

There is no error in the total pressure sensed by the inlet pitot-static instrument. The static pressure sensed by the inlet pitot-static instrument has, under ideal conditions, an estimated error of 0.25% of the dynamic pressure. However, because of minute differences in probe-to-probe manufacture and or alignment, a sensing error of 1% of the dynamic pressure can be expected.

The data acquisition accuracy (or more appropriately inaccuracy) are the extremes expected for the individual element measurements. Since some elements read high while other elements read low it is more reasonably expected that the overall performance inaccuracies are on the order of one-fourth of the inaccuracies of the individual elements. The problem of data sampling is at least as important in overall performance accuracy as the ability to properly sense and record the data. A treatment of this problem is beyond the scope of the current report.

APPENDIX III

OVERALL PERFORMANCE DATA FOR BUILD I

The build 1 measured performance of the Fan B stage is shown in Figures 51 and 52. The build 1 performance can be compared with the build 2 performance which was presented in Figures 4 and 5 along with the fan core portion performance comparison already made in Figure 32. Referring to the bypass portion map the only significant difference noted between build 1 and build 2 is the operational limit line in the region of 85% speed, wherein build 1 has significantly less operating margin. In both builds, the limit line was set by high rotor stress rather than aerodynamic stall. The reason for the improved operating margin on build 2 was the higher permissible absolute stress level made possible by the material change. The fan core portion comparison was discussed relative to Figure 32.

The build 1A vehicle was tested in the presence of a tip radial, hub radial, and one-per-rev circumferential inlet flow distortion. The distortion was generated by screens mounted on a support structure which was located approximately 0.6 fan diameters in front of the rotor. The tip and hub radial distortion generating screens covered the outer and inner 40% of the annulus, respectively. The one-per-rev distortion extended over the full annulus height and was 180° in circumferential extent. Plots of the actual distortion patterns for representative readings at 90% corrected speed are shown in Figures 53 through 55. As is noted in these figures, approximately 10% distortion was obtained. The overall bypass portion maps for this distorted inlet flow testing are shown in Figures 56 through 58. As was noted for build 2 distortion testing, the hub radial and one-per-rev circumferential distortions resulted in only modest decreases to the fans operating margin. The tip radial distortion resulted in a greater reduction in fan operating margin with the greatest reduction occurring at 80% speed.

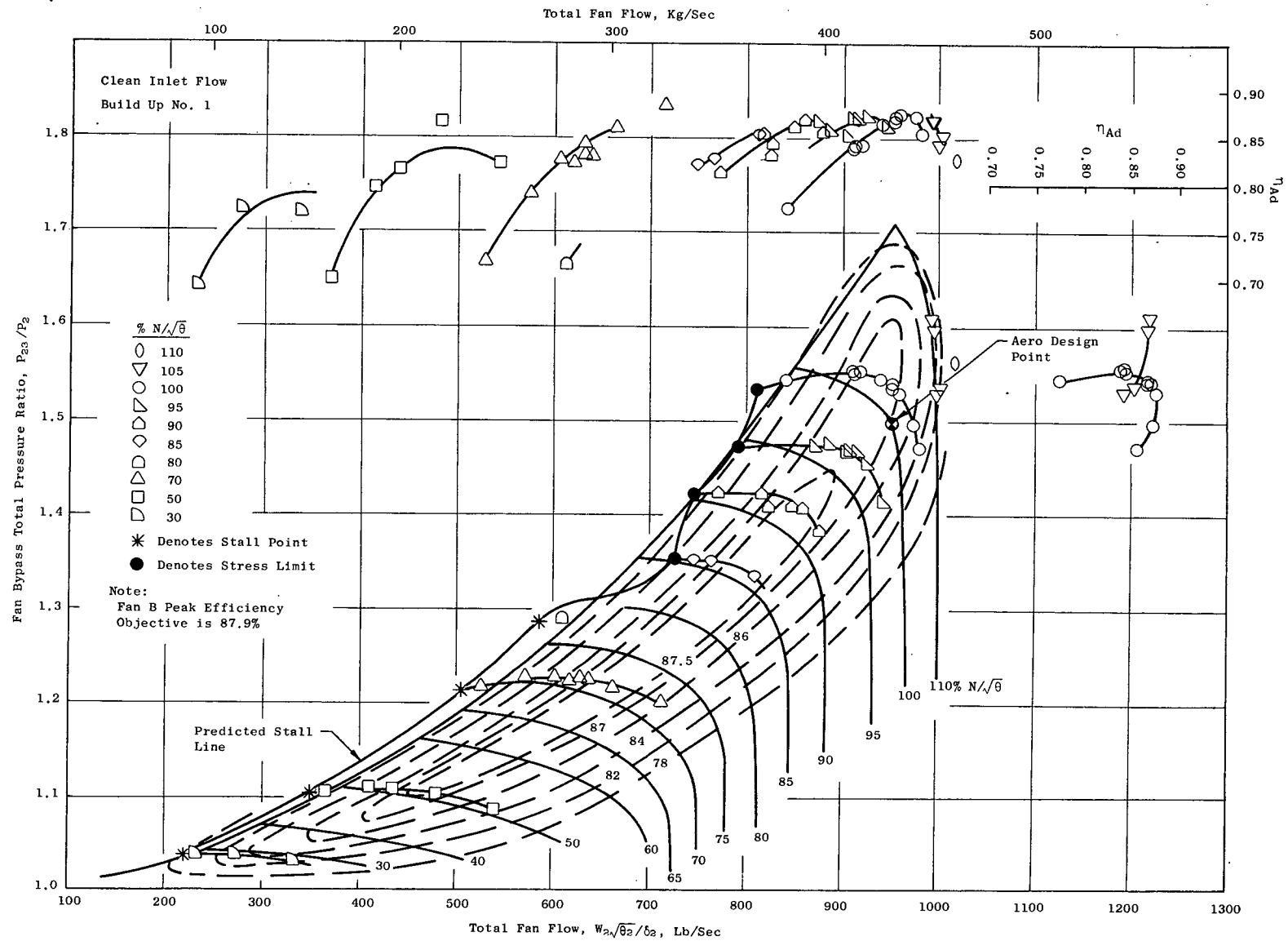


Figure 51. Fan B Performance Map, Fan Bypass Total Pressure Ratio Vs. Total Fan Flow.

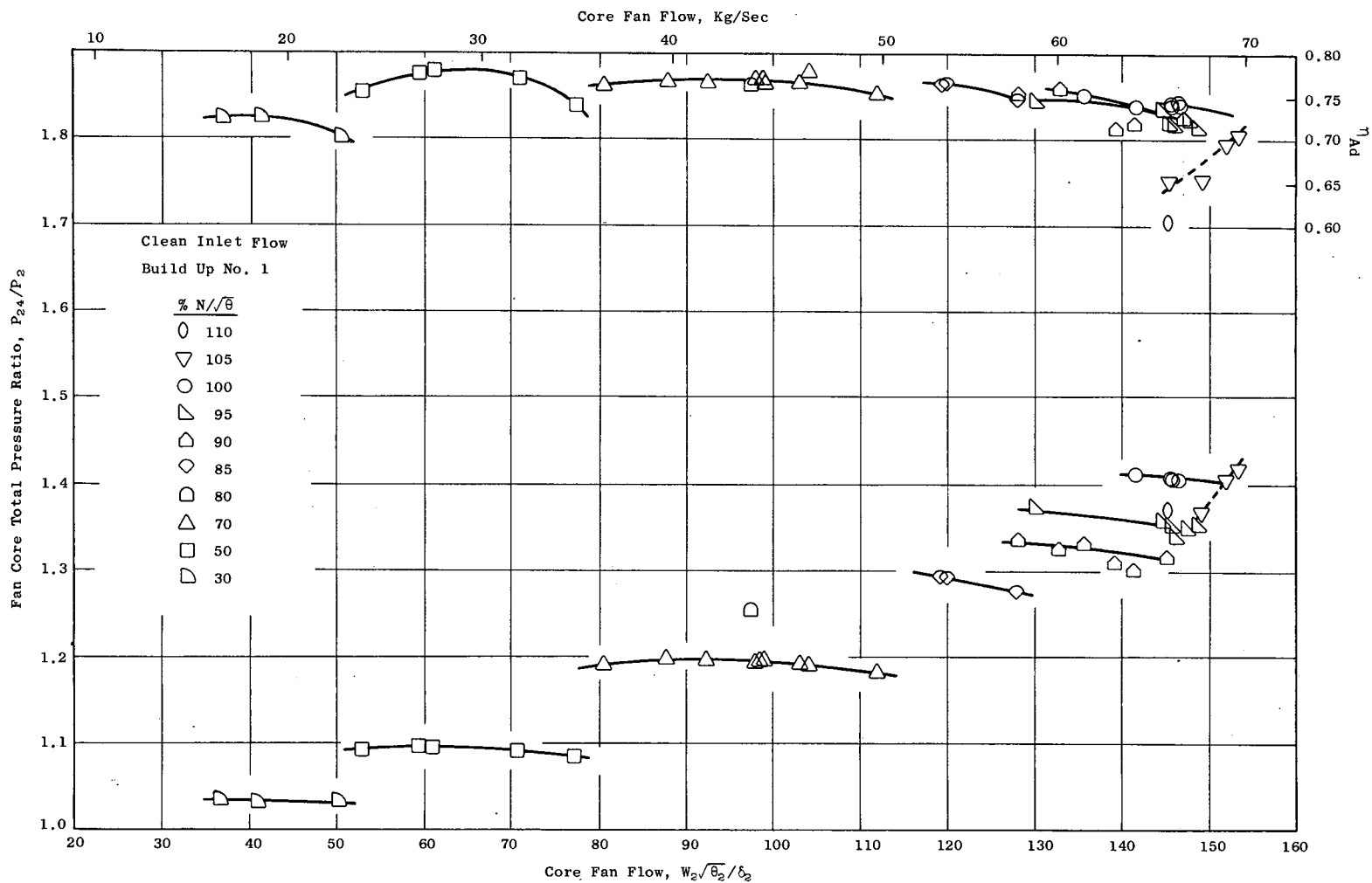


Figure 52. Fan B Performance Map, Fan Core Total Pressure Ratio Vs. Core Fan Flow.

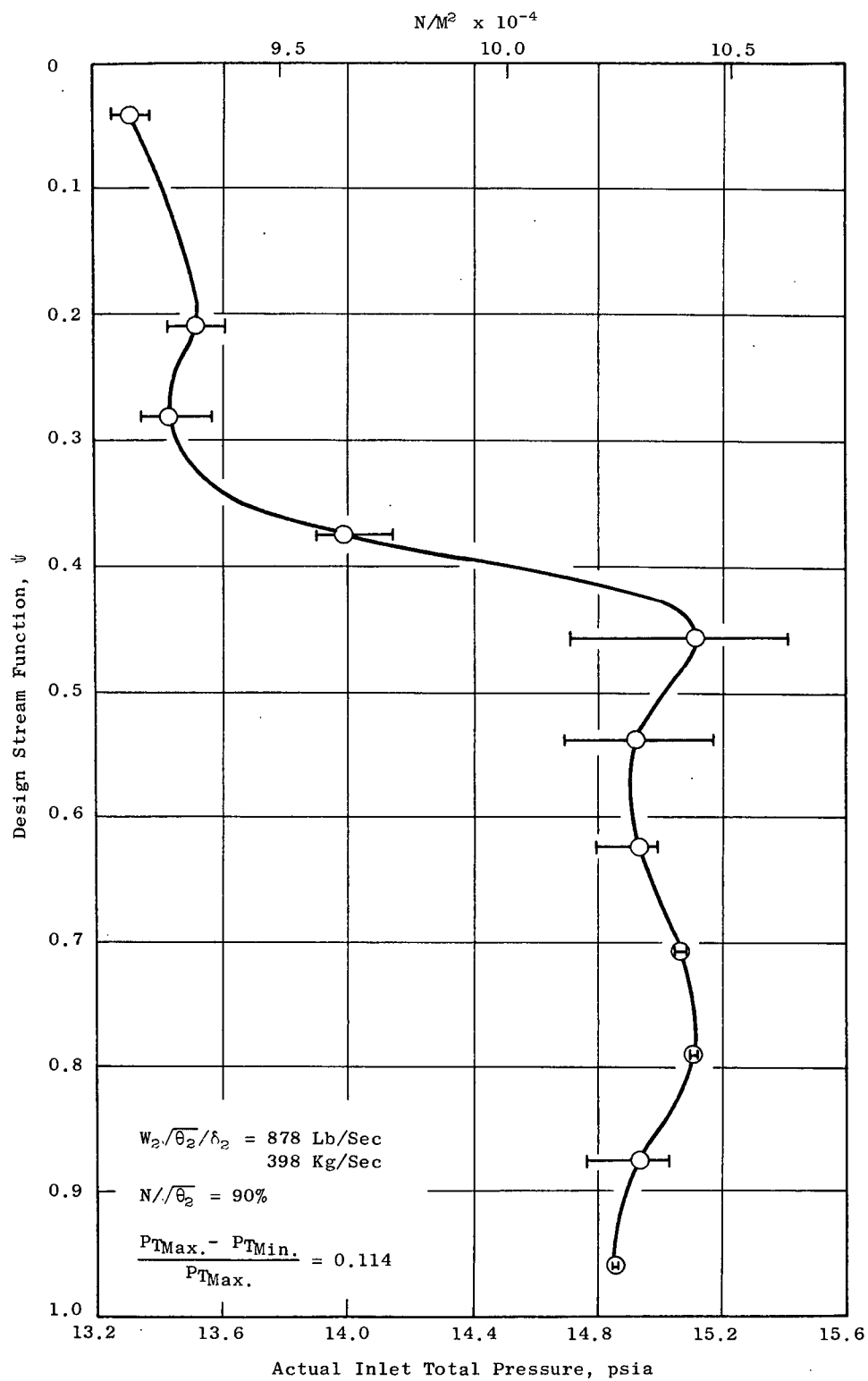


Figure 53. Tip Radial Distortion Inlet Pressure Profile.

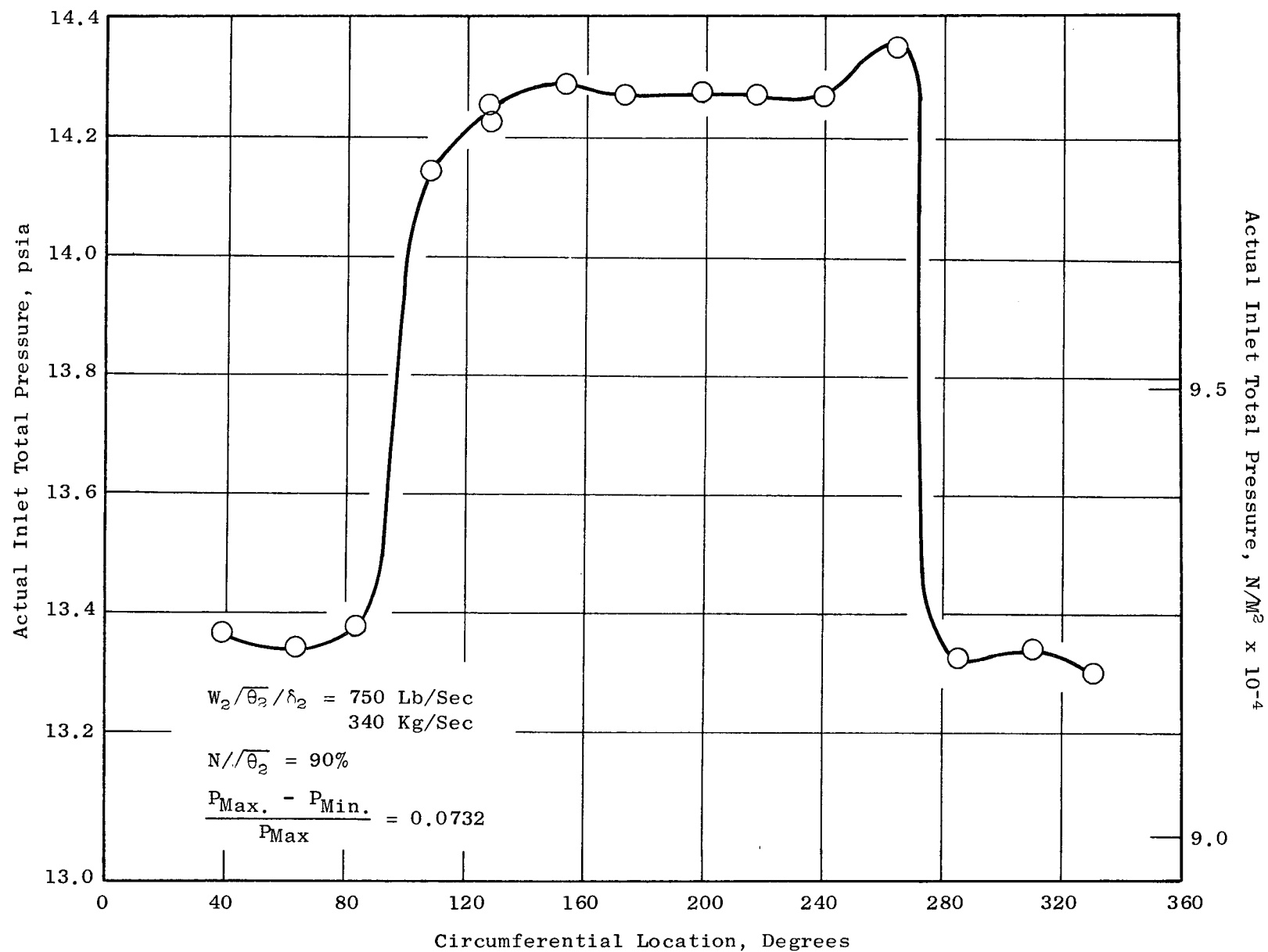


Figure 55. One/Rev Distortion Inlet Pressure Profile.

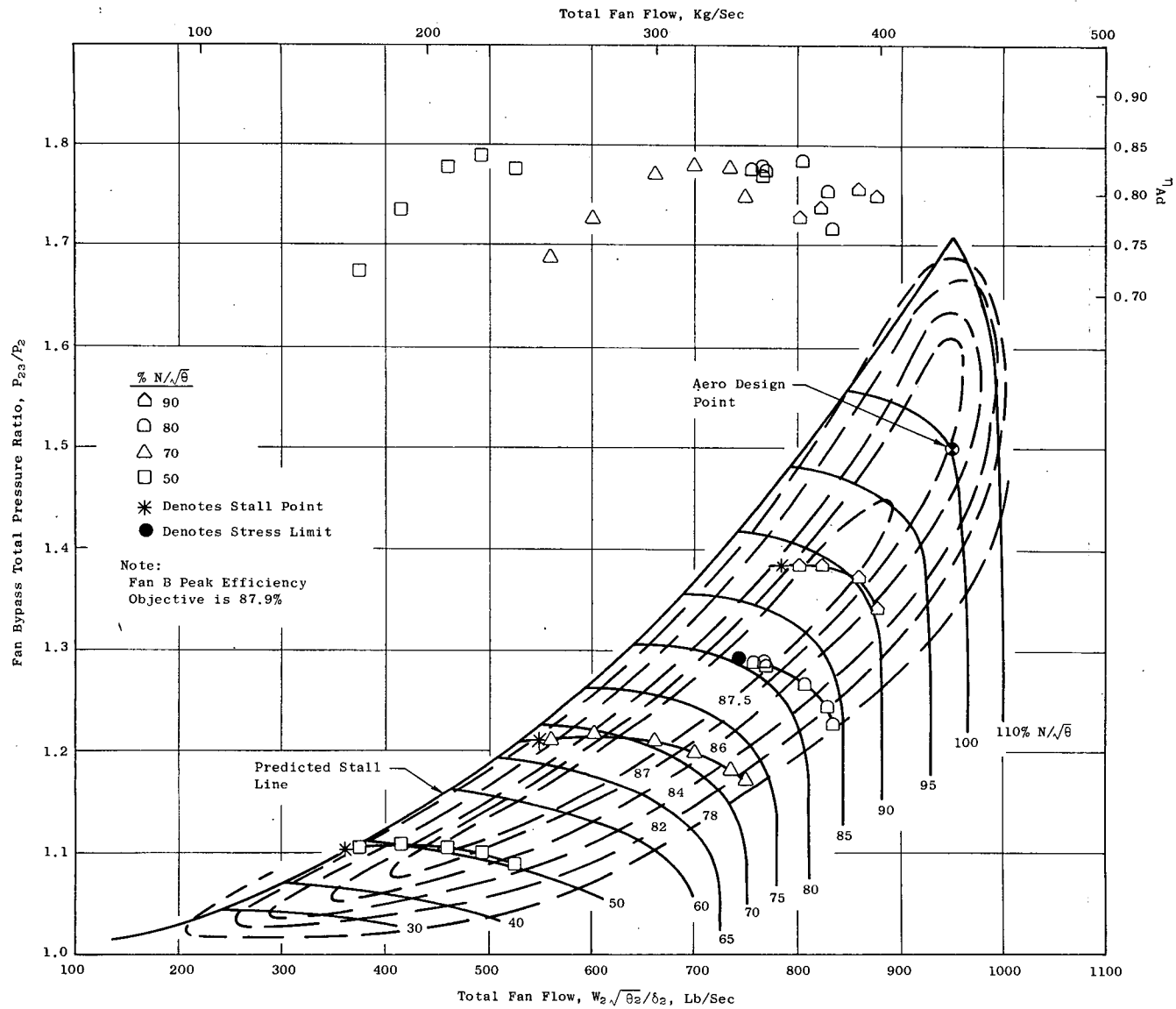


Figure 56. Fan B Performance Map, Tip Radial Distortion (Build 1).

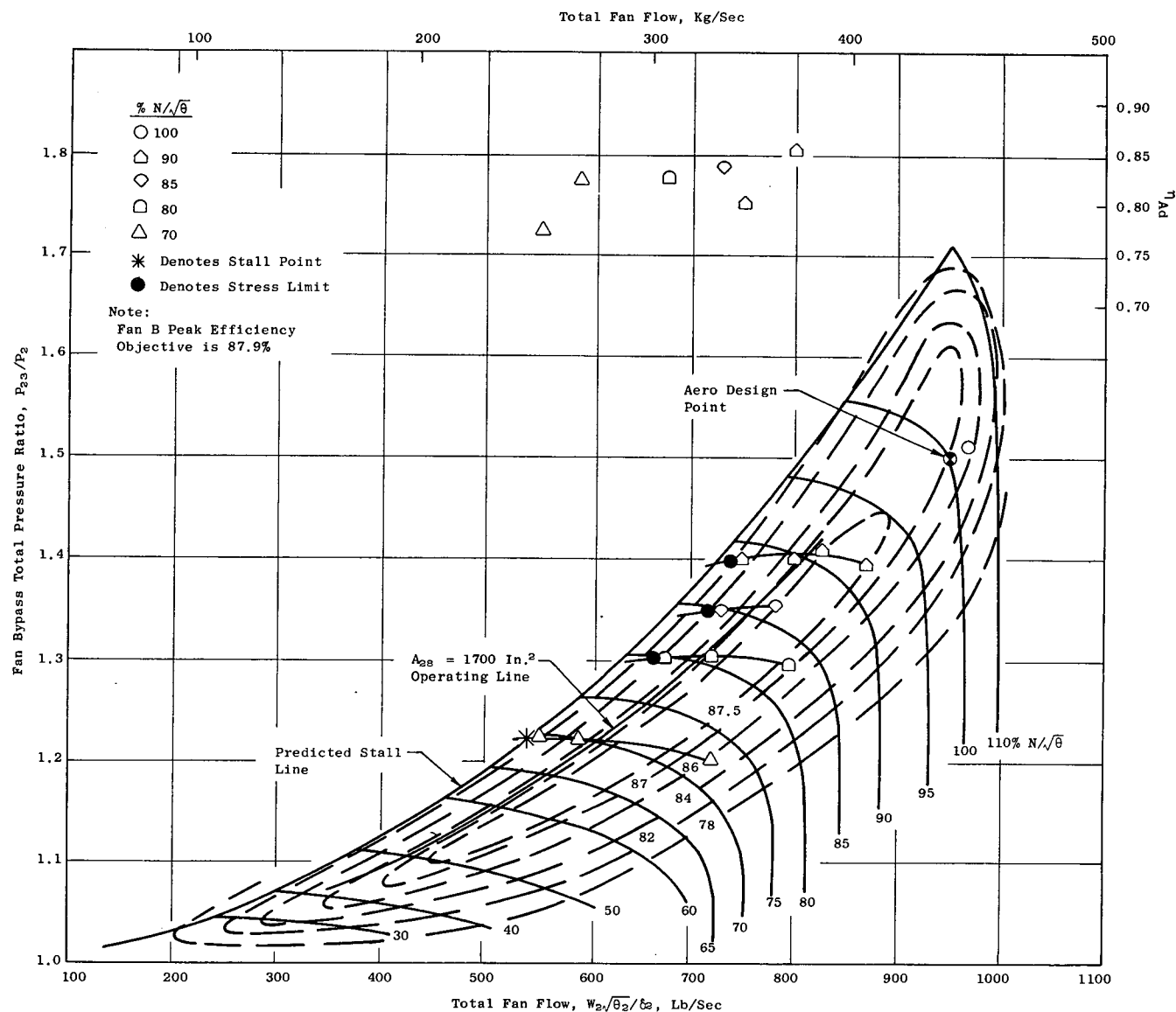


Figure 57. Fan B Performance Map, Hub Radial Distortion (Build 1).

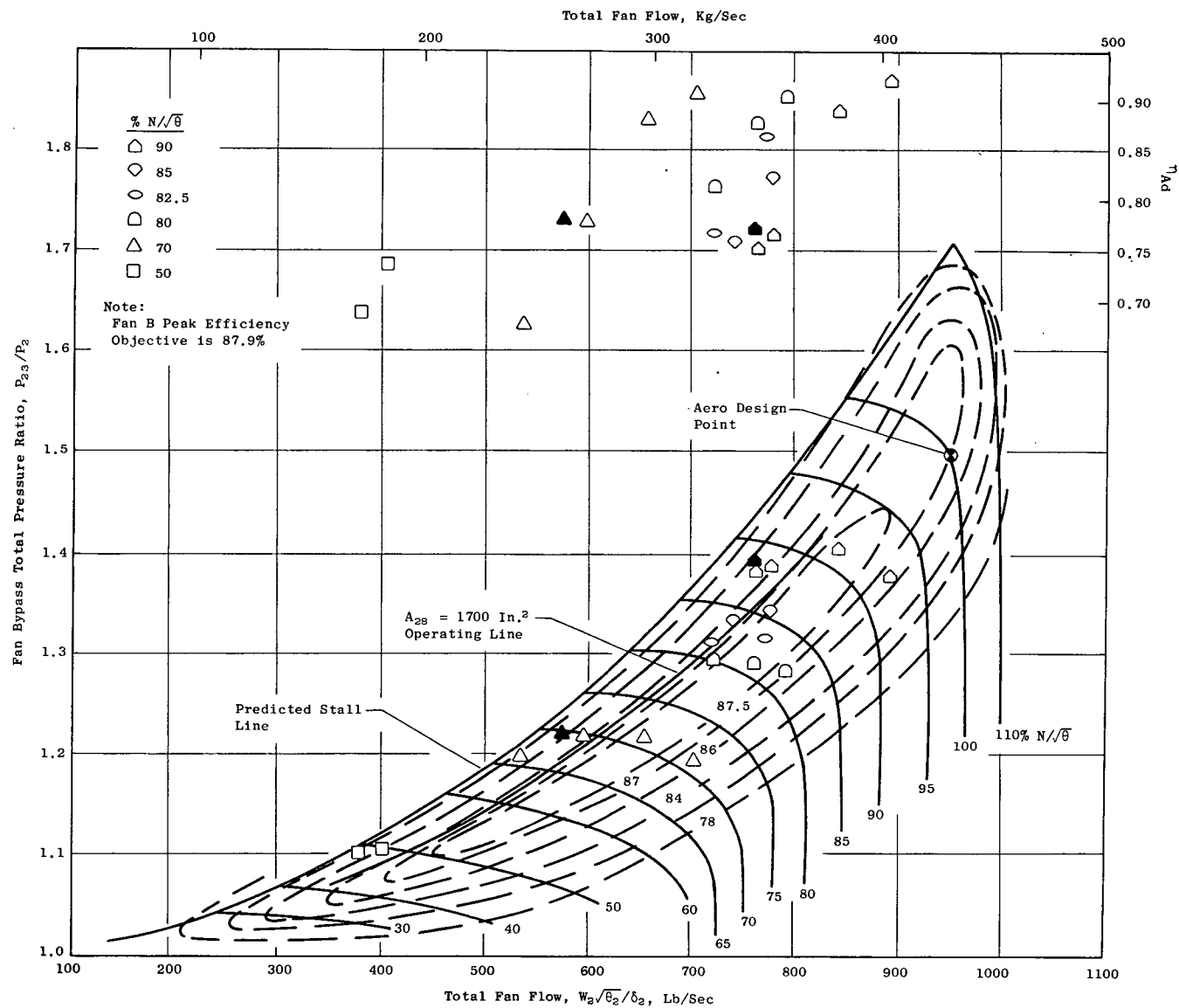


Figure 58. Fan B Performance Map, One/Rev Distortion (Build 1).

APPENDIX IV

Rotor Tip Pressure Patterns

Ten Kulite transducers were mounted in the casing over the rotor tip to determine the time-varying static pressure field caused by the passage of the rotor blades. The electronic signal from the Kulite transducers was displayed on an oscilloscope. The oscilloscope sweep rate was synchronized with rotor speed and the start of the sweep cycle was triggered with a one-per-rev indicator such that a time-steady picture of the pressure variation within a selected number of blade passages appeared on the scope screen. The vertical scale of the scope was calibrated by inputting a known pressure differential and measuring a deflection. The horizontal time or distance scale was calibrated by a clearanceometer which indicates the passing of each blade. The horizontal scale was adjusted such that two blade passages were displayed on the scope screen. The method of data recording was to photograph the screen image. Figure 59 shows the recorded data for the 100% corrected speed point. A wall static pressure tap was located in the same axial plane as each Kulite. The data reduction method assumes that the wall static pressure tap recorded a true average value and that differences from the average could be added or subtracted according to the differences from the average, as deduced from the photographs. An average trace was deduced from which these differences were obtained by digitizing the photograph over both blade passages and performing a numerical average.

The Kulite data presented herein were recorded for Build 1. Several of the Kulites were inoperative for Build 2 and since no significant overall performance differences existed between the two builds, Build 1 was selected to enable a more complete and accurate presentation of the data. A total of nine readings were reduced into the form of static pressure contours. Figure 60, which shows a skeleton of the overall bypass performance map previously presented in Figure 4, shows the data points selected for analysis. The readings were generally selected so as to be representative of a constant area operating line changing from sea level static operation at 90% corrected speed (takeoff) to altitude cruise operation at 100% corrected speed. In addition, readings at two other operating lines were selected at 90% corrected speed. The figure number of the isobar plot appears adjacent to the data point.

Figures 61 through 69 present the isobar plots for the nine reduced readings. Adjacent to the axial distance scale a triangular symbol shows the location of the Kulite transducer. Only nine Kulite transducers are indicated; the tenth, which was located forward of those shown, was inoperative for the majority of the testing. Shown as an inset on each of these figures is the axial distribution of static pressure, as measured by the wall static pressure taps, for that reading.

Referring to Figure 62, the 100% corrected speed reading, the entrance shock is normal to the incoming flow for approximately one-half of the channel width from the blade leading edge to the adjacent blade suction surface. The

Preceding page blank

normal shock then changes into an oblique shock for the second half of the afore mentioned channel width. The static pressure rise for the normal portion of the entrance shock is approximately that predicted by standard normal shock relations. Assuming a relative total pressure equal to the upstream value, a maximum suction surface Mach number of 1.37 is estimated; the inlet relative Mach number is 1.27. Aft of the entrance shock an acceleration occurs which terminates in a normal shock in the aft region of the covered portion.

As the corrected speed is increased to 105%, Figure 61, the entrance shock becomes essentially oblique across the entire passage. For the region of the shock adjacent to the leading edge the measured static pressure ratio and shock angle require approximately a six-degree deflection at the Mach number in front of the shock which is reasonably internally consistent with the expected deflection angle. Adjacent to the pressure surface, a marked weakening of the entrance shock strength is noted. This marked weakening is also observed at 100% corrected speed, but at the lower speeds this weakening is not noted. One contributing factor to explain this observation is that at corrected speeds below 100% the shock intersects the suction surface of the adjacent blade forward of the region where any significant accelerating curvature occurs. At and above 100% corrected speed, the suction surface has significant accelerating curvature prior to the intersection of the entrance shock. It is further suspected that characteristics of the opposite family as those of the shock, generated by this accelerating curvature, are partially responsible for the reacceleration of the flow along the pressure surface aft of the entrance shock. The oblique entrance shock at 105% corrected speed appears to reflect from the suction surface of the adjacent blade and to terminate in a normal shock on the pressure surface of the blade from which it originated.

As the corrected speed is lowered from 100%, the entrance shock becomes essentially normal and progressively moves forward of the leading edge, as expected. The strength of the bow wave which propagates into the upstream flow is a maximum in the 90 to 95% corrected speed region. There is no second shock observed aft of the entrance shock for any corrected speed below 100%. The static pressure on the suction surface of the blade in front of the entrance shock remains low at corrected speeds down to 80%. An estimate of the Mach number in this low static pressure region, using inlet relative total pressure as deduced from the wall static pressure at blade inlet and wheel speed, yields a peak value of 1.42 at 90% corrected speed which diminishes to 1.35 at 80% corrected speed. It was further estimated, that the incidence angle increased by 7.4° and 9.4° as corrected speed was dropped from 100% to 90% and 80%, respectively. This increased expansion from the inlet conditions is of the right order to explain the observed suction surface static pressures.

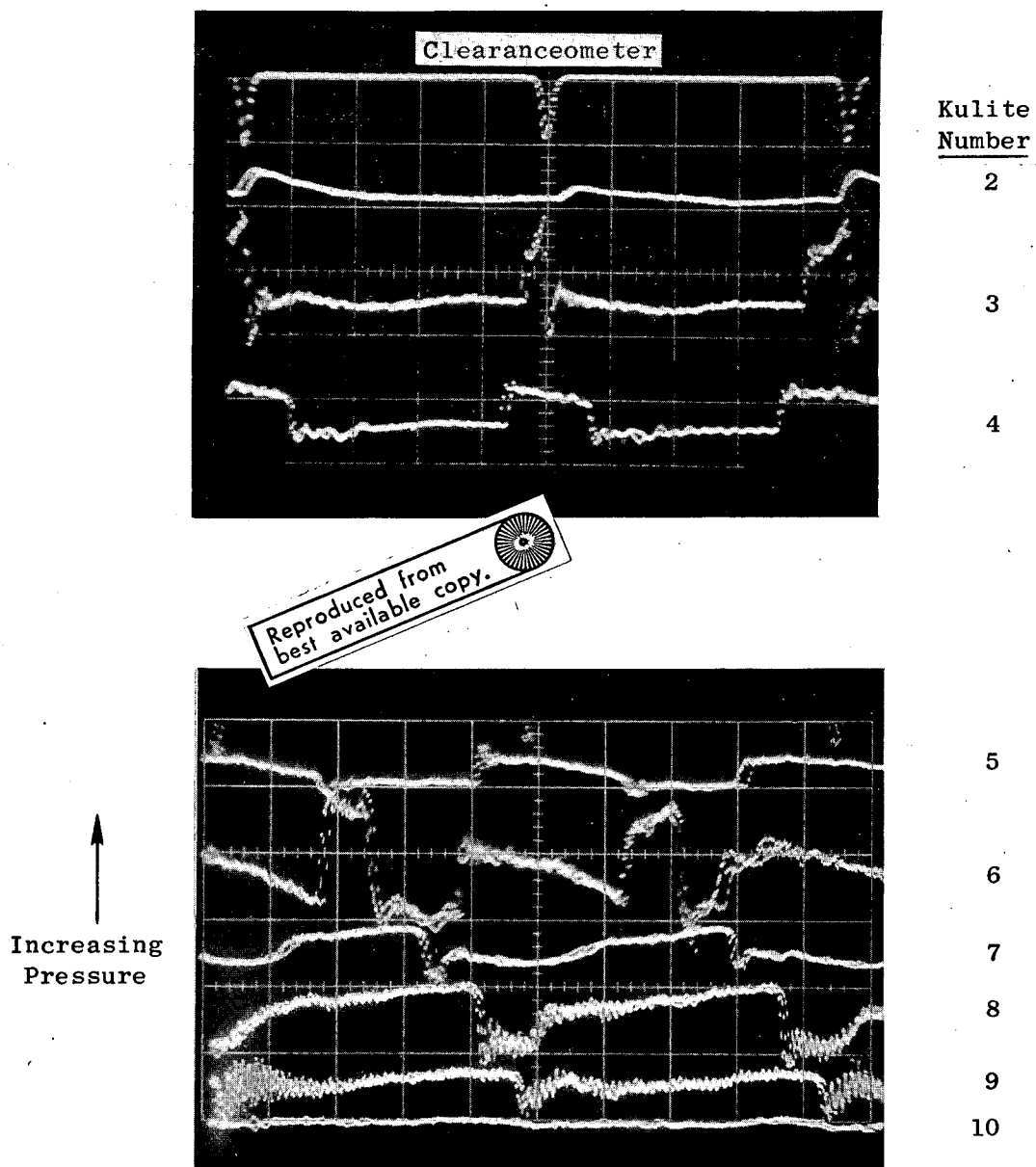


Figure 59. Typical Data Record of Kulite Trace.

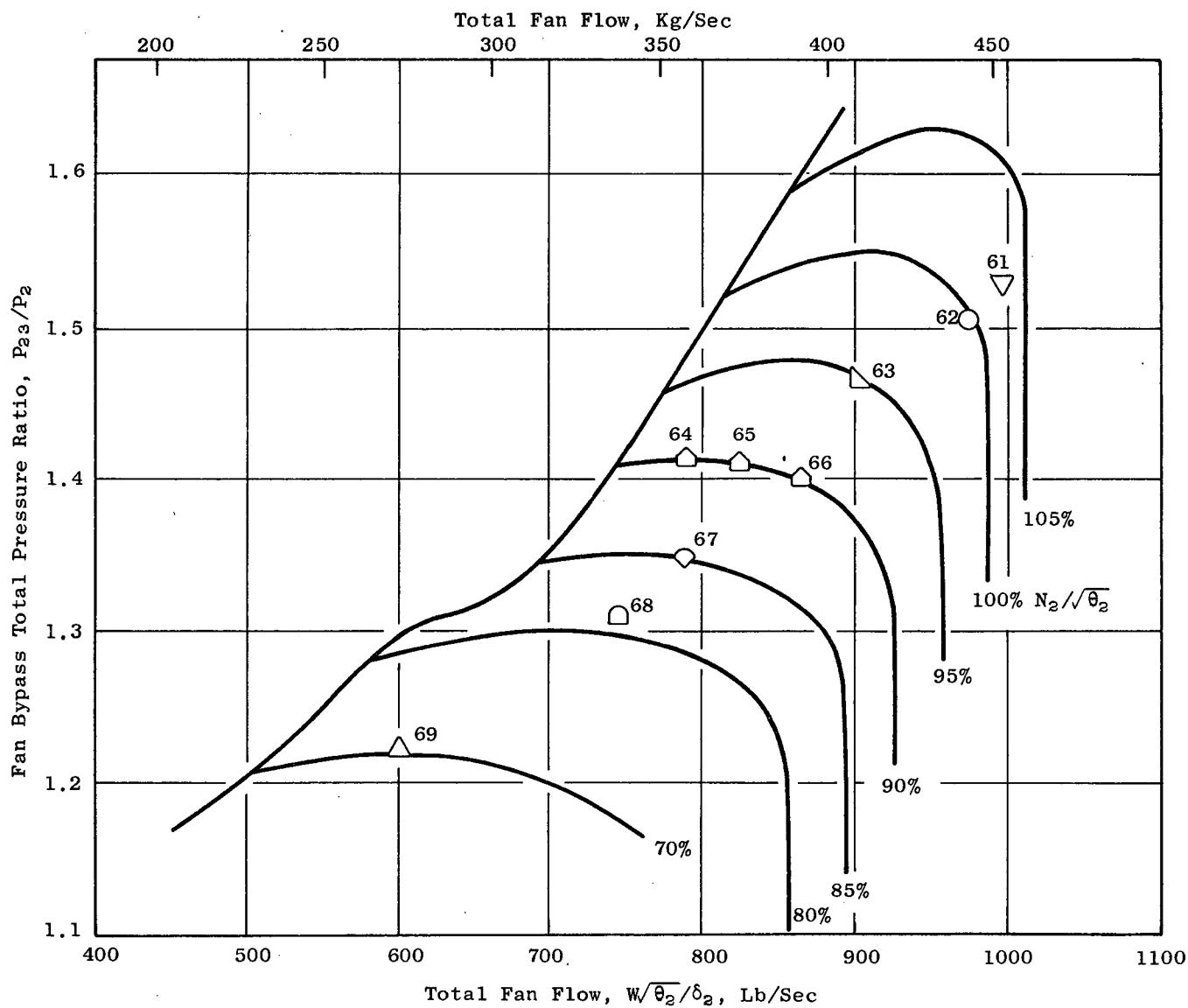


Figure 60. Readings Taken for Rotor Tip Static Pressure Contours.

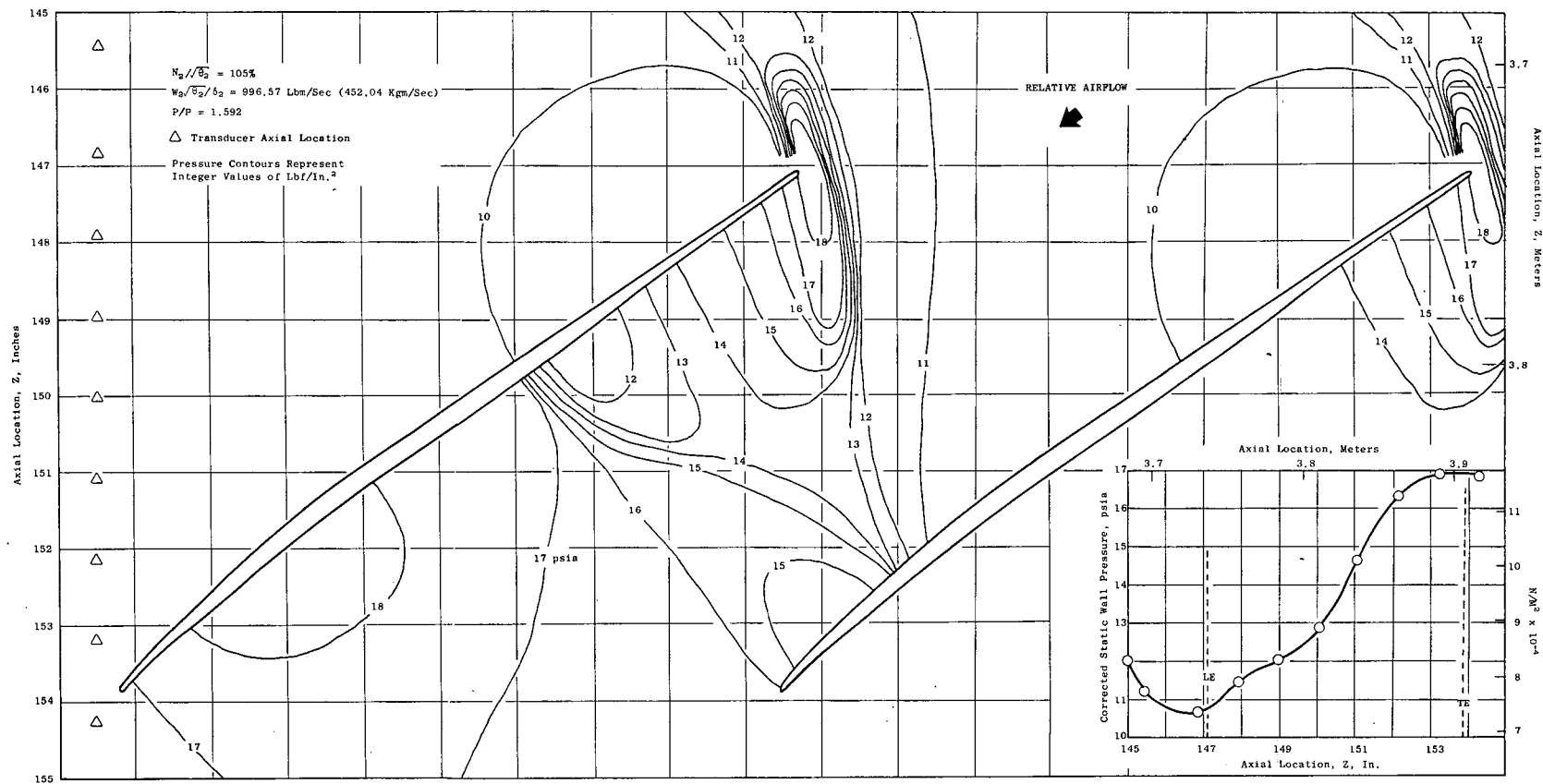


Figure 61. Rotor Static Pressure Distribution.

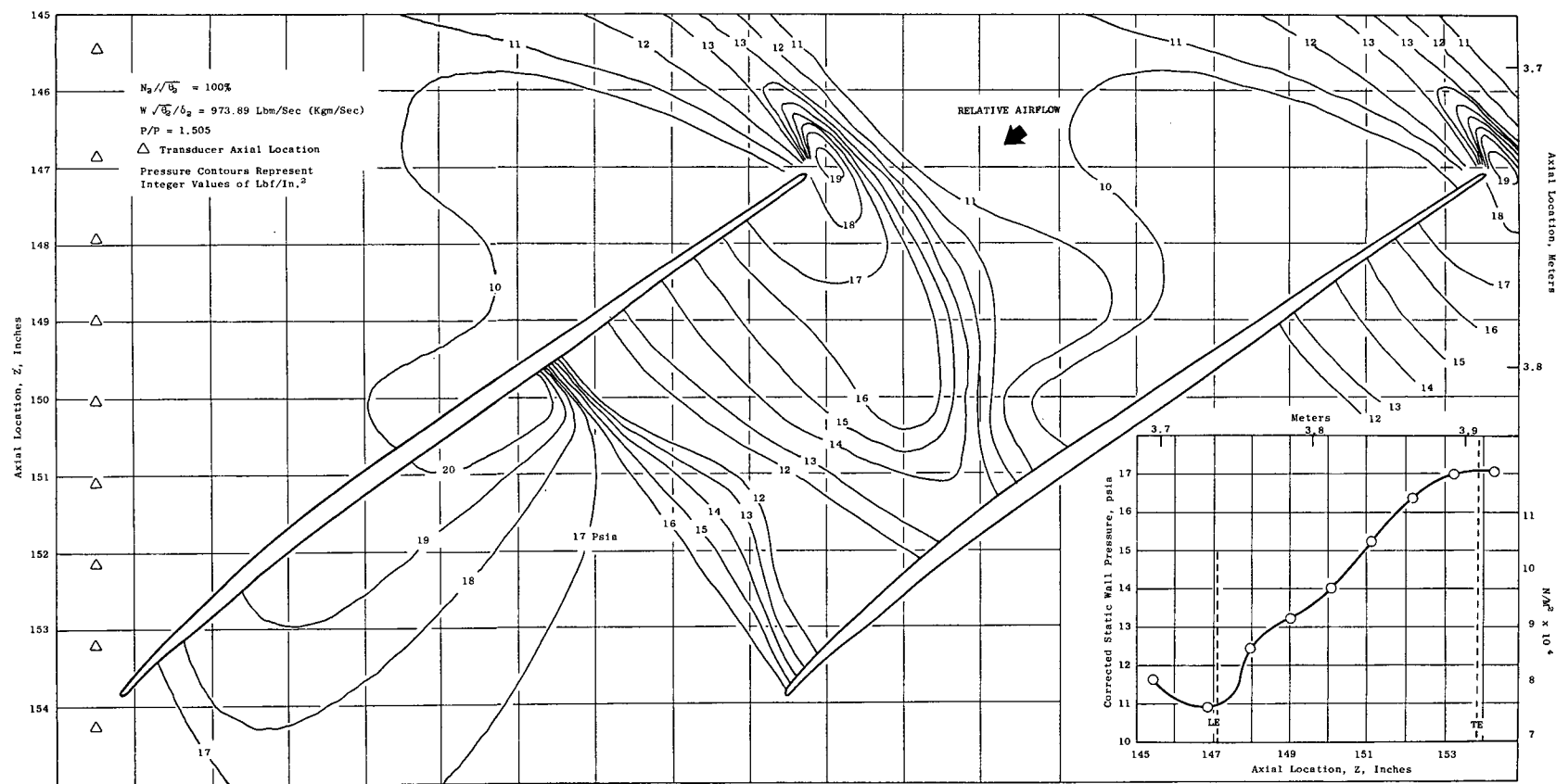


Figure 62. Rotor Static Pressure Distribution.

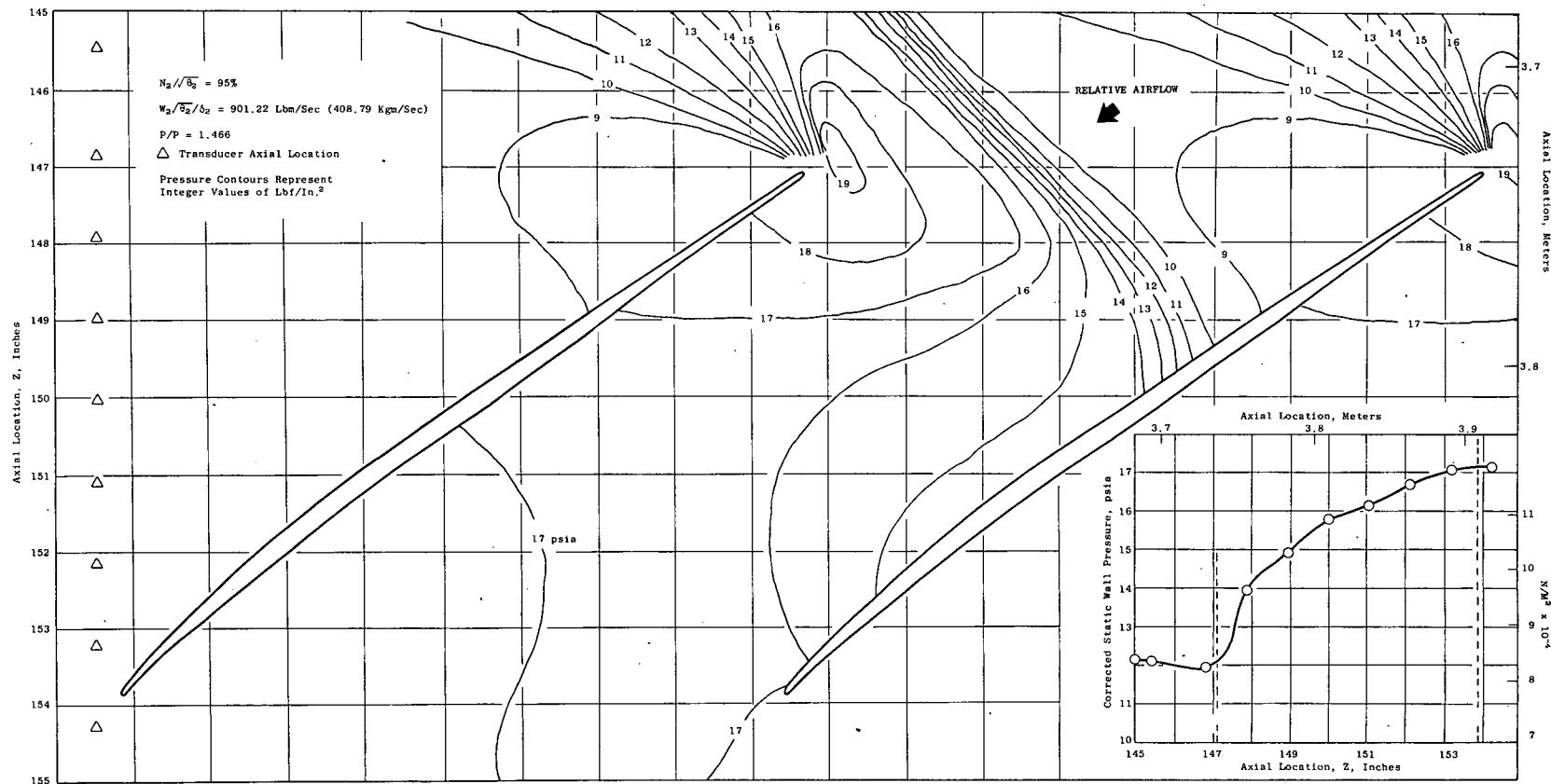


Figure 63. Rotor Static Pressure Distribution.

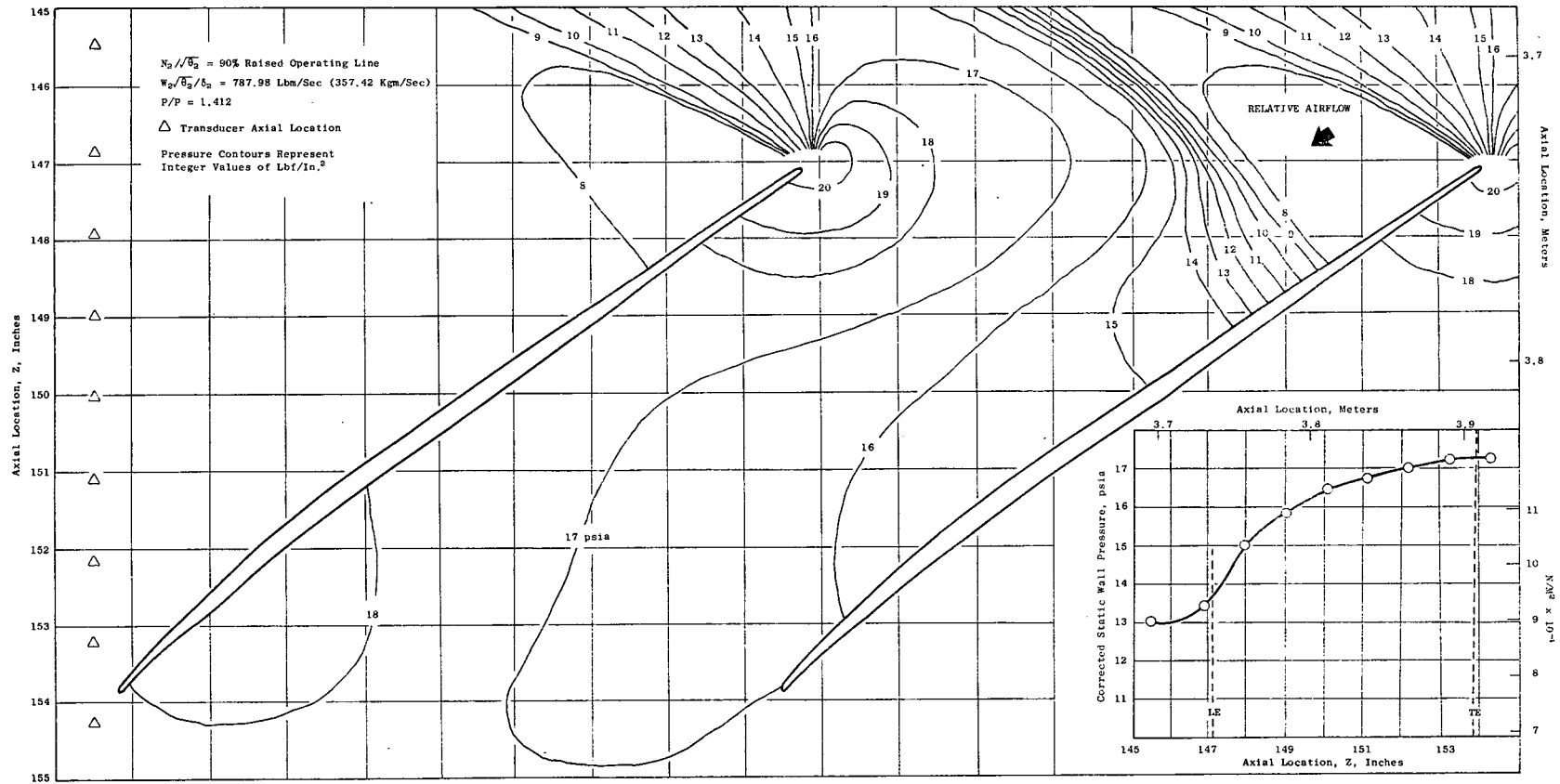


Figure 64. Rotor Static Pressure Distribution.

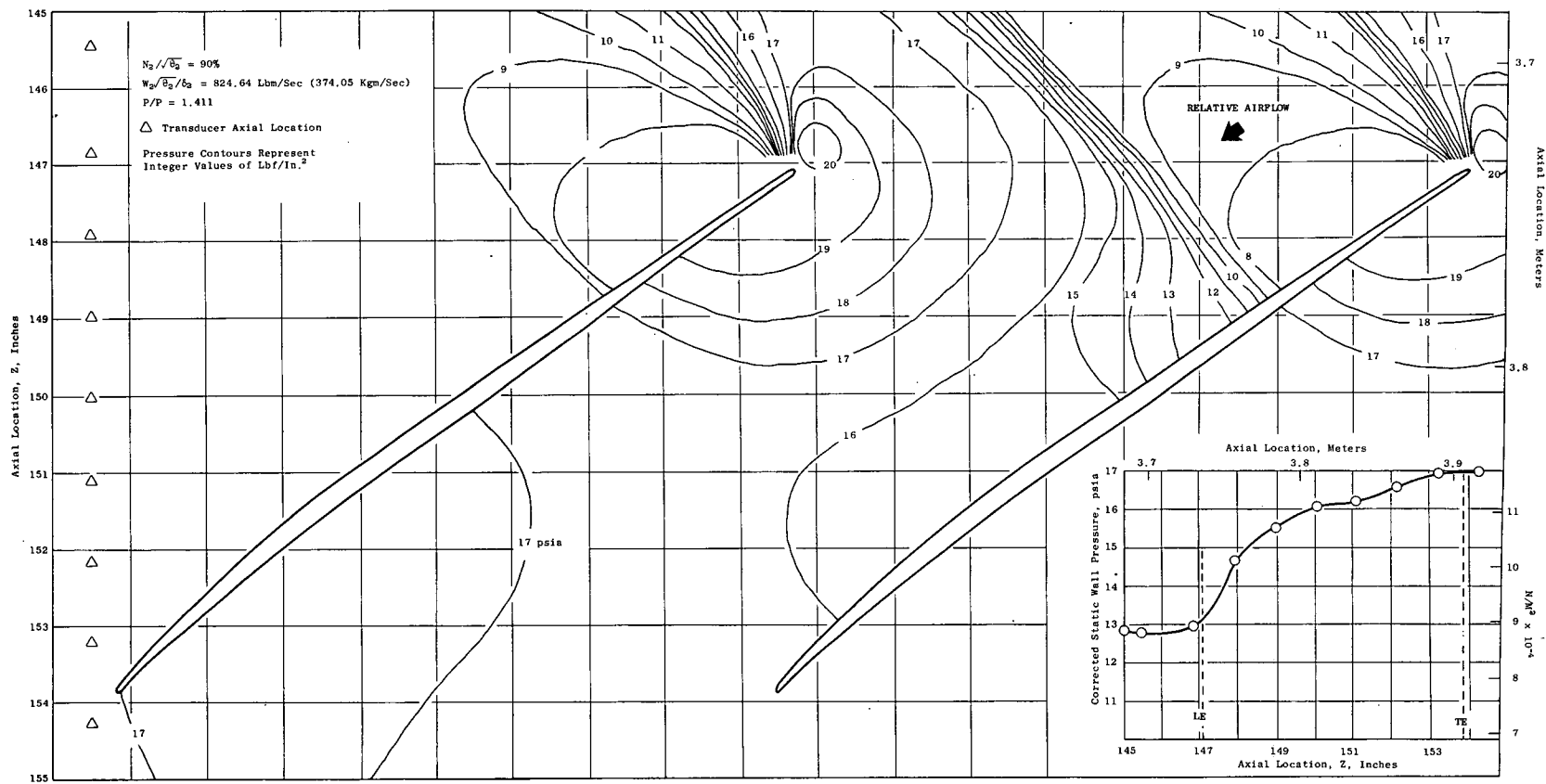


Figure 65. Rotor Static Pressure Distribution.

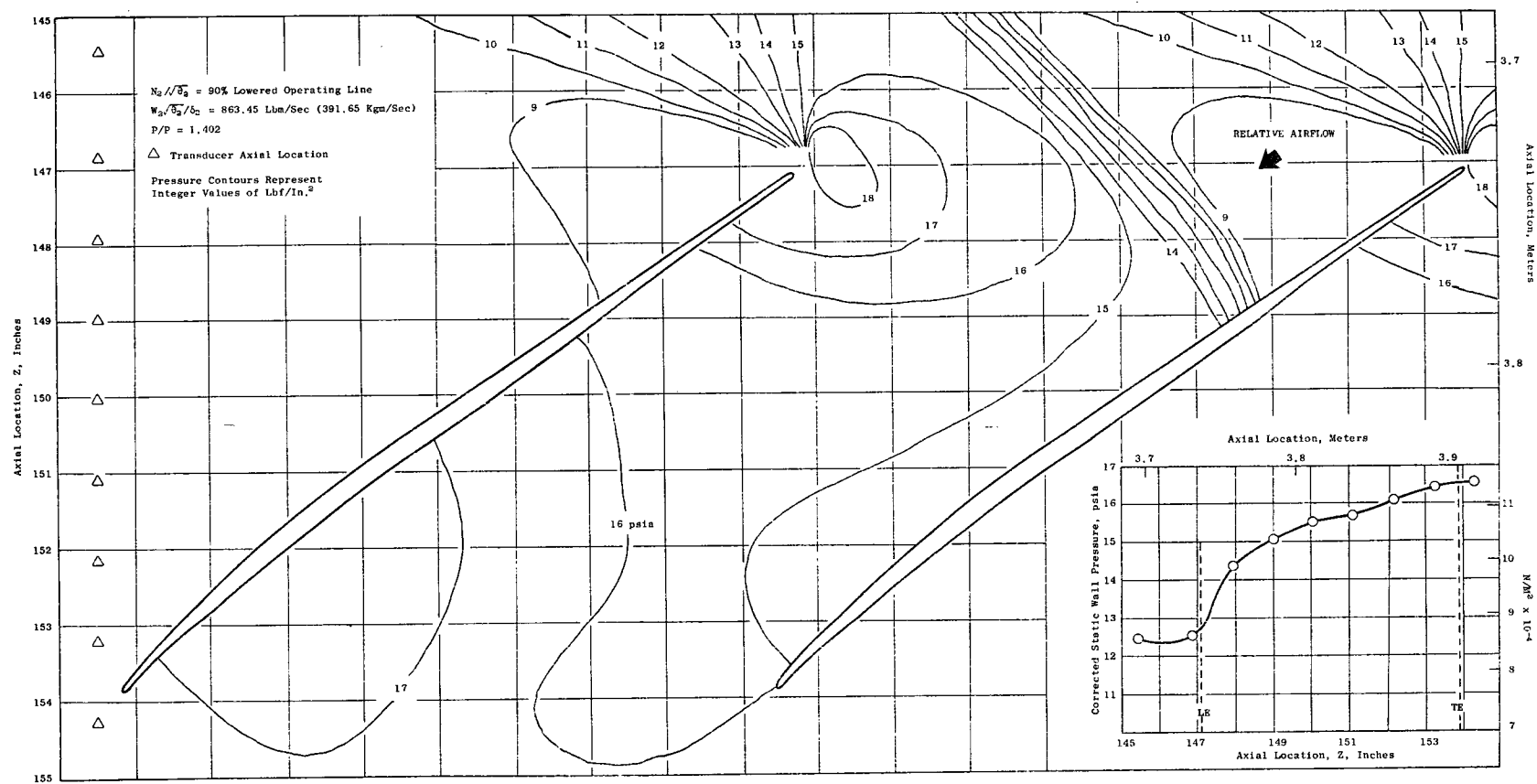


Figure 66. Rotor Static Pressure Distribution.

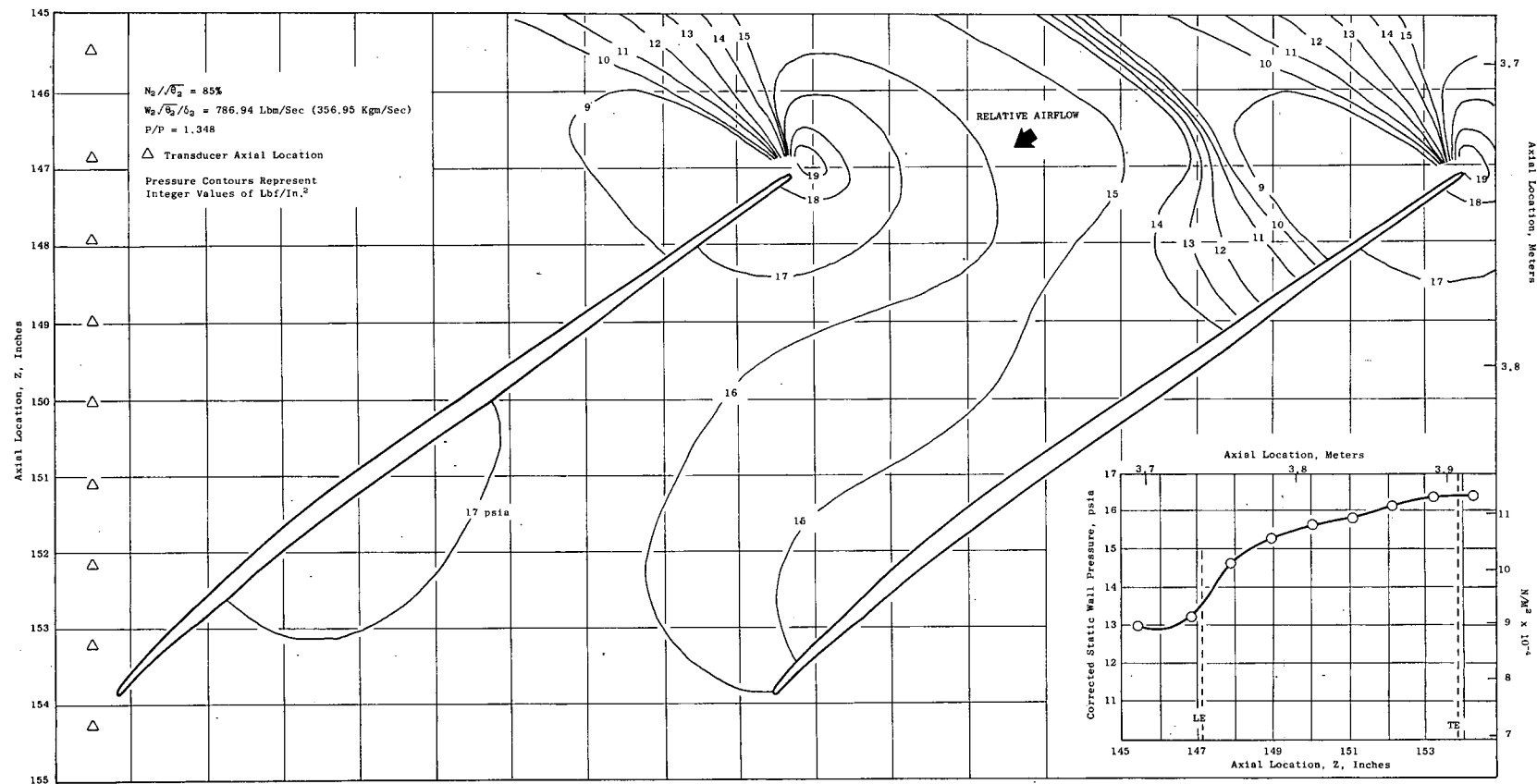


Figure 67. Rotor Static Pressure Distribution.

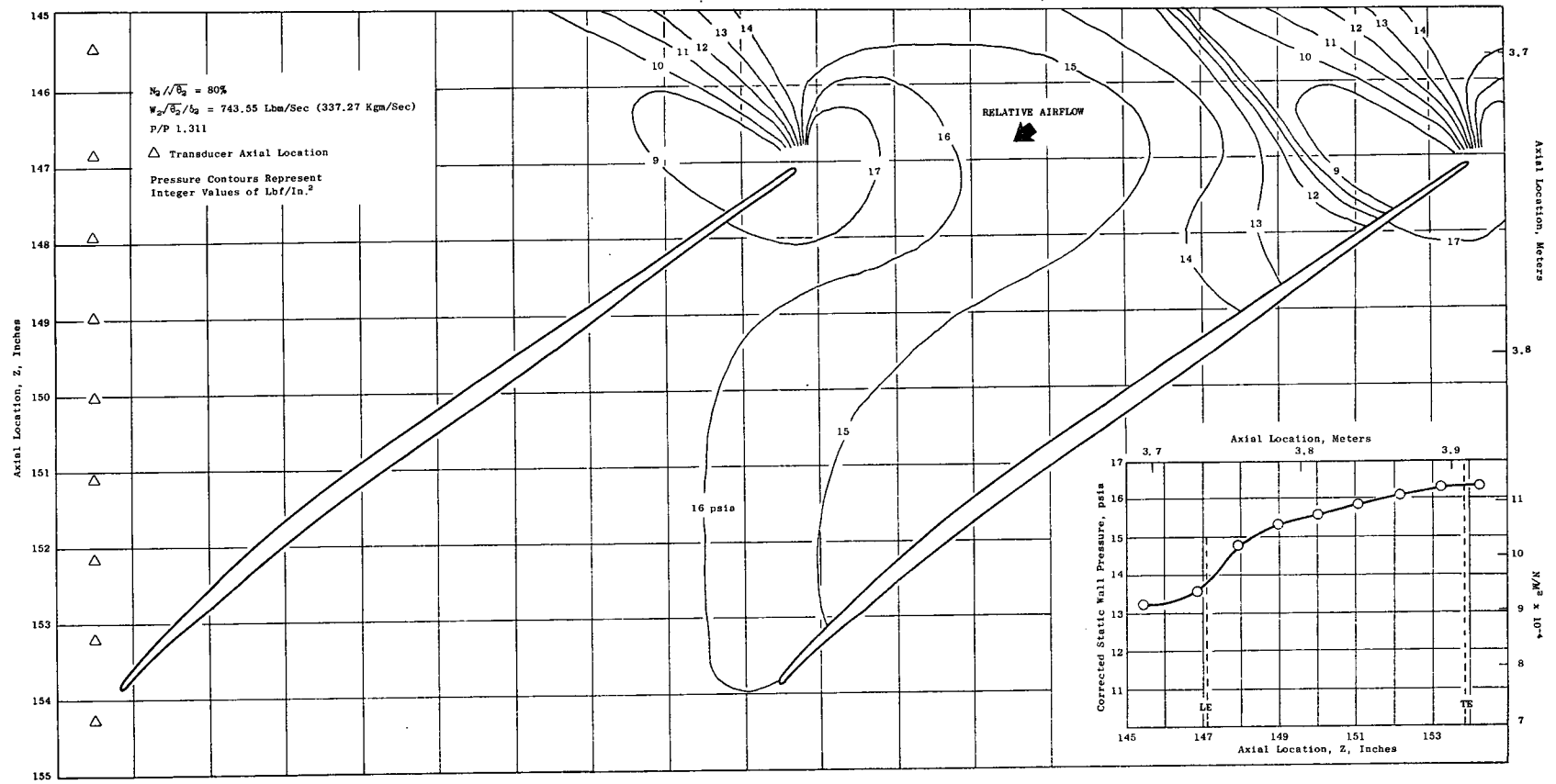


Figure 68. Rotor Static Pressure Distribution.

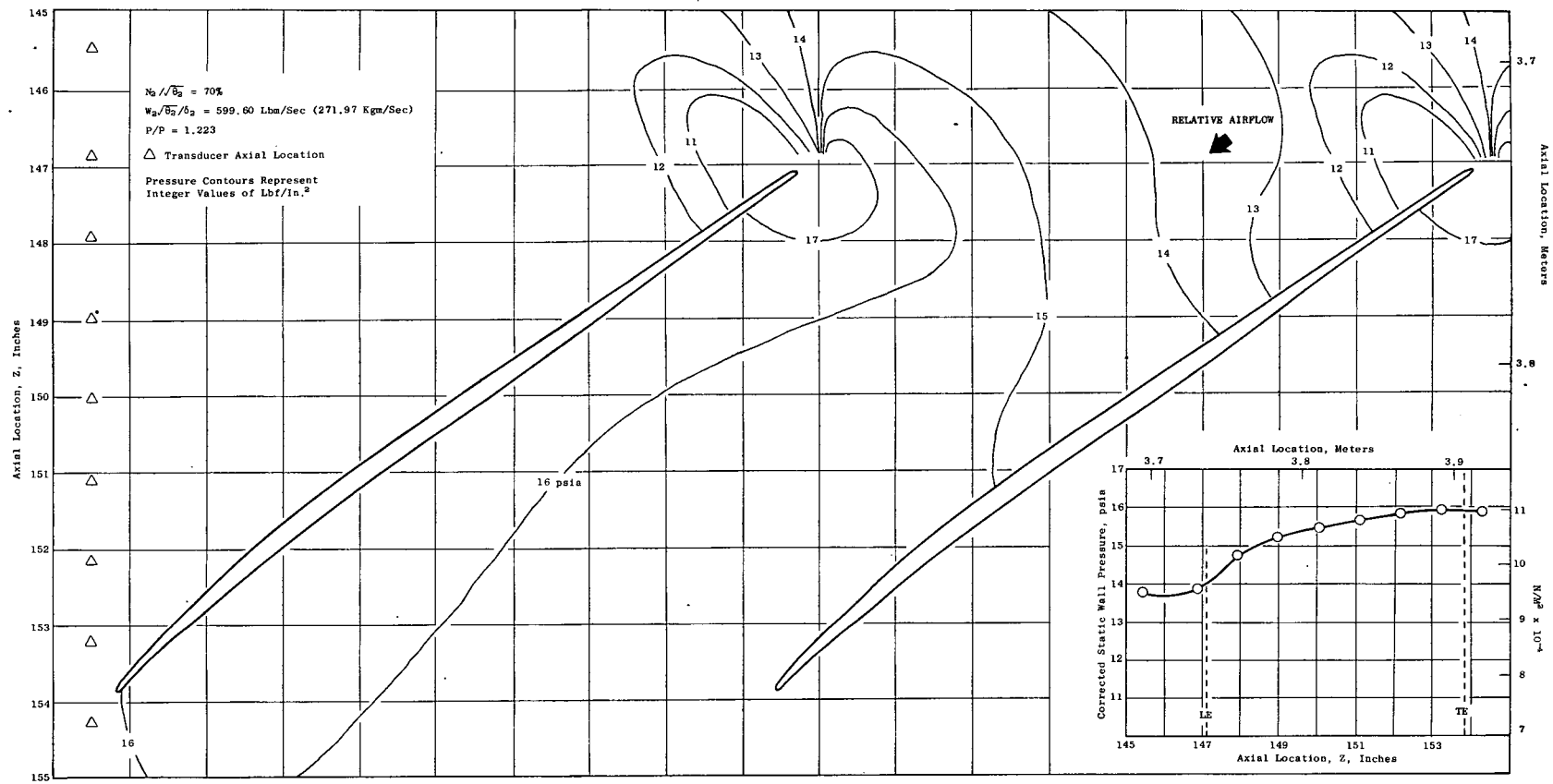


Figure 69. Rotor Static Pressure Distribution.

APPENDIX V
AEROMECHANICAL CHARACTERISTICSINTRODUCTION

This appendix covers the aeromechanical aspects of the titanium-bladed NASA Quiet Engine Fan "B" test vehicle. Some initial testing was done with an aluminum-bladed rotor, and information gained from this rotor will be included where it is unique and enlightening. The unstalled aerodynamic regions where the vehicle can be continuously operated without stalling or aeromechanical distress were determined. These regions are bounded by "operational limit lines" and defined on the fan compressor maps. Separate maps are given for a clean inlet and the different distortion patterns tested. The purpose of this section is to give the basis for setting the aeromechanical limits on the vehicle operation and to explain what can aerodynamically be expected to happen to the vehicle within these operational regions under different operations and conditions. Areas discussed are as follows:

- The general results of the laboratory stress distribution and vibratory stress surveys and how this information was used in determining the allowable stress limits for strain gage monitoring during tests.
- A discussion of the aeromechanical response characteristics of the fan blades and vanes due to various stimuli with an aerodynamically clean inlet.
- A discussion of the aeromechanical response characteristics of the fan blades and vanes during tests with distorted inlet flow. The distortion patterns tested included a tip radial, hub radial, and a one per rev distortion pattern.

RESULTS AND DISCUSSIONA. Scope Limits

To ensure the safety of the blades and vanes in a new assembly, it is necessary to install strain gages at a few locations on these airfoils to be monitored during testing. To be effectively used, one must determine before testing the maximum vibratory stress, or "scope limit", that can be allowed at these monitored locations for each possible vibratory mode. This scope limit should conservatively represent the maximum vibratory stress that can be permitted without incurring fatigue damage anywhere on the airfoil. This requires determining where a fatigue crack would be initiated for a sufficiently high vibratory amplitude, the maximum vibratory stress that can be sustained at this location without fatigue damage, and the ratio of the vibratory stress at this location to that where the monitored strain gages are located. To determine the location where a fatigue failure would first be initiated (i.e., the "critical point"), one must know the vibratory stress pattern for each vibratory mode and the steady-state

Preceding page blank

stress pattern under operating conditions. Specifically, the scope limits are determined as follows:

The steady-state stress distribution pattern is first determined using both analytical and experimental means. On the airfoil sections away from the roots of blades or the ends of the vanes, the stress pattern is determined using computer programs which have been shown to give good results in these regions. The stress near blade roots, attachment points, fillets, etc., were determined by first analytically determining the various components of moments and forces on these regions due to operating conditions. The stress influence coefficients (i.e., stress per unit load or force) due to these various components are experimentally determined in the laboratory for many points in these regions. Multiplying these stress influence coefficients by the appropriate components of the loads and adding up the results determines the local stress pattern.

Next, the vibratory stress distribution pattern is determined for the various possible modes that might be encountered. Except for the lower blade modes, this is determined experimentally by instrumenting an airfoil with many gages and vibrating it in the laboratory at its natural frequencies. For the lower modes on the rotor blades, a more sophisticated method is necessary. This is because the frequency of these modes and the associated stress pattern change markedly with engine speed. Since the vibratory stress pattern as measured in the lab does not always approximate the pattern at operating speed, a combined analytical and experimental method is necessary. This method makes use of calculated vibratory moments and the experimentally measured stress influence coefficients in a manner very similar to that used to calculate the steady-state stresses.

With both the steady-state stress pattern and the vibratory stress patterns known, it is possible to determine the critical points for the various vibratory modes. The critical point is that location where fatigue cracks would first be initiated due to the combination of steady-state and vibratory stress. In determining the critical point, a fatigue limit material properties diagram for the airfoil material is used. The Fatigue Limit Diagram which is used is one that lies three standard deviations below the mean fatigue limit curve. This ensures that only the minimum expected material properties are used for determining the scope limits.

With the critical point located, the allowable vibratory stress at this location available, and the vibratory stress pattern known, the scope limit for a particular airfoil strain gage may be calculated using the following equation.

$$\sigma_{\text{scope}} = \frac{(2) (\sigma_{\text{gage}} / \sigma_{\text{critical point}}) \sigma_e}{K_1 K_2 K_3 K_4}$$

where,

σ_e = The single-amplitude endurance limit at the critical point on the blade in this vibration mode as determined by the Fatigue Limit Diagram for the blade material and the steady-state stress at the location.

$\sigma_{\text{gage}}/\sigma_{\text{critical}}$ = The ratio of the vibratory stress at the location of the strain gage to the vibratory stress at the critical point on the blade for the vibration mode being considered.

K_1 = A blade-to-blade vibratory response variation allowance factor (usually 1.3, based on past experience).

K_2 = A factor for allowance for tolerance in the strain gage electronics circuit (usually 1.05).

K_3 = Stress concentration factor at the location of the critical point (varies with geometry and surface condition).

K_4 = An allowance for the sensitivity of the monitoring gage to slight changes in mode shape, such as might be expected due to manufacturing tolerances. (Usually determined by the ratio of vibratory stress at the nominal gage location to that about 1/10 or 1/8 inch away.

It is easier in practice to read a vibratory stress signal on an oscilloscope from the peak-to-peak of the wave rather than its amplitude. Scope limits are, therefore, normally calculated in this manner. This peak-to-peak or double amplitude method of presenting scope limits is the reason behind the two in the numerator of the scope limit equation.

Since scope limits are vibratory mode (i.e., frequency) dependent, equipment to determine the frequency as well as amplitude of the monitored strain gage signals is necessary for their proper application.

B. Clean Inlet Aeromechanical Response

1. Fan Blades

With a clean inlet, the fan blade vibratory stresses are characterized by very low levels over the majority of the operating region. Very little increase in vibratory levels were noted until very close to the operational limit line as defined on the compressor maps. This operational limit line is where either stall occurred or the blades encountered a "stress condition". The exact nature of this stress condition is not fully understood

and, since it was first felt it was a form of instability, this operational region was not probed. On the titanium rotor, this stress condition was encountered above 80 percent and below 100 percent speeds with normal rotating stall occurring at all other speeds. This differs slightly from the aluminum-bladed rotor which did not encounter the condition until 82.5 percent speed, but still encountered it at 100 percent speed. This stress condition and various other aeromechanical characteristics of the fan blades with a clean inlet are discussed in the following sections.

a. Separated Flow Response

Separated flow response is a term to describe the vibratory response of a blade or vane to cascade turbulent flow separation or free-stream turbulence. It usually involves the lower modes and is characterized by random vibratory amplitude with time.

Along the nominal operating line, blade vibration due to separated flow response was minimal and did not exceed about ten percent of scope limits as can be seen in Figure 70. The peaks in this curve are due to the integral per-rev response of the blades due to a modest amount of distortion found in even "clean" inlets. Excluding these peaks, the remaining blade stress may be attributed to the separated-flow blade response. This low blade response was characteristic even when the rotor was throttled close to the operational limit line.

b. Integral-Order Blade Response

Integral order blade response can exist when a natural frequency or mode of vibration is induced to respond at an integral multiple of the rotor speed. These multiples are referred to as "per-revs" and can be predicted from the Campbell Diagram (Figure 71) where the blade natural frequency crosses each per-rev line. It is this type of blade response that produces the peaks of stress versus rotor speed as shown on Figure 70. With a clean inlet and in the absence of inlet guide vanes, integral order blade response never caused the rotor stresses to reach high levels. Slight increases were noted when the first flexural mode blade frequency became resonant with the three per rev (around 2270 rpm), when the second flexural mode was resonant with the fifth and sixth per revs and with the first torsional mode at eight per rev.

c. Stall Response

Rotating stall was the limiting condition upon throttling up to 80 percent speed and from 100 percent speed up. At 50 percent speed, the rotor stall stresses were so low as to make stall detection difficult. These stall stresses increase rapidly with rotor rpm between 50 and 70 percent speed, but there was little further increase above 70 percent speed. The stall stresses on the titanium blades did not exceed scope limits. Stall stresses on the aluminum blades commonly exceeded scope limits during the high-speed stalls (on the order of 120 percent of limits).

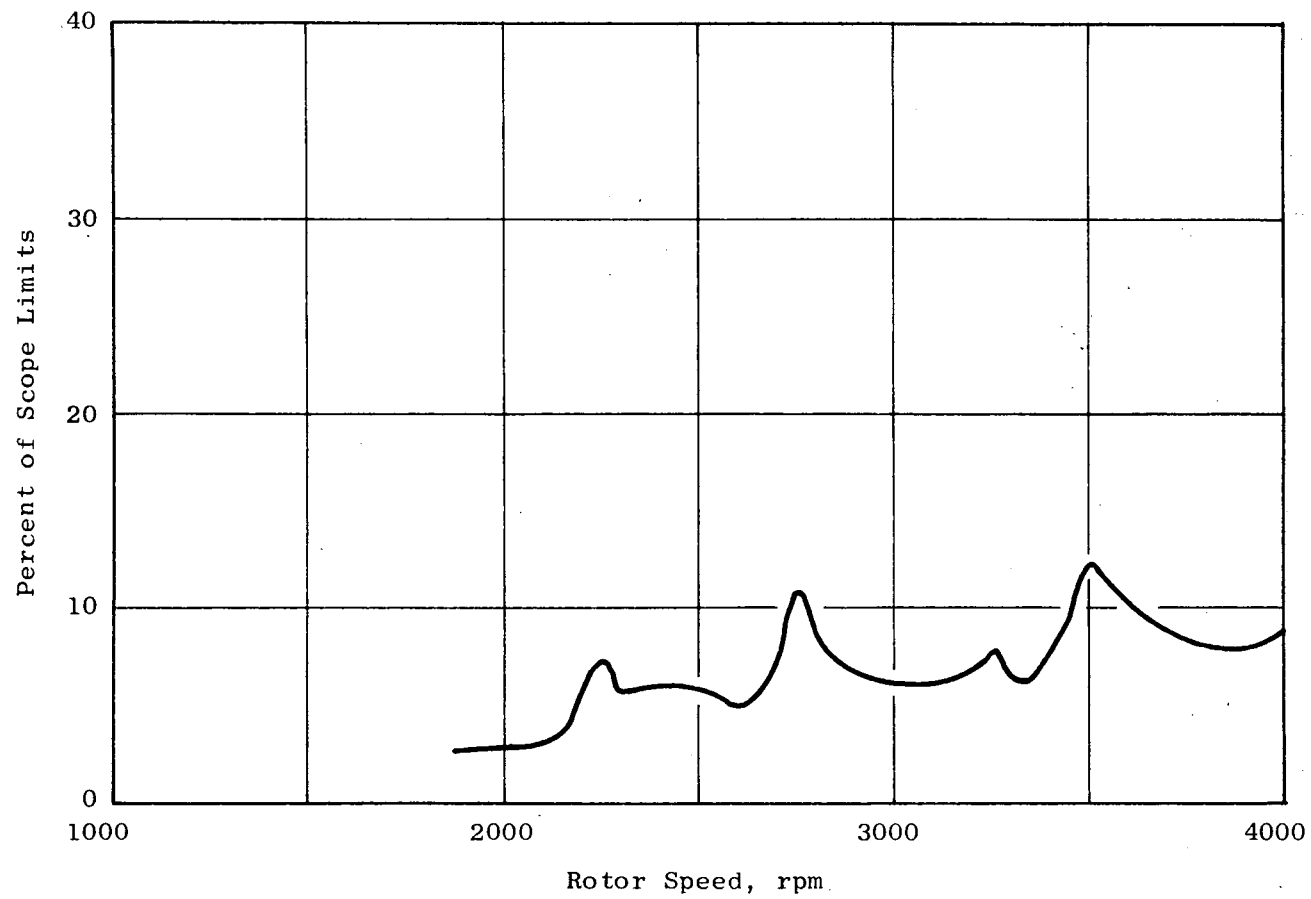


Figure 70. Titanium-Bladed Fan B Nominal Operating Line Vibrational Characteristic.

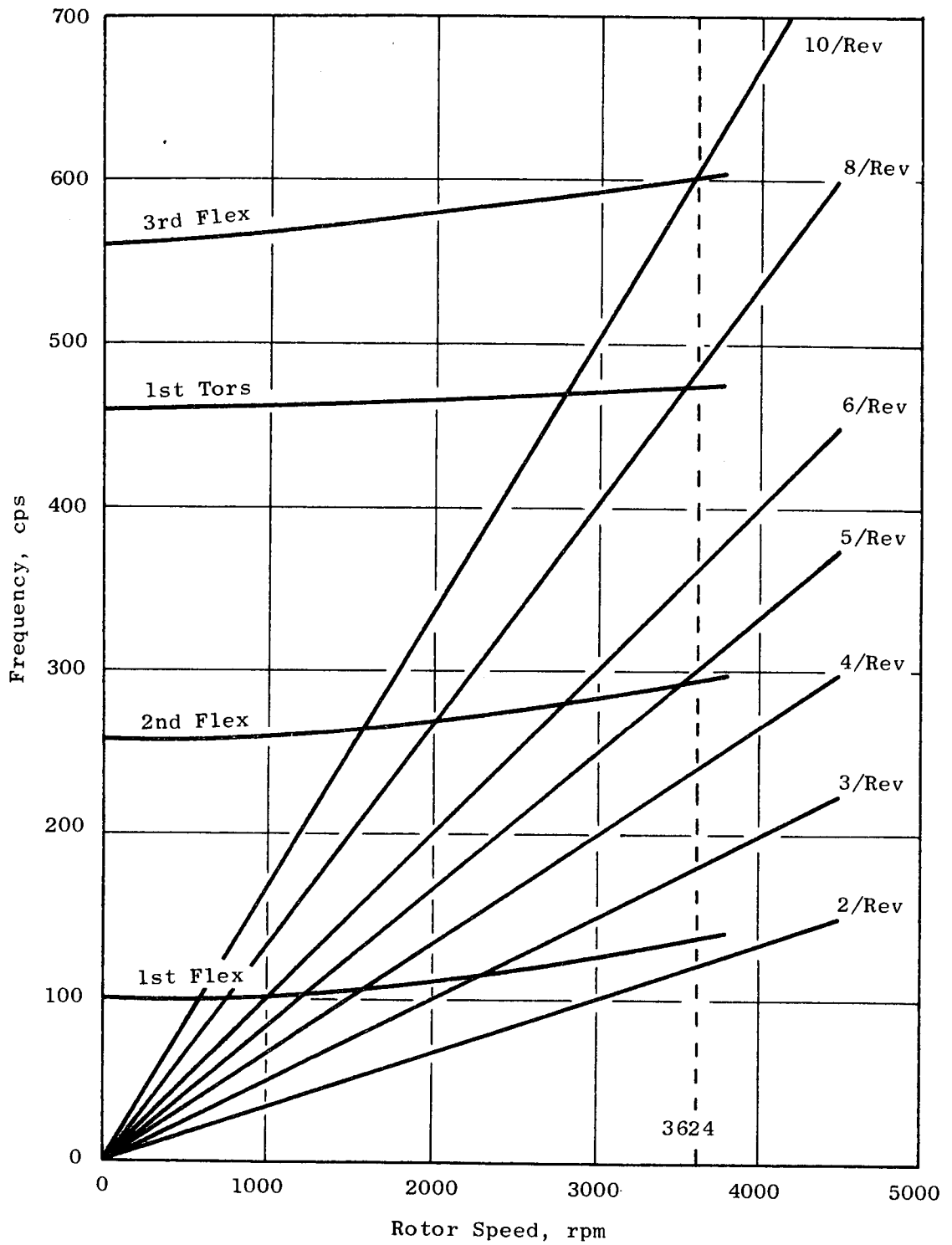


Figure 71. Titanium-Bladed Fan B Campbell Diagram.

No significant fatigue damage was incurred to the aluminum blades, however, due to the relatively few number of cycles incurred at the higher stress levels.

d. "Stress Condition" Response

Between 80 and 95 percent speeds, a vibratory stress condition was encountered near the projected stall line which could cause the blade stresses to reach 100 percent of scope limits in practically a pure first flexural mode. This condition could be a form of blade instability although there is some evidence to suggest that it is a first flexural mode blade resonance with a stall cell passing frequency. This condition was encountered while throttling the fan toward stall. Since the frequency of this mode was a nonintegral multiple of the rotational frequency and since no corresponding activity was noted on the fan OGV's, it was first felt that it was blade instability. There are troublesome aspects to this conclusion, however. For example, it occurred in an operational region where experience indicates it should not occur. Also, the phase relationship between the vibratory signals from different instrumented blades was constant and repeatable. It appeared and disappeared on all blades simultaneously and the variation in stress amplitude between the instrumented blades was very small. During the final series of tests, a Kulite dynamic pressure probe was installed behind the rotor, and the dynamic pressure pattern at several immersions was obtained behind the rotor at 85 percent speed. A varying pressure pattern was detected near the blade tips. It could be shown that this pressure pattern frequency and the blade response frequency and the measured phase relationship between the instrumented blades could both be explained by a seven cell rotating stall or other rotating seven cell aerodynamic disturbance.

This stress condition would develop rapidly with further throttling and was capable of driving the blades to 100 percent of scope limits.

2. Stator Vanes

a. Separated Flow Response

Separated flow was the primary excitation source for the Fan "B" vanes. Vane stresses from this source caused typical vibratory stress limits at 100 percent speed of 17 percent on the forward inner OGV, 10 percent on the aft inner OGV, and 11 percent on the outer OGV's. There was very little variation in the response of these vanes as the fan was throttled.

An instability was encountered on the outer OGV's while exploring the high speed portion of the fan compressor map well below the operating line. This instability was observed on only one of the instrumented vanes and was apparently caused by negative air incidence angles on the vane. With further reduction in the back pressure on the fan, the response of this vane was observed to approach 100 percent of limits.

b. Integral-Order Vane Response

Only the forward inner OGV's experienced any significant integral-order vibratory response. The first flexural mode response of this vane was excited by the 26 fan blade passing frequency around 2600 rpm. Response in this mode did not exceed 30 percent of limits (Figure 72). The outer OGV was apparently too far removed to be excited by the fan blade wakes and the aft inner OGV's did not have a blade passing resonance in the operating speed range (See Figures 73, 74, and 75).

c. Distorted Inlet Aeromechanical Response

1. Rotor Blade Response

Three distortion patterns were tested on the titanium-bladed Fan B. They were a hub radial, a tip radial, and a one per rev (180 degrees) distortion pattern. All had a $\Delta P/P$ of about 15 percent. With the distortion patterns, the vehicle was only tested to 90 percent speed. The vibratory response of the blades along the nominal operating line with the hub and tip distortion patterns remained low and did not increase very much from the clean inlet conditions. The one per rev pattern did induce a larger stress increase. This increase occurred around 2270 rpm and was an integral order resonance with the rotor speed. The blade vibratory stresses with all patterns tested remained below the scope limits. Specific blade vibratory characteristics are discussed in the following sections.

a. Separated Flow Response

Along the nominal operating line up to 90 percent speed (the maximum test speed with the distortion patterns), the separated flow response of the blades increased only slightly from that noted with the clean inlet. The largest increase in this type of blade response occurred with the hub radial pattern where the separated flow response reached 15 percent of limits. With throttling, the blade stresses did increase a little more rapidly with inlet distortion than occurred with a clean inlet.

b. Integral-Order Blade Response

The most significant aeromechanical effect of the distortion patterns on the blades was caused by the one per rev pattern. Around 2250 rpm, the blade first flexural resonance response to the three per rev increased blade stress to 70 percent of limits. This represented about a ten fold increase over the stress levels observed at other speeds, but represented no problem to fan operation in this region. This blade vibratory response was anticipated since one per rev distortion patterns commonly have appreciable components of other odd number per rev harmonics.

Neither the hub or the tip radial distortion patterns caused a significant change in the vibratory response along the operating line.

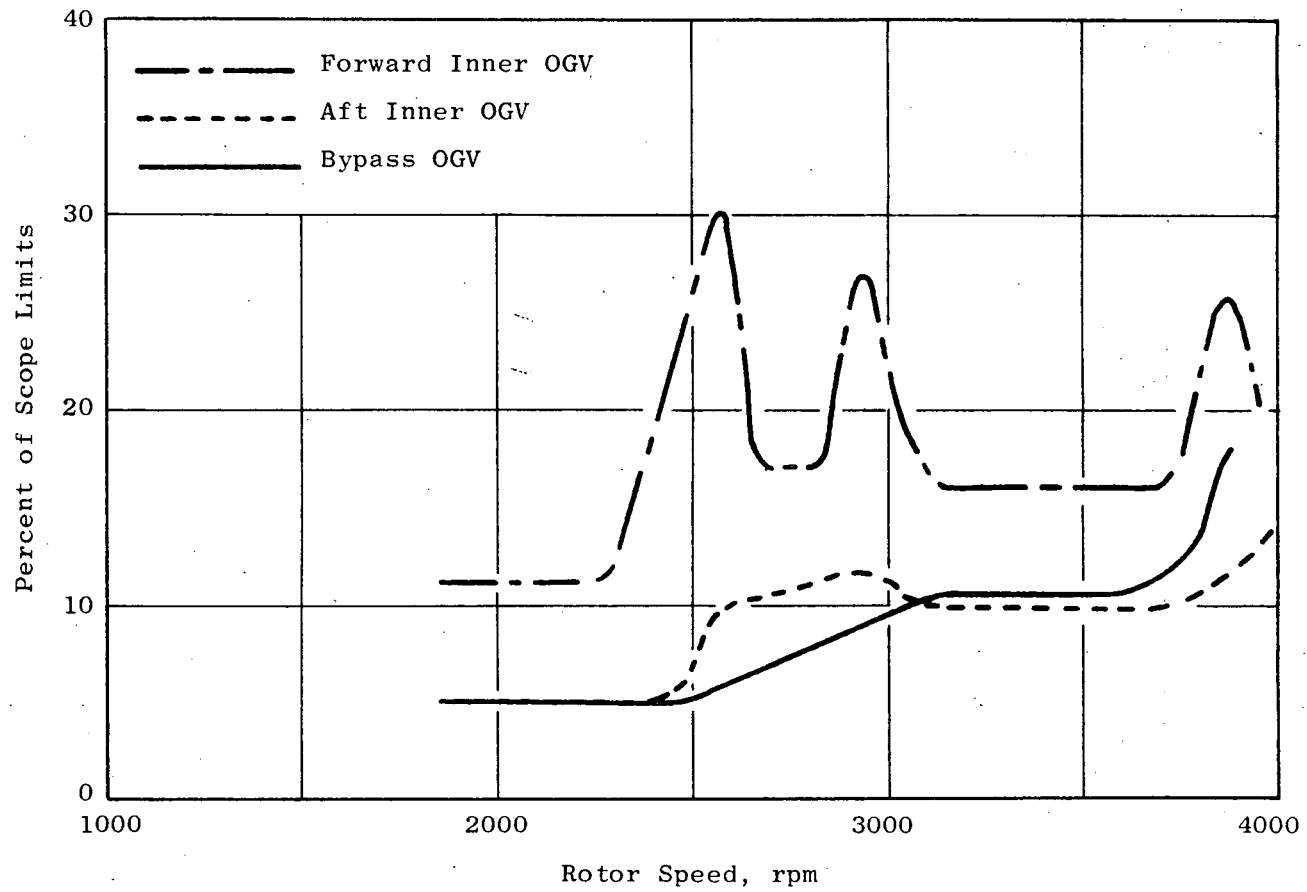


Figure 72. Fan B Stator Vanes Nominal Operating Line Vibration Characteristic.

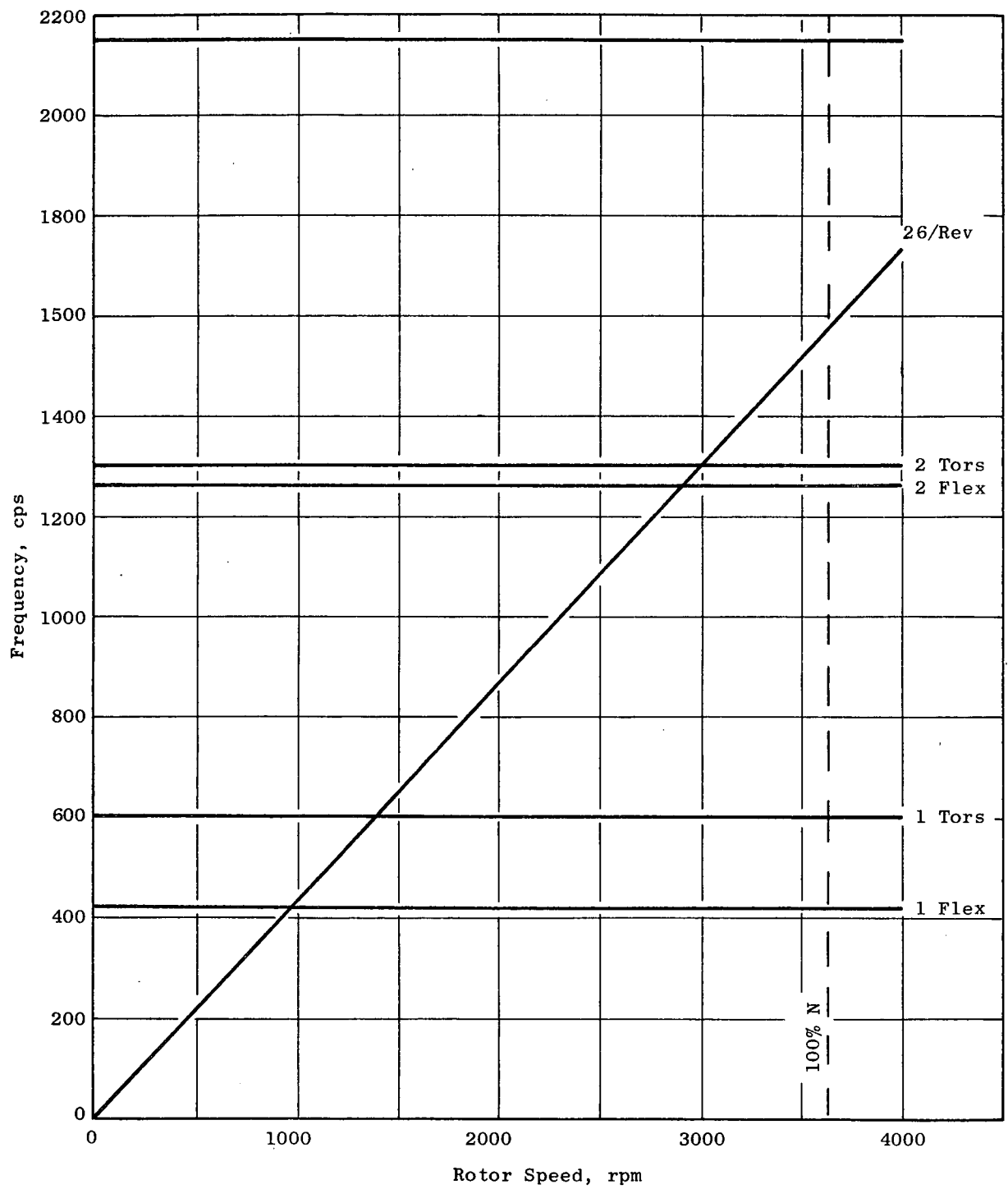


Figure 73. Fan B Bypass OGV, Campbell Diagram.

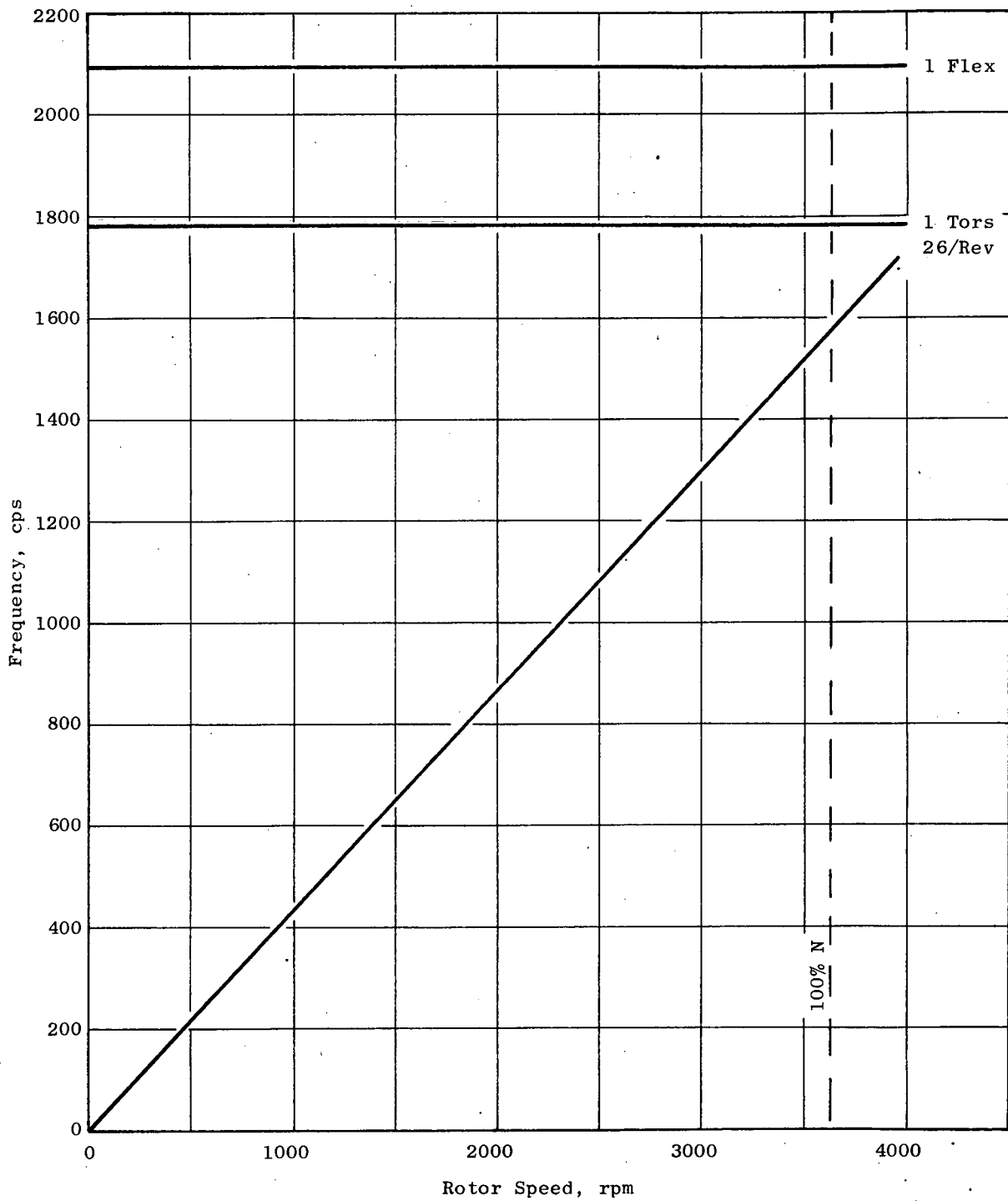


Figure 74. Fan B Aft Inner OGV, Campbell Diagram.

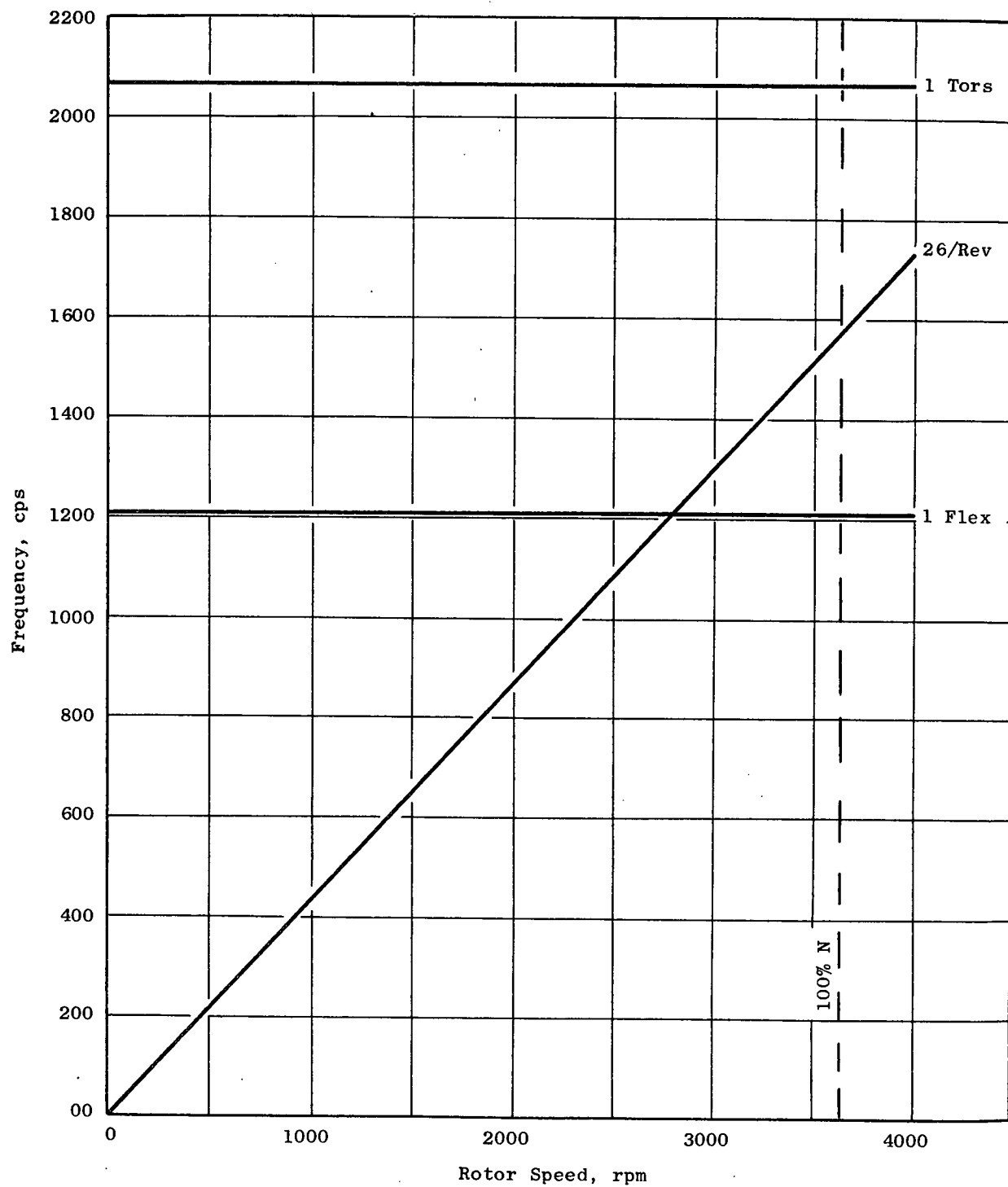


Figure 75. Fan B Forward Inner OGV, Campbell Diagram.

c. Stall and Stress Condition Response

The vehicle was throttled to stall with each of the three distortion patterns at 90 percent speed. With the hub radial pattern, the blade "stress condition" was encountered before stall. Normal rotating stall occurred with both the tip radial and the one per rev patterns. Blade stall stresses with the one per rev pattern reached 68 percent of scope limits or approximately that experienced with a clean inlet. With a tip radial pattern, stall stresses only reached 42 percent of limits. This indicates that the stall was occurring over only a portion of the blade span.

The blade stress condition discussed earlier was encountered around 80 percent speed with the tip radial distortion pattern and at 90 percent speed with the hub radial pattern. The characteristics of this phenomena duplicated exactly those encountered with a clean inlet.

2. Stator Response

vibratory response was not notably effected by any of the three distortion patterns tested. The only exception to this was a local stress variative on the fan OGV's when they were tested with the one per rev distortion pattern. Those vanes near the edge of the "shadow" of the pattern did experience a higher than normal amount of activity. None of these vanes had stress levels exceeding 20 percent of limits, however.

CONCLUSIONS

An operational limit line for the titanium-bladed Fan "B" was determined with three different inlet distortion patterns. Within these operational limit lines, the fan may be operated successfully without encountering stall or concern for fatigue damage to the airfoils. Specifically, with a clean inlet, Fan "B" demonstrated the following characteristics:

- Rotor stresses were very low and did not exceed 15 percent of scope limits along the nominal operating line.
- Stator stresses did not exceed 30 percent along the nominal operating line. While mapping the compressor well below nominal operating line, an instability did occur on the bypass OGV's which caused the vane stresses to approach 100 percent of limits.

With inlet distortion, the following aeromechanical characteristics were demonstrated:

- Rotor vibratory stresses only increase slightly with the hub and tip radial inlet distortion patterns. With the one per rev distortion pattern, blade stresses rose to 70 percent of limits at 2250 rpm. At the take-off speed, however, little increase in blade vibratory stress was noted with this pattern.

- The stator vibratory response patterns duplicated those demonstrated with a clean inlet with both the tip and hub distortion patterns. With a one per rev pattern, only individual fan OGV's near the edge of the pattern responded with a greater activity.

LIST OF SYMBOLS

A_t	throttle area, nozzle throat area required to pass measured weight flow assuming isentropic expansion from measured discharge total pressure and total temperature to ambient static pressure, ft^2
BPR	bypass ratio
B/U	build up
C_p	static-pressure-rise coefficient, $\Delta p/q^*$
DV	Discharge Valve
N	rotational speed, rpm
\bar{P}	total pressure, psia
p	static pressure, psia
Δp	static pressure rise across OGV, psia
q^*	$\bar{P} - p$, psia
R	radius, in.
\bar{T}	total temperature, $^{\circ}\text{R}$
V	velocity, ft/sec
W	weight flow, lb/sec
α	absolute air angle, degrees
β	relative air angle, degrees
δ	ratio: $-\frac{\text{total pressure}}{\text{standard pressure}}, \frac{\text{psia}}{14.696 \text{ psia}}$
η	efficiency
θ	ratio: $-\frac{\text{total temperature}}{\text{standard temperature}}, \frac{^{\circ}\text{R}}{518.688^{\circ}\text{R}}$
λ	effective-area coefficient
ψ	stream function, percent flow passing between OD and point of interest, $\psi_{OD} = 0$, $\psi_{ID} = 1$
$\bar{\omega}$	total-pressure-loss coefficient

Subscripts:

Ad	adiabatic
fs	free stream
OGV	outlet guide vane
2	fan inlet
2c	fan inlet, core portion
23	fan discharge, bypass portion
24	fan discharge, core portion